Reduced shape-space : approach to material characterization instrumented indentation test case

Liang Meng

Par **Liang MENG**

Reduced shape-space : approach to material characterization instrumented indentation test case

Thèse présentée pour l'obtention du grade de Docteur de l'UTC

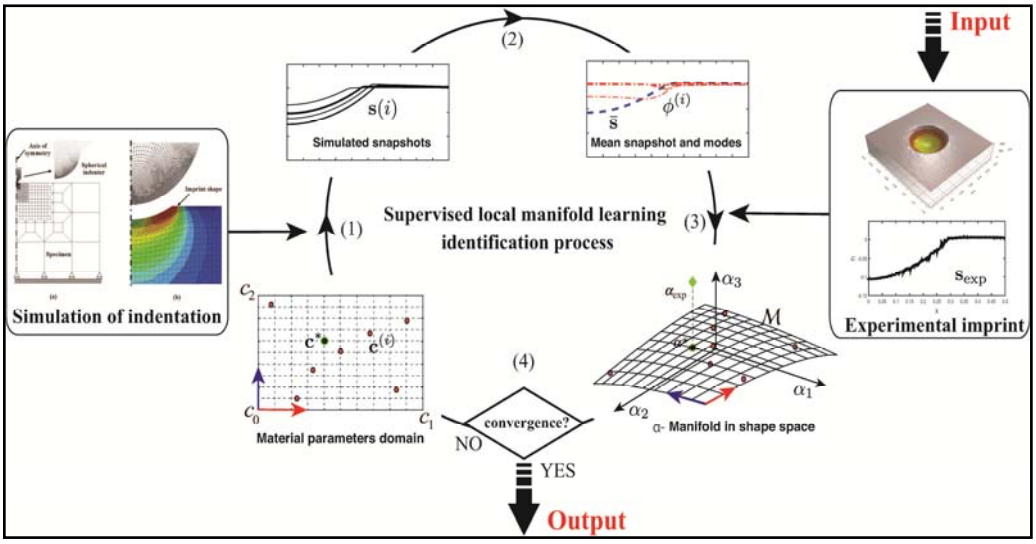

Soutenue le 19 octobre 2017
Spécialité : Mécanique Avancée : Unité de recherche en Mécanique - Laboratoire Roberval (UMR-7337)

D2377

Reduced Shape-space : Approach to Material Characterization Instrumented Indentation Test Case

Liang MENG

Laboratoire Roberval, UMR 7337 UTC-CNRS
Sorbonne Universités, Université de Technologie de Compiègne

Spécialité : Mécanique Avancée

This dissertation is submitted for the degree of *Doctor*
Defense on the 19th October, 2017

Composition of the Jury

Reviewers:
Pierre DUYSINX, Université de Liège, Belgium
Emmanuelle ABISSET-CHAVANNE, École Centrale de Nantes, France Examiners:
Florian DE VUYST, Université de Technologie de Compiègne, France
Weihong ZHANG, Northwestern Polytechnical University, China
Balaji RAGHAVAN, INSA de Rennes, France (co-supervisor)
Piotr BREITKOPF, Université de Technologie de Compiègne, France (Advisor)
Invited:
Gérard MAUVOISIN, Université de Rennes 1, France
Olivier BARTIER, Université de Rennes 1, France

À mes parents, mes beaux-parents, ma femme et notre future bébé,
ils sauront pourquoi . . .

Acknowledgements

Financé par le China Scholarship Council (CSC), j'ai réalisé cette thèse au sein du Laboratoire Roberval de l'UTC dont l'environnement est propice aux échanges et à la réflexion. Je tiens naturellement à remercier toutes les personnes qui ont contribué, de près ou de loin, à l'accomplissement de ces travaux.

Je suis, en premier lieu, très reconnaissant envers mon directeur de thèse, Piotr Breitkopf, pour la confiance qu'il m'a accordée en acceptant d'encadrer ce travail doctoral et aussi pour toutes les heures qu'il a consacrées à diriger cette recherche. J'aimerais également lui dire à quel point j'ai apprécié sa grande disponibilité et ses conseils toujours très pertinents.

Mes remerciements vont également à mon co-encadrant, Balaji Raghavan, pour ses nombreux conseils avisés et pour sa relecture finale méticuleuse de chacun des chapitres qui m'a sans aucun doute permis de préciser mes propos. J'adresse aussi mes remerciements à Gérard Mauvoisin, Olivier Bartier, Xavier Hernot de l'Université de Rennes 1, qui ont toujours su se rendre disponibles malgré la distance et dont l'aide a été d'une importance majeure dans l'élaboration de ce travail. J'aimerais remercier Guénhaël Le Quilliec à la fois pour l'organisation de la visite dans son équipe de recherche à l'Université de Tours mais aussi pour son soutien régulier.

J'aimerais remercier, par ailleurs, Professeur Weihong ZHANG, Northwestern Polytechnical University de Chine, pour les opportunités qu'il m'a offertes notamment en effectuant mon master dans son équipe, et en me mettant en lien avec le Laboratoire Robeval de l'UTC.

Je ne saurais oublier le soutien de l'ensemble de l'équipe numérique à commencer par celui de Catherine Vayssade mais aussi de Pierre Villon, Alain Rassineux, Pierre Feissel, Delphine Brancherie, Ludovic Cauvin, Briguitte Duch avec qui j'ai grandement apprécié de travailler, échanger ou simplement discuter. Je souhaiterais aussi adresser ma gratitude à mes collègues doctorants et post-doctorants, notamment Anna, Tariq, Rudy, Abir, Intissar, Augustin, Blanche, Halil, Alain, Corentin, Ivan, Tea, Pablo, Dounia. J'apprécie énormément leurs efforts pour que je me sente à l'aise, particulièrement en m'apprenant des expressions françaises autour d'une tasse de café. Un merci tout particulier à Augustin et Paul pour les matchs de tennis qu'ils m'ont gracieusement laissés gagner pour que je puisse reprendre la rédaction de ma thèse plus efficacement.

Mes remerciments vont aussi à ma famille et mes amis chinois (trop nombreux pour être citées ici), me posant cette question récurrente, « quand est-ce que tu soutiens ta thèse ? », bien qu'angoissante, m'ont encouragé à ne jamais dévier de mon objectif final.

Ces remerciements ne peuvent s'achever sans une pensée pour ma très chère épouse : Fei Dong. Je ne peux que sourire en regardant l'épanouissement de notre couple tout au long de mes travaux scientifiques. Son soutien quotidien indéfectible et son enthousiasme contagieux dans ma vie quotidienne sont pour moi les piliers fondateurs de ce que je suis et de ce que je fais.

Abstract

The thesis lies at the intersection of three disciplines : numerical methods, experimental techniques, and machine learning. The primary aim of this work is to develop a group of algorithms for characterization by inverse analysis of a material's constitutive law. In the field of material characterization, indentation test is especially attractive since it is considered non-destructive, and may be performed even on a structure in service.

The test, similar to a hardness test, consists in penetrating an indenter into the surface of the material. The force exerted on the indenter is recorded against the penetration depth over a series of time instants, leading to a force-displacement (P-h) curve, which is the most frequently used source of information for the identification of material properties. However, the inverse problem based solely on this curve tends to be ill-posed, leading to non-unique identification solution, i.e., the "mystical material pair", for whom the corresponding force-displacement curves are almost identical despite the very different material properties .

The basic idea is then to complete the identification process with innovative experimental measurements, such as laser microscope, which allows measuring the 3D residual imprint after the withdrawal of the indenter. To address the advantage of this measurement over P-h curve, we propose to construct, within a reduced affine space, a manifold of shapes admissible to the postulated constitutive law, experimental and simulation setups, based on synthetic data. The intrinsic dimensionality of the manifold limits the number of identifiable parameters allowing to validate numerically experimental procedures.

Considering both the model and measurement errors, we develop a series of local manifold learning algorithms to solve the inverse problem iteratively for experimental results obtained in cooperation with INSA de Rennes. This approach allows us to characterize diverse metallic materials of increasing complexity, based on actual experimental measurements. For example, for the Hollomon's law, the mystical pair is alleviated in using a single imprint, while for the Voce law, a multi-depth experimental protocol is proposed to differentiate mystical siblings.

Résumé

Ce travail se situe à l'intersection des trois disciplines : méthodes numériques, techniques expérimentales et du *machine learning*, a pour but de proposer une famille de techniques d'identification par analyse inverse des lois de comportement en mécanique.

Dans le domaine d'identification des matériaux, l'indentation instrumentée est particulièrement attractive, car elle permet de procéder à des essais non-destructifs sur l'échantillon ou sur une structure en service. L'essai d'indentation, similaire à un test de dureté, consiste à enfoncer la pointe de l'indenteur à une faible profondeur dans la matière tout en enregistrant le déplacement en fonction de la force appliquée. L'identification des propriétés élasto-plastiques des matériaux est basée alors sur l'exploitation de la courbe force-déplacement (courbe *P-h*). Toutefois, le problème inverse est souvent mal posé et des problèmes d'unicité mènent à la notion de paires de "matériaux mystiques" produisant, dans des conditions d'essai donnés, des courbes *P-h* identiques, malgré des propriétés différentes.

L'idée de notre travail est de compléter la procédure d'identification en faisant appel à des dispositifs expérimentaux récents, notamment à la microscopie laser, permettant de mesurer la carte 3D de l'empreinte résiduelle obtenue après le retrait de l'indenteur. Pour aborder la question de la richesse d'information de l'empreinte par rapport à la courbe *P-h* seule, nous proposons de construire, dans un espace affine réduit, *la variété des formes* d'empreinte admissibles au sens d'une loi de comportement et du modèle d'éléments finis de l'essai. La mesure de la dimension intrinsèque nous indique alors le nombre maximal de paramètres potentiellement identifiables. Cela nous permet de proposer et de valider numériquement des nouveaux procédés expérimentaux, plus représentatifs, à partir des données synthétiques, ainsi que des algorithmes d'identification associés.

La prise en compte de l'erreur de modèle et de l'erreur de mesure, nous mène ensuite à proposer un ensemble d'algorithmes de projection d'empreintes expérimentales, réalisées en collaboration avec l'INSA de Rennes sur la variété synthétique. Nous abordons alors le problème d'identification des propriétés d'écrouissage de plusieurs matériaux de complexité croissante et départageons des "jumeaux mystiques" par des essais de multi-indentation, basés sur l'exploitation de l'empreinte seule ou en complément de la courbe *P-h*.

List of publications related to this thesis

[J1]. **Meng L**, Breitkopf P, Raghavan B, et al. Identification of material properties using indentation test and shape manifold learning approach. *Computer Methods in Applied Mechanics and Engineering*, 2015 (297), pp. 239-257.

[J2]. **Meng L**, Breitkopf P, Le Quilliec G, Raghavan B, Villon P. Nonlinear shape-manifold learning approach : concepts, tools and applications. *Archives of Computational Methods in Engineering*, 2016, pp. 1-21.

[J3]. **Meng L**, Breitkopf P, Le Quilliec G. An insight into the identifiability of material properties by instrumented indentation test using manifold approach based on P-h curve and imprint shape. *International Journal of Solids and Structures*, 2017 (106), pp. 13-26.

[J4]. **Meng L**, Raghavan B, Bartier O, et al. An objective meta-modeling approach for indentation-based material characterization. *Mechanics of Materials*, 2017 (107), pp : 31-44.

[J5]. **Meng L**, Breitkopf P, Raghavan B, et al. On the unicity of the elastoplastic parameters identified by indentation on power law and Voce hardening solids. *International Journal of Materials Forming* (submitted on 2nd November, 2017).

List of conference participations related to this thesis

[C1]. **Meng L**, Studies on the inverse identification of Voce parameters with indentation test and non-linear shape-manifold learning method, 13e Colloque National en Calcul des Structures (CSMA), 14-19 May 2017 Giens, France

[C2]. **Meng L**, Vers une approche objective pour l'identification des paramètres mécaniques basé sur l'interpolation des empreintes, Colloque "Indentation 2016" du Groupe Indentation Multi-Echelle (GIME), 12-14 October 2016 Lille, France

[C3]. **Meng L**, Towards an objective approach for the identification of mechanical properties based on interpolations of imprints. The 12th World Congress on Computational Mechanic (WCCM), 24-29 July 2016 Seoul, Korea **(IACM Travel Award, three awardees for France)**

[C4]. **Meng L**, An insight into the identifiability of material properties by instrumented indentation test using manifold approach based on P-h curve and imprint shape, The 12th International Conference on Numerical Methods in Industrial Forming Processes, 4-7 July 2016 Troyes, France

[C5]. **Meng L**, Towards an objective approach for the identification of mechanical properties based on interpolations of imprints, European Congress on Computational Methods in Applied Sciences and Engineering (ECCOMAS), 5-10 June 2016 Crète Island, Greece

[C6]. **Meng L**, Nonlinear shape manifold learning approach : concepts, tools and applications (Poster), 9th annual US-France symposium of the International Center for Applied Computational Mechanics,1-3 June 2016 Compiègne, France

[C7]. **Meng L**, Identification of material parameters using indentation test and manifold learning aprroach, 12e Colloque National en Calcul des Structures (CSMA), 18-22 May 2015 Giens, France

Table des matières

Table des figures **xix**

Liste des tableaux **xxiii**

1 Introduction **1**
1.1 Background and motivations 1
1.2 Outline 6

2 Literature review **9**
2.1 Manifold learning approach 9
2.1.1 Machine learning in solid mechanics 9
2.1.2 Dimensionality reduction algorithms 11
2.2 Characterization of material properties 18
2.3 Identification using the indentation test 20
2.3.1 Reverse analysis 20
2.3.2 Inverse identification 22
2.3.3 Uniqueness of solution to inverse identification 24

3 Nonlinear manifold learning approach **27**
3.1 Basic concepts 28
3.1.1 Shape description 28
3.1.2 Concept of shape admissibility 29
3.1.3 Concept of shape space 29
3.1.4 Hypothesis of the shape manifold 30
3.1.5 Shape interpolation 31
3.1.6 Shape projection 32
3.2 Step-by-step manifold construction 33
3.3 Numerical tools and methods 34
3.3.1 Level set representation of structural shape 34

3.3.2 Shape space constructed by PCA . . . 35
3.3.3 Intrinsic dimensionality estimation . . . 36
3.3.4 Shape manifold construction . . . 38
3.4 An illustrative example : manifold approach in material characterization . . 39
3.4.1 Material laws . . . 39
3.4.2 Comparison of manifolds based on σ-ε curves . . . 41
3.4.3 Classifying material behaviors . . . 42
3.5 Closing remarks . . . 44

4 Global manifolds based on indentation 47
4.1 Finite element simulation . . . 48
4.1.1 Finite element model . . . 48
4.1.2 Different boundary conditions . . . 50
4.2 The conditioning of the inverse identification problem . . . 50
4.3 Describing indentation quantities in reduced space . . . 52
4.3.1 Constructing snapshots from indentation quantities . . . 52
4.3.2 Reducing dimensionality of indentation snapshot by SVD . . . 54
4.4 Example shape manifold of indentation responses . . . 56
4.4.1 *P-h* curve manifolds . . . 56
4.4.2 Imprint manifolds . . . 57
4.4.3 Manifolds combining *P-h* curve and imprint . . . 59
4.5 Solving the inverse identification problem in reduced space . . . 59
4.5.1 Objective function based on *P-h* curve . . . 60
4.5.2 Objective function based on imprints . . . 61
4.5.3 Objective function based on *P-h* curve and imprint . . . 62
4.6 On the identifiablity of different parameters . . . 62
4.6.1 Sensitivity analysis . . . 62
4.6.2 Conditioning number . . . 64
4.6.3 The choice of weighting coefficient *w* . . . 64
4.7 Unique identification of Hollomon's law with only a conical indenter . . . 65
4.8 Closing remarks . . . 67

5 Local manifolds based on indentation 69
5.1 Inverse identification problem based on local manifolds . . . 70
5.2 Local manifold learning algorithm families . . . 71
5.2.1 *panning* . . . 72
5.2.2 *zooming* . . . 72

5.2.3 *panning & zooming* . . . 73
5.2.4 *Floating search* . . . 74
5.3 Inverse identification of Hollomon's parameters . . . 76
5.4 Inverse identification of Voce parameters . . . 78
5.4.1 Identifying Voce parameters . . . 78
5.5 Closing remarks . . . 82

6 Non-uniqueness identification of Voce parameters 83
6.1 Unique identification from σ-ε curve . . . 84
6.1.1 Comparison of global manifolds for Voce law . . . 84
6.1.2 Local manifold identification of Voce law . . . 84
6.2 Inadequacy of "single depth" indentation . . . 86
6.2.1 Comparison of global indetation manifolds . . . 86
6.2.2 The concept of "true" and "false" mystical pairs . . . 88
6.3 Alternative identification techniques . . . 90
6.3.1 Dual-sharp indentation . . . 90
6.3.2 Multi-depth indentation protocol . . . 91
6.4 Closing remarks . . . 93

7 Identification from experimental imprint obtained from spherical indentation 95
7.1 Materials and experimental techniques . . . 96
7.1.1 Test materials . . . 96
7.1.2 Indentation set-up and procedure . . . 98
7.1.3 Analyzing the imprint shape . . . 99
7.1.4 Experimental employment . . . 100
7.2 AISI 1095 STEEL test case . . . 101
7.2.1 Problem description . . . 101
7.2.2 Results and discussion . . . 102
7.3 SECOND TEST CASE : aluminum alloys . . . 110
7.4 Characterizing the three materials with Voce parameters . . . 111
7.5 Discussions on the material constitutive behaviors . . . 112
7.6 Closing remarks . . . 114

8 Conclusions and Perspectives 115

Bibliographie 119

Annexe A Preparation of specimens 131

Annexe B Identifying AISI 1095 with floating search algorithm 133

Annexe C Verification of local-manifold identification method 137

C.1 Truncation on POD modes 137
C.2 Sensitivity to different prescribed loads 138
C.3 Inaccuracy of local manifold 138
C.4 The effect of polynomial basis 139
C.5 The effect of number of snapshots k 140

Table des figures

1.1 3D DIC data of a thick, notched tension specimen are compared to data from a LS-DYNA simulation : Maximum and minimum principal strains measured with DIC are shown in (a) and (c), respectively. Simulated maximum and minimum principal strains are respectively presented in (b) and (d) [142]. . 2

1.2 A dimensionality reduction problem from visual perception : the input consists of a sequence of 4096-dimensional vectors, representing the brightness values of 64 pixel by 64 pixel images of a face rendered with different poses and lighting directions. A three-dimensional embedding of the data's intrinsic geometric structure is learned from data mining [147]. 3

2.1 Inappropriate use of Euclidean distance (red line) in non-linear shape manifold. 15

2.2 A typical force-displacement curve (h_f and $h_{\max}$ are the residual and maximum penetration depth, $P_{\max}$ the maximum force). 19

2.3 Schematic diagram showing pile-up/sink-in effects around the indenter tip [126]. 23

2.4 A mystical material pair, $(M_1, M_2)_{\theta=74^\circ}$, observed by Chen *et al. 2007*. . . 25

3.1 Concepts of shape space. 30

3.2 Shape manifold in shape space. 31

3.3 Shape interpolation along the manifold. 32

3.4 Projecting a shape on to the manifold. 32

3.5 Local manifold construction by "walking" along the global manifold. 33

3.6 Generating the signed distance function for a shape Ω using fixed mesh grid. 35

3.7 The connectivity/vicinity of points before and after embedding. 37

3.8 Voce law with three hardening parameters : σ_y, Q and γ. 40

3.9 Illustrative stress-strain curves and the corresponding low-dimensional embeddings for (a)-(b) perfectly elastic (Hooke's law), (c)-(d) Hollomon's power law hardening, and (e)-(f) Voce law hardening 41

3.10 Reduced shape space constructed for three different constitutive laws. . . . 43
3.11 Reduced space constructed for elasto-plastic materials hardening according to either Hollomon's or Voce law. 43
3.12 Possibility of using two different laws to characterize similar materials. . . 44

4.1 Finite element model of specimen and different indenter tips. 49
4.2 Stress field in the specimen after indentation with a perfectly sharp indenter. 49
4.3 The three possible conditionings of an inverse problem : (a) input space of a two-variable physical model, and (b)-(e) diverse situations of model outputs within condensed space. 51
4.4 Snapshot definition depending on a typical imprint obtained from a spherical indenter. 52
4.5 Snapshot definition depending on *P-h* curves with different boundary conditions. 53
4.6 A series of snapshots obtained for varying material parameters. 55
4.7 The mean snapshot and different POD modes scaled by the corresponding eigenvalues. 55
4.8 Manifolds based on indentation curve snapshots $\boldsymbol{s}_{\mathrm{C}},\ p=q=201, w=0$. . . 57
4.9 Manifolds based on imprint snapshots $\mathbf{s}_{\mathrm{I}},\ l=540, w=1$. 58
4.10 Manifolds based on combined snapshot $\boldsymbol{s}=[0.5\boldsymbol{s}_{\mathrm{I}},\ 0.5\boldsymbol{s}_{\mathrm{C}}]^{\mathrm{T}}$. 59
4.11 Objective function distribution when employing *P-h* curve snapshots with spherical indenter, $p=q=201,\ w=0$. 60
4.12 Objective function distribution when employing imprint snapshots with spherical indenter, $l=540,\ w=1$. 61
4.13 Objective function distribution when employing the combined snapshots with spherical indenter, $p=q=201, l=540, w=0.5$. 62
4.14 Maps of $-\nabla(\varepsilon)$ obtained from imprint manifolds in Figure 4.12 : (a) prescribed force and (b) prescribed displacement. 63
4.15 The conditioning of the inverse problem for different values of weighting coefficient *w* in Equation. 4.5 (prescribed displacement). 65
4.16 Distinguishable residual imprints for the two mystical material pairs using conical indenters. 65
4.17 Correspondence between the Design of Experiments and residual imprint mappings in "shape space". 66

5.1 Framework of material characterization using local manifold approach. . . 70
5.2 *Panning* iterations. 72

5.3 *Zooming* iterations. 73
5.4 Combination of *panning* and *zooming*. 74
5.5 Floating search strategy. 75
5.6 Convergence of σ_y(left) and n (right). 77
5.7 Convergence of the indentation curves (case i, iterations 1,2,3,9). 77
5.8 Convergence of the imprint mappings (case iii, iterations 1,3,5,8). 78
5.9 Convergence summary for the three Voce parameters (M_4) normalized by their corresponding reference values (initial point $\boldsymbol{\mu}_A$). 79
5.10 Minimizing the discrepancy between the simulated (M_4) and target (pseudo-experimental) imprints (initial point $\boldsymbol{\mu}_A$). 79
5.11 Convergence summary for the three Voce parameters (M_5) normalized by their corresponding reference values (initial point $\boldsymbol{\mu}_B$). 80
5.12 Minimizing the discrepancy between the simulated (M_5) and target (pseudo-experimental) imprints (initial point $\boldsymbol{\mu}_B$). 80
5.13 A comparison of tensile curves for (M_4, M_5) rebuilt using Voce law with the identified parameters. 81
5.14 A comparison of indentation responses for a mystical material pair (M_4, M_5) for Voce law. 81

6.1 Illustrative stress-strain curves and the corresponding low-dimensional embeddings for (a)-(b) perfectly elastic (Hooke's law), (c)-(d) Hollomon's power law hardening, and (e)-(f) Voce law hardening 85
6.2 The "target" material parameters (black dot) and eight different parameter combinations chosen as initial points in parameter space. 86
6.3 High-dimensional indentation responses and the corresponding embeddings for different constitutive laws : (a)-(b) perfectly elastic (Hooke's law) (c)-(d) Hollomon's law, and (e)-(f) Voce law. 87
6.4 Goodness of fit (Equation 6.1) for the 1331 imprints using a spherical indenter. 89
6.5 Two mystical material pairs using the Voce hardening law : (Mt, M_6) the *true* mystical material pair, and (Mt, M_7) the *false* mystical material pair. 89
6.6 Goodness of fit for Voce imprints using dual-sharp indentation with : (a) $\theta = 70.3°$, and (b) $\theta = 63.14°$. 90
6.7 Multi-depths indentation responses for the mystical material pair $(M_4, M_5)_{R=0.5}$ (Figure 5.14). 91
6.8 Goodness of fit for indentation imprints using multi-depths indentation : the "true mystical material" M_6 is readily separated from others. 92
6.9 *"True"* mystical material that is distinguished with multi-depth indentation. 93

7.1 Microstructure of AISI 1095 steel. 96
7.2 Microstructure of EN AW-2017F alloy. 97
7.3 Microstructure of EN AW-5754F alloy. 97
7.4 Experimental set up for indentation. 98
7.5 Spherical indenter tip measured by a Scanning Electron Microscope(SEM). 98
7.6 Confocal laser imaging setup and a typical scanned imprint on an aluminum alloy EN AW-5754F. 99
7.7 Experimentally measured imprints for the three considered materials. . . . 100
7.8 Projection of an experimental imprint to α-space. 101
7.9 *Panning* iterations (Table 7.4). 103
7.10 Material parameters identification procedure by design space and local manifold 1. 104
7.11 Material parameters identification procedure by design space and local manifold 7. 104
7.12 Material parameters identification procedure by design space and local manifold 8. 105
7.13 *Zooming* steps (Table 7.5). 106
7.14 Experimental imprint and numerical snapshots (*zooming* algorithm). 107
7.15 Combination of *zooming* and *panning* (Table 7.6). 108
7.16 Convergence patterns for the parametric identification of n and σ_y. 109
7.17 Progressive reduction of the error estimation ε_1 between the imprint shape obtained with identified parameters and the experimental imprint reconstructed with POD modes. 109
7.18 Local manifold convergence for EN AW-2017F. 110
7.19 Convergence patterns for the parametric identification of n and σ_y for for the two aluminum alloys. 111
7.20 Comparison of tensile curves for steel AISI 1095. 112
7.21 Comparison of tensile curves for EN AW-5754F alloy 113
7.22 Comparison of tensile curves for EN AW-2017F alloy 113

A.1 Surface roughness profiles for the three materials. 132

B.1 Convergence of design space with different values of β (shrinking coefficient). 134
B.2 Actual convergence of the local manifold for case B. 135
B.3 Convergences of residual imprints for case B. 135
B.4 Convergence summary for the three cases. 136

Liste des tableaux

2.1 A comparison of diverse dimensionality reduction algorithms 18

5.1 A comparison of identified material parameters using different measured quantities. 76
5.2 Identified Voce parameters using different initial points, $E = 70$GPa, $\nu = 0.33$ and $h_{\max} = 0.1$mm. 79

6.1 Voce parameters identified from various starting points using the stress-strain curve. 86
6.2 Comparison of pile-up heights for M_4 and M_5 with diverse penetration depths. 91

7.1 Composition of the AISI 1095 steel used in this study given in % of weight content. 96
7.2 Composition of the EN AW-2017F aluminum alloy used in this study given in % of weight content. 97
7.3 Composition of the EN AW-5754F aluminum alloy used in this study given in % of weight content. 97
7.4 Iteration results using *panning* approach. 103
7.5 Iteration results using regular *zooming* approach. 106
7.6 Iteration results using *panning* & *zooming*. 108
7.7 Summary of identified Hollomon's hardening parameters for the two aluminum alloys. 110
7.8 Summary of identified parameters for the three materials considering different hardening behaviors. 111

A.1 Surface roughness measures for the studied samples. 131

B.1 Summary of identified hardening coefficient for steel. 134

C.1 Identified results with truncated POD modes. 137

C.2 Identified results with prescribed force of 300 N. 138
C.3 Identified results derived by adopting different polynomial basis. 139
C.4 Identified results using different number of snapshots. 140

List of abbreviations

General

e.g.	exampli gratia or "for example"
w.r.t	with respect to
AFM	Atomic force microscope
AI	Artificial intelligence
ANN	Artificial neural networks
CLSM	Confocal laser scanning microscope
DA	Dimensional analysis
DIC	Digital image correlation
DoE	Design of experiments
FE	Finite element
IIT	Instrumented indentation test
k-PCA	kernel-Principal component analysis
LLE	Locally linear embedding
MDS	Metric multidimensional scaling
NLDR	Nonlinear dimensionality reduction
PCA	Principal component analysis
PGD	Proper generalized decomposition
POD	Proper orthogonal decomposition
PGM	Plastically graded material
RB	Radial basis
ROM	Reduced order modeling
SVD	Singular value decomposition
SVM	Support vector machine

Mathematical symbols

Please note that, throughout this thesis, bold lower-case letters indicate vectors, whereas bold capital letters indicate matrix. In case of scalar/vector/matrix with index or exponent, the font and case indicate the object type after index/exponent application (e.g., $\mathbf{v}_i$ calls the i^{th} vector $\mathbf{v}$ while y_i refers to the i^{th} component of vector $\mathbf{y}$).

$\boldsymbol{C}$	covariance matrix
M	number of samples
m	reduced dimensionality
N	dimensionality of raw data
n	hardening exponent of Hollomon's law
k	number of neighbors
d_{int}	intrinsic dimensionality
R	radius of spherical indenter
t	time increment
P	indentation load
h	indenter penetration depth

Greek Letters

$\boldsymbol{\alpha}$	coordinates of raw data described in lower-dimensional space
β	coefficient of shrink in "floating-search" algorithm
θ	half-apex angle of conical indenter
$\boldsymbol{\chi}$	high-dimensional data
$\boldsymbol{\phi}$	orthogonal basis of reduced space

Subscripts

I	imprint snapshot
C	indentation curve snapshot
int	intrinsic dimensionality
exp	experimental meausrement

Chapitre 1

Introduction

The research presented in this thesis grew out of a rapidly increasing need for data analysis methods to obtain a deeper understanding of the complex physical phenomena in the field of mechanical engineering. It endeavors to promote the integration of the two disciplines of manifold learning/non-linear dimensionality reduction (NLDR) and computational mechanics. This introduction will now provide the motivations behind this work in Section 1.1, and a basic outline of the thesis in Section 1.2.

1.1 Background and motivations

Since several decades, the maturity of computational science and engineering has allowed us to simulate complex phenomena with attention to details [9, 121], albeit at the expense of an ever-increasing computing cost. Quite obviously, the outputs from finite element (FE) simulations always contain massive information, for instance the displacement [40, 117], temperature and flow fields [130, 92] measured from a solid structure. On the other hand, despite many techniques being practiced for centuries, new measurement systems and methodologies are constantly emerging, which have not merely led to a huge leap in the understanding of experimental mechanics, but to the explosion of the size of the collected data as well. For example, the advent of Digital Image Correlation (DIC) allows an experimentalist to examine, in detail, complex behavior that exists even in relatively simple mechanical tests [142], and it has revolutionized the field of material science by providing significantly more detailed information than previously available with strain gauge measurements. However, on the other hand, this technique involves a considerable amount of data to deal with, Figure 1.1. As a result, the demand for efficient data analysis methods is growing at an unprecedented fast rate.

The complexity of the collected data inevitably brings out a plethora of difficulties. For example, in structural optimization problems, overwhelmingly complex geometrical features will slow the algorithm down and make the process of finding global optima difficult. Considering the inter-dependence of geometrical parameters that must be optimized for a given objective function, a lighter yet efficient method is needed for processing the input end (design variable) of optimization algorithms [118]. In addition to simplifying the input side, reducing the output side, which typically contains massive data, is also required to gain deep insights of the problem at hand. This in turn can be helpful to design the experiments that need to be carried out. The characterization of material mechanical properties solved by inverse analysis [95], among others, falls under this second heading, and will be chosen as the current focus of this thesis.

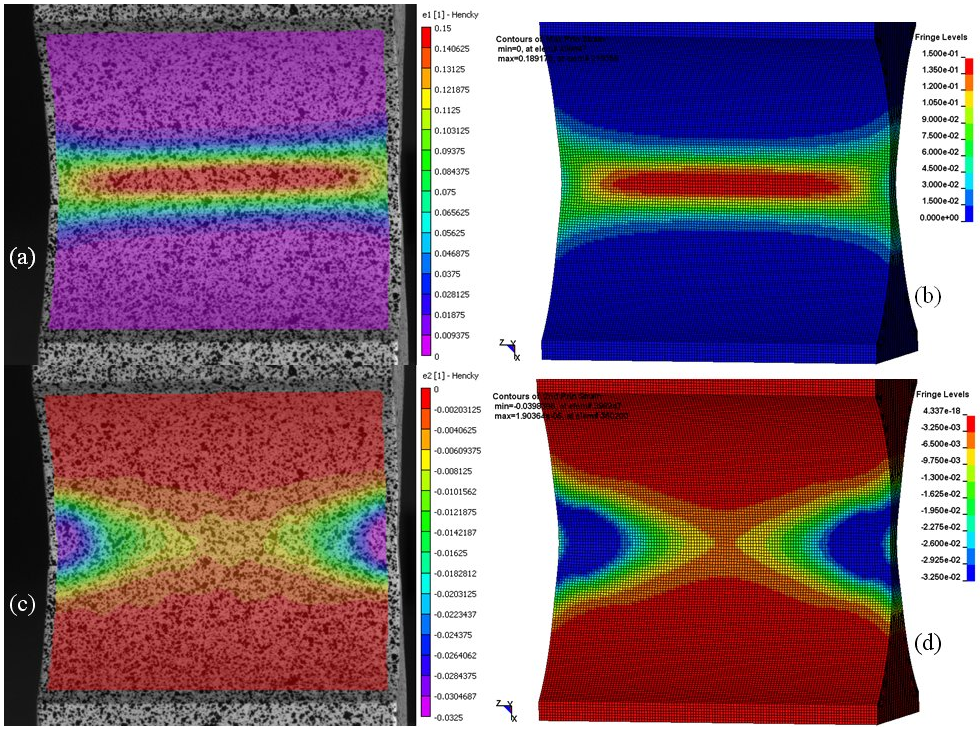

FIGURE 1.1 3D DIC data of a thick, notched tension specimen are compared to data from a LS-DYNA simulation : Maximum and minimum principal strains measured with DIC are shown in (a) and (c), respectively. Simulated maximum and minimum principal strains are respectively presented in (b) and (d) [142].

On the other hand, clearly benefiting from the heightened availability of digitized information via the internet, machine learning (ML) began to thrive in the 1990s. Over time, the field moved its goalpost from achieving artificial intelligence to tackling solvable problems of a more practical nature [80]. Another subject that overlaps significantly with machine learning is data mining. Although employing the same methods, the former focuses on

prediction based on *known* properties learned from the training data, while the latter invests itself in the discovery of *previously unknown* properties in the data. Figure 1.2 illustrates the discovery of an intrinsic three-dimensional embedding from pixel image data. Up until now, the great success of machine learning/data mining has been demonstrated various fields, e.g., pattern recognition and image processing, and its inevitable mergeing with the field of computational mechanics, propelled by the explosive complexity of models and data, is becoming increasingly visible.

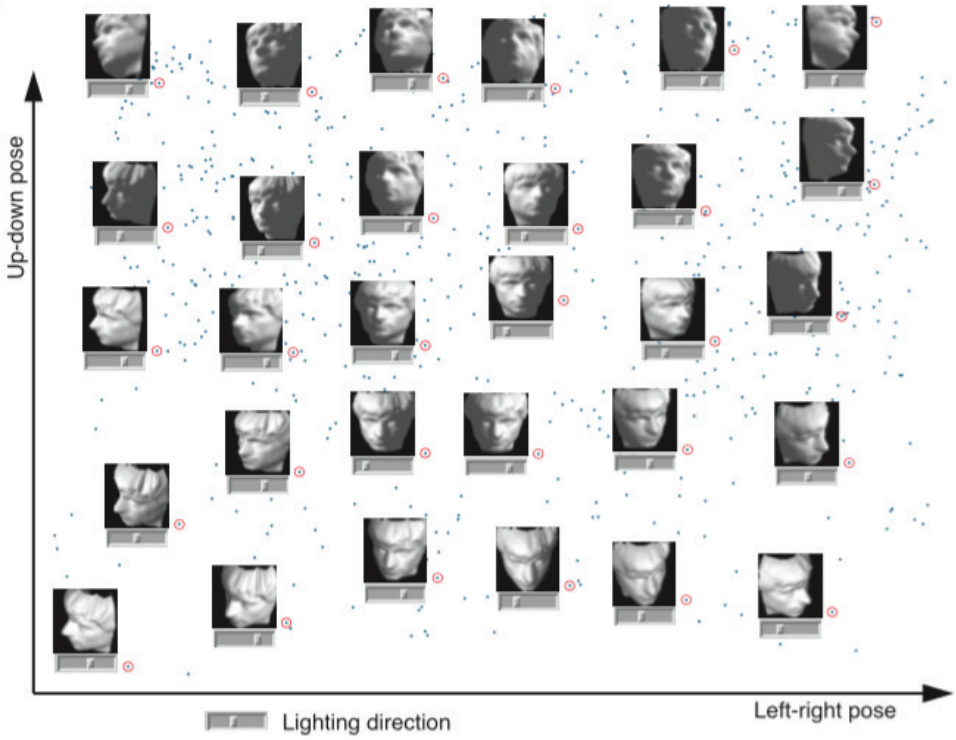

FIGURE 1.2 A dimensionality reduction problem from visual perception : the input consists of a sequence of 4096-dimensional vectors, representing the brightness values of 64 pixel by 64 pixel images of a face rendered with different poses and lighting directions. A three-dimensional embedding of the data's intrinsic geometric structure is learned from data mining [147].

With all these in mind, one stumbles somewhat naturally upon the idea of bridging the gap between these two fields. In this thesis, we make the first attempt to adapt manifold learning methods to the problem of mechanical characterization. We will carefully study one particular application in the field of material property identification using the instrumented indentation test (IIT). The idea of data mining is applied to diverse indentation response datasets with the aim of carefully and meticulously investigating the *non-unique* solutions to the inverse identification problem. Meanwhile, richer and more complex information is

proposed for use to perform more reliable characterization. The thesis is therefore conducted with the three main motivations listed below :

Motivation 1 : Apply manifold learning approaches to computational mechanics

The primary motivation of the thesis is to integrate the methods of computer science (mainly manifold learning) in the realm of computational mechanics, especially when dealing with large amounts of physical data, either simulated or experimentally measured. Given that manifold learning approaches have rarely been used in solving mechanical problems, their fundamental concepts, for instance, shape admissibility, intrinsic dimensionality and the shape-manifold hypothesis, need to be targeted and adapted to general mechanical problems in a first attempt.

Taking as an example the material characterization problem, we note that in recent years it has been a popular way to characterize unknown materials by solving an inverse problem using experimental measurements and the corresponding FE model [57, 33, 12]. In the context of indentation, the experimental measurements refer mainly to the point-wise force-displacement (*P-h*) curve and/or the increasingly popular high-accuracy field measurement, i.e., the residual imprint. This latter, obtained by scanning the specimen after the test, produces especially big amounts of data in 3D. However, the characterization problem remains a rather challenging task due to the absence of an explicit relationship between material's properties and its (*massive*) indentation responses. It clearly shows that there is a great demand to *"intelligently"* study the material plasticity encoded in the indentation responses.

Therefore, reducing the dimensionality of complex physical data and interpreting it within a much more condensed space are understandably of substantial research interest. It bears mentioning that this motivation is inspired by the common sense observation that real-life data points are observed to *fill up* the space in which they are represented in a *non-uniform* fashion, and they appear to agglomerate around a lower-dimensional hyper surface [132].

Motivation 2 : Investigate the identifiability of material parameters for different constitutive laws

Early works dealing with the subject of material characterization may be found in [11, 89, 59, 106]. Up till today, researchers have been capable of probing several material elastoplastic parameters by carrying out a single indentation test alone. The unicity of the solution obtained is generally "accepted" if the same parameter values are found by iterations from different

initial points. However, this is immature and the unique identification of parameters may be influenced by various factors, e.g., the measured quantities and the indenter's geometry. For these reasons, we propose to investigate the identifiability of diverse material parameters by analyzing the collected information, with the aid of manifold hypothesis and the estimate of intrinsic dimensionality.

Generally, the intrinsic dimensionality of raw data describes the number of variables that is needed to represent the original data. In the context of indentation-based identification, the intrinsic dimensionality of indentation responses may serve as a primary estimate of the number of identifiable parameters for a given experimental setup. This consideration could help to pave the way towards the design of experiment to be carried out in identification problems.

By this thesis, to address the above issue, two fundamental constitutive laws will be studied with special attention : the two-parameter Hollomon's power law and the three-parameter Voce law. They are chosen for two simple reasons : (a) applicable to the majority of metals and alloys, and (b) have the advantage of easier visualization of the manifold after dimensionality reduction.

Motivation 3 : Propose new protocols for unique identification

A review of existing literature indicates that the big majority of research work focuses on exploiting the recorded force-displacement curve during indentation test. However, the *P-h* curve can sometimes be *inexploitable* in cases like spherical indentation [104, 103], since the precise measurement of the displacement of the indenter tip requires the determination of the frame compliance and the non-linear tip deformation.

In addition, multiple authors [34, 148] have reported since the last few decades a phenomenon of identical *P-h* curves being obtained for different materials, termed as "mystical materials" [32]. This phenomenon unfortunately renders the solution to the inverse identification problem non-unique. It is now widely recognized that the non-unicity issue is particularly severe when self-similar indenters (mainly conical ones) are employed for the identification of the well-known Hollomon's equation for power law hardening.

A more complete and robust methodology would ostensibly involve combining the *P-h* indentation curve with mapping the residual deformation or indentation imprint in an attempt to provide more data for a reliable inverse identification [15, 136]. Though it does not in any way resolve the previously mentioned issues with the *P-h* curve, it may allow for a greater perspective for the unique characterization on account of the larger amount of exploitable data available.

All in all, a critical analysis of the available literature presents a solid argument for using the imprint profile and this forms our third motivation for this thesis : to fully study the characterization potential of the residual imprint and its possible influence on the non-unicity of identification, and if possible, develop a protocol based on the use of the imprint. We further note that it is appealing to solve this inverse problem within *a reduced space* since the source of non-uniqueness could be more easily checked if the correspondence between material parameter sets and indentation responses were readily visualized.

1.2 Outline

The thesis is organized in the following manner :

In the current chapter, we have presented the motivations of the current research on the basis of a general analysis of the research background. The tasks to be accomplished are divided into three main headings : to apply manifold learning approaches to the filed of mechanics, to study the identifiability of material parameters using instrumented indentation, and finally to propose new protocols to alleviate non-unicity of the solutions obtained in inverse identification.

In Chapter 2, the state-of-the-art of related subjects is first reviewed in detail. Section 2.1.1 recalls recent developments in the field of machine learning approaches, with special attention paid to those applicable in the field of computational mechanics. This is followed by a comparison of some dimensionality reduction methods in Section 2.1.2. In Section 2.2, we present a number of techniques that are employed in material characterization, while a more detailed review in relating to indentation-based methods is provided in Section 2.3, where both the *reverse* and *inverse* methods are covered. In Section 2.3.3, we also address the non-uniqueness issue usually encountered in identification, which would be the principal focus of our interest in Chapter 4 and 6.

So as to serve as a basis for the development of material characterization approaches proposed in subsequent chapters, in Chapter 3 we introduce, in the context of problems in mechanics, a comprehensive list of basic concepts relating to nonlinear manifold learning. The manifold hypothesis, concept of shape admissibility and shape interpolation are all covered in Section 3.1. The idea of constructing the global manifold in piece-wise fashion is also briefly introduced in Section 3.2. In Section 3.3, a group of numerical tools are presented so as to define the shape space in an exploitable manner, and a criterion to estimate the intrinsic dimensionality is also proposed based on Local linear embedding (LLE). Finally, in Section 3.4 a material characterization problem based on stress-strain curve is employed to showcase the application of the manifold method. In addition to validating the manifold hypothesis,

we also obtain additional advantages such as the ability to glean a deeper understanding of mechanical phenomena involved. It is highlighted that the maximum number of identifiable *independent* material parameters appears to correlate with the *intrinsic dimensionality* of the corresponding global manifold. The content of this chapter, along with two other applications of manifold methods, resulted in a peer-reviewed journal paper [J2].

In Chapter 4 we apply the *global* manifold approach developed in Chapter 3 to the characterization of a material's elasto-plastic parameters using the instrumented indentation test (IIT). In this chapter, we deal with synthetic data without added noise, with the aim of studying the identifiability of Hollomon's parameters in *ideal conditions* and investigating possible influences of indenter geometries and of indentation setups in the simulation. In addition to the force-displacement curve, another available indentation response, the residual imprint, is also considered. The axisymmetric displacement field (obtained from spherical indentation on an isotropic material) and *P-h* curve are treated either separately or together to construct POD snapshots while studying global manifolds. By calculating the objective (minimization) functions to be solved in inverse analysis within a rather large design space, the difficulty in unique parameter identification with only the *P-h* curve is readily visible. The advantages of using the imprints are demonstrated by presenting a one-to-one correspondence between their projections in the low-dimensional shape-space and the material parameter sets. The main results of this chapter can be found in [J3].

In Chapter 5, we validate the insights gleaned from the global manifolds in Chapter 4 by a series of iterative identification procedures. A family of local manifold learning algorithms is developed to explore the design space in different ways, depending on the previously acquired knowledge about the material. Only the useful portions of the manifold are constructed in piece-wise manner, at a moderate computational expense. The identification results confirm that the residual imprint will allow for an easier and unique identification of Hollomon's parameters, even for conical indenters, for which the non-uniqueness issue has been extensively reported. On the other hand, we also try to generalize this conclusion to the identification of Voce's parameters, however, the failure here in getting a unique solution suggests that a single indentation test could be insufficient and the non-uniqueness issue with regard to the calibration of Voce law remains an open subject [C1, C2].

Our focus in Chapter 6 is then to investigate the source of the non-unicity in identifying Voce law. To first rule out any possible inefficacy of the manifold principles and protocol proposed, we carry out in Section 6.1 a series of identifications based on the uniaxial stress-strain curve itself, which is universally accepted as fully interpreting an isotropic material's hardening behavior. The unique identification result obtained suggests that any failure of accurate identification by the indentation test could be attributed to a possible interdependence

between different Voce parameters with respect to the indentation responses. Then, in Section 6.2, we further underline that a single indentation test is inadequate to distinguish Voce hardening materials, leading to the phenomenon of "mystical siblings". After comparing the reconstructed constitutive behaviors, we divide these materials into two groups : the *true* and *false* mystical pairs. For the latter, a multi-depth indentation technique is proposed in Section 6.3. The results reported in this chapter are the subject of [J5].

In Chapter 7, in place of synthetic data, the manifold-based identification protocol is verified using experimentally measured indentation responses. Since the imprint is proposed for obtaining unique solutions in Section 4.7, we retain the same as the focus of this chapter. We underline in this chapter that the manifold approach permits the direct use of the experimental imprint without any preprocessing, since the constructed imprint-manifold provides us with a natural/physics-based way of smoothing the experimental response data. The three metallic materials characterized include an AISI 1095 steel and two aluminum alloys : EN AW-2017F and EN AW-5754F. In view of possible overlappings of lthe ocal searching spaces, a discussion on the reuse of snapshots is anticipated in the closing comments, Section 7.6. The main contributions of this chapter have been published in [J1].

Chapter 8 ends the dissertation with perspectives on future research.

In Appendix A, details about the preparation of specimens for indentation tests are given, and partial identification results for the AISI 1095 steel is also provided in Appendix B. Finally, we give in Appendix C some comments on the robustness of the proposed manifold-based identification method with respect to such numerical parameters as the number of retained POD modes, the order of polynomial basis in manifold approximation as well as the number of snapshots.

Chapitre 2

Literature review on related subjects

The literature review described in this chapter is intended to describe the state of the art in the subjects involved, and set the stage for the chosen orientations for the research work that has been accomplished in this doctoral thesis. It is organized in the following fashion : in Section 2.1.1, we first review the developments and approaches in the field of machine learning which could potentially be applicable to the field of computational solid mechanics. With added emphasis on the reduction of complex physical data, Section 2.1.2 summarizes and compares a series of linear and nonlinear dimensionality reduction methods most frequently used in clustering. Then, focusing on the material characterization problem in Section 2.2, we present a family of mechanical testing methods, in particular the instrumented indentation test which is becoming more and more popular. Section 2.3 presents a dynamic and detailed review of the evolution of indentation-based material characterization. Two groups of methods, i.e., *reverse* and *inverse* analysis, are recalled in Section 2.3.1 and 2.3.2 respectively. Finally, we review all the previous work on the non-unicity issue in property identification in Section 2.3.3.

2.1 Manifold learning approach

2.1.1 Machine learning in solid mechanics

Since its birth in the 1950s [99], artificial intelligence (AI) has evolved into knowledge-based expert systems [18] and machine learning [131]. At the same time, the modern-day maturity of computational engineering results in massive amounts of data while simulating complex physical phenomena with attention to details. On the other hand, modern techniques are trending towards high-precision measurements on a smaller and smaller scale. This combination of high-precision measured and massively-sized simulated data has propelled

the explosive growth of the field of machine learning, making it play an increasingly important role in data-driven prediction and decision-making.

The categorization of machine learning tasks may vary according to diverse criteria. Depending on the availability of input and output to/from the system at hand, [128] generally classified machine learning tasks into three categories : supervised, unsupervised and reinforcement learning. While it originally grew out of the fields of pattern recognition and computational learning theory [60, 137], several applications in the field of computational mechanics may also be interpreted as belonging to the machine learning framework [18, 62, 93, 85, 69]. Promising results have been reported so far in the parameterization of material microstructures [160], in generation of computational patient avatars for surgery planning in biomechanical field [62] as well as in model reduction in finite elasto-dynamics [97, 98], among others.

Supervised learning attempts to "discover" a relationship between the inputs and outputs of training data. Some mature algorithms include decision tree learning [50, 127], linear regression [101], Support Vector Machine (SVM) [42, 52, 149] and Artificial Neural Networks (ANN) [162, 65]. Reduced Order modeling (ROM) in computational mechanics [97, 98, 88, 30] may be classified in this category. This field has been gaining widespread acceptance and is frequently used to approximate high-dimensional physical fields associated with a design problem using a lower-order meta-model [49, 19, 159]. The more popular methods at this point include Proper Orthogonal Decomposition (POD) [10, 41, 6], Proper Generalized Decomposition (PGD) [35, 36, 55, 56] and the Reduced Basis (RB) methods [116, 71, 68].

The corresponding unsupervised procedure is known as clustering since it attempts to group data into different sets based on the measured ”distance” or their inherent similarities. In this case, the inferred function will automatically label each sample entering the learning system. Examples of linear approaches to unsupervised learning include Principal Component Analysis (PCA) [76], Metric multidimensional scaling (MDS) [43] and Singular Value Decomposition (SVD) [61], etc. The well-known Locally Linear Embedding (LLE) [132] and Isomap [7] are unsupervised methods which have the capacity to generate highly nonlinear embeddings. Applications of these algorithms in computational mechanics include reliability-based design optimization (RBDO) [150, 70] and dimensionality reduction of input/output of complex mechanical systems [121, 123].

Semi-supervised learning is a category that lies in between the first two. Even though much of the output is unlabeled in this case, we observe a considerable improvement in learning accuracy when it is used in conjunction with labeled data. Multi-fidelity optimization [146, 72] and multi-level of parameters [47] are two examples of the same.

Finally, in reinforcement learning, machine learning algorithms interact with a dynamic environment so as to perform a certain goal with certain feedbacks in terms of "rewards" and "punishments". However, a description of these algorithms, indispensable for the development of autonomous cars as well as the famous computer program AlphaGo that plays the board game Go, is beyond the scope of this thesis.

As stated previously, in this thesis, our interest lies in mechanical problems where the data collected from FE simulations or from experimental measurement are high-dimensional. For the sake of a better understanding of complex mechanical phenomena, dimensionality reduction algorithms that attempt to condense the physical data or the model in a very light and efficient manner can obviously be quite appealing. With these considerations, the current research interest falls into the category of unsupervised learning. The related algorithms are briefly summarized in what follows.

2.1.2 Dimensionality reduction algorithms

In this section, we review various representative algorithms with consistent terminology and notation, and compare and contrast their capacities of interpolating or projecting new points in the system as well as of evaluating the intrinsic dimensionality. A more detailed survey of many of these algorithms may be found in [25].

Given a high-dimensional dataset $\boldsymbol{X} = \{\boldsymbol{\chi}_i\}_{i=1}^{M} \subset \mathbb{R}^N$, we may assume in this dissertation, without loss of generality, that the input observations/patterns $\boldsymbol{\chi}_1, \boldsymbol{\chi}_2, \cdots, \boldsymbol{\chi}_M$ are centered on the origin of the coordinate system, i.e., $\sum_{i=1}^{M} \boldsymbol{\chi}_i = \boldsymbol{0}$. The raw data, while high dimensional, is essentially confined to a lower-dimensional subspace, whose dimensionality is termed as the "intrinsic dimensionality", d_{int}, which is defined as the minimum number of parameters needed to represent the data without any loss of information [31]. By $\{\boldsymbol{\alpha}_i\}_{i=1}^{M} \subset \mathbb{R}^m$, we denote the coordinates of the raw data described in the low-dimensional subspace. Note that $d_{\text{int}} \leq m \leq N$.

Principal component analysis (PCA)

In PCA, input patterns are projected in the lower-dimensional space by minimizing the reconstruction error

$$\varepsilon_{\text{PCA}} = \sum_{i=1}^{M} \left\| \boldsymbol{\chi}_i - \sum_j \alpha_{i,j} \boldsymbol{\phi}_j \right\|^2, \; j = 1, 2 \cdots m, \tag{2.1}$$

where the vectors $\{\boldsymbol{\phi}_j\}_{j=1}^{m}$ define a partial orthogonal basis of the reduced space, and the original data $\boldsymbol{\chi}_i$ is described by $\boldsymbol{\alpha}_i = (\alpha_{i,1}, \alpha_{i,2}, \cdots \alpha_{i,m})^{\mathrm{T}}$ in this space. Essentially, the

subspace with minimum reconstruction error is also the subspace with maximum variance [133], whose basis vectors are derived from the top eigenvectors of the covariance matrix

$$\boldsymbol{C} = \frac{1}{M}\sum_{i}^{M} \boldsymbol{\chi}_i \boldsymbol{\chi}_i^{\mathrm{T}}. \tag{2.2}$$

Using the directions corresponding to the eigenvectors as principal axes, an orthogonal transformation is then performed to convert the raw data of (possibly correlated) variables into a set of m linearly *uncorrelated* variables called *principal components*. The outputs of PCA, namely the coordinates of input patterns in the subspace, are calculated as

$$\alpha_{i,j} = \boldsymbol{\chi}_i^{\mathrm{T}} \boldsymbol{\phi}_j. \tag{2.3}$$

Note that, the eigenvalues of the covariance matrix in Equation 2.2 correspond to the projected variances of the high-dimensional data along the principal axes. The number of significant eigenvalues is thus an estimate of the dimensionality of the subspace, m, which contains most of the variance of the raw data. Its choice depends on the spectrum of the eigenvalues where a pronounced gap must exist between the m^{th} and the $(m+1)^{th}$ eigenvalues.

Instead of eigenvalue decomposition on $\boldsymbol{C}$, PCA may also be performed by singular value decomposition (SVD) of the data matrix $\boldsymbol{X}$. More details can be found in [76]. We will show later that the basic geometric intuition behind PCA—i.e. maximizing variance—is also useful for nonlinear dimensionality reduction algorithms.

Multidimensional scaling (MDS)

Unlike PCA, MDS attempts to find the subspace for the high-dimensional data that most faithfully preserves the inner products between the input patterns. If the usual Euclidean dot product is adopted, the objective of the minimization problem has the form

$$\varepsilon_{\mathrm{MDS}} = \sum_{ij} (\boldsymbol{\chi}_i^{\mathrm{T}} \boldsymbol{\chi}_j - \boldsymbol{\alpha}_i^{\mathrm{T}} \boldsymbol{\alpha}_j)^2. \tag{2.4}$$

The solution is then found by performing eigenvalue decomposition on the Gram matrix $\boldsymbol{G}$ where

$$G_{i,j} = \boldsymbol{\chi}_i^{\mathrm{T}} \boldsymbol{\chi}_j. \tag{2.5}$$

As with PCA, we retain the m largest eigenvalues $\{\lambda_i\}_{i=1}^{m}$ and the corresponding eigenvectors $\{\mathbf{v}_i\}_{i=1}^{m}$. The low-dimensional representation of the raw data is thus computed as

$$\alpha_{i,j} = \sqrt{\lambda_j} v_{j,i}. \tag{2.6}$$

Though based on somewhat different geometric intuitions, MDS yields the same output as PCA since both methods essentially consist of a rotation of the coordinate system followed by a projection into the subspace of highest variances. Quite obviously, the covariance matrix $\boldsymbol{C}$ in PCA and the Gram matrix $\boldsymbol{G}$ in MDS lead to identical results in spectral decomposition in view of the fact that $\boldsymbol{G} = \boldsymbol{X}^{\mathrm{T}}\boldsymbol{X}$ has the same rank and the same eigenvalues as the covariance matrix $\boldsymbol{C} = \frac{1}{M}\boldsymbol{X}\boldsymbol{X}^{\mathrm{T}}$.

On the other hand, MDS, though designed to preserve inner products, may be interpreted as preserving *pairwise distances*. Knowing *a priori* the matrix of squared distances $\boldsymbol{D}$, composed of

$$d_{i,j} = \|\boldsymbol{\chi}_i - \boldsymbol{\chi}_j\|^2, \tag{2.7}$$

the Gram matrix can also be derived from the transformation

$$\boldsymbol{G} = \frac{1}{2}(\boldsymbol{I} - \boldsymbol{l}\boldsymbol{l}^{\mathrm{T}})\boldsymbol{D}(\boldsymbol{I} - \boldsymbol{l}\boldsymbol{l}^{\mathrm{T}}), \tag{2.8}$$

in which $\boldsymbol{I}$ is the $M \times M$ identity matrix and $\boldsymbol{l} = \frac{1}{\sqrt{M}}(1, 1, \cdots 1)^{\mathrm{T}}$ the uniform vector of unit length. One can refer to [43] for more information on MDS and its extensions.

PCA and MDS are two representative linear methods for dimensionality reduction, and they both generate faithful low-dimensional representations for input patterns confined to a nearly linear structure. However, they could fail if the original data is highly nonlinear. For this reason, nonlinear methods like Kernel-PCA, Isomap and LLE, among others, are used.

Kernel-based PCA (kPCA)

With a user-specified kernel, the linear operations of PCA are performed in a reproducing kernel Hilbert space (also called a high-dimensional feature space), which is related to the input by a possible nonlinear map

$$\begin{gathered} \boldsymbol{\Psi} : \mathbb{R}^N \to \mathbb{F} \\ \boldsymbol{\chi} \to \boldsymbol{\gamma} \end{gathered} \tag{2.9}$$

where $\mathbb{F}$ could have an arbitrarily large dimensionality. The essence of kPCA is first transforming the raw data in such a high-dimensional, implicit feature space before following the

procedures of PCA. Adopting the zero-mean data assumption, the covariance matrix in $\mathbb{F}$ turns to be

$$\bar{\boldsymbol{C}} = \frac{1}{M}\sum_{i}^{M} \boldsymbol{\Psi}(\boldsymbol{\chi}_i)\boldsymbol{\Psi}(\boldsymbol{\chi}_i)^{\mathrm{T}}. \tag{2.10}$$

Note that, kPCA does not necessarily carry out the map $\boldsymbol{\Psi}$ explicitly to the feature space. In contrast, a kernel function is designated over pairs of data points

$$k_{ij} := k(\boldsymbol{\chi}_i, \boldsymbol{\chi}_j) = \boldsymbol{\Psi}(\boldsymbol{\chi}_i)^{\mathrm{T}}\boldsymbol{\Psi}(\boldsymbol{\chi}_j). \tag{2.11}$$

We note that the choice of kernel implicitly determines the mapping $\boldsymbol{\Psi}$ to the feature space. The commonly used kernels are :
(a) polynomial kernels [51] :

$$k(\boldsymbol{\chi}_i, \boldsymbol{\chi}_j) = (\boldsymbol{\chi}_i^{\mathrm{T}}\boldsymbol{\chi}_j + 1)^d, \tag{2.12}$$

(b) radial basis functions :

$$k(\boldsymbol{\chi}_i, \boldsymbol{\chi}_j) = \exp\left(-\frac{\|\boldsymbol{\chi}_i - \boldsymbol{\chi}_j\|^2}{2\sigma^2}\right), \tag{2.13}$$

and (c) Neural Network type [67] :

$$k(\boldsymbol{\chi}_i, \boldsymbol{\chi}_j) = \tanh(\boldsymbol{\chi}_i^{\mathrm{T}}\boldsymbol{\chi}_j + b). \tag{2.14}$$

Notice that the kernel function in Equation 2.12 is essentially a nonlinear map into the high-dimensional space of all d^{th} order monomials in the entries of an input vector. Here, the dot product of vectors mapped by $\boldsymbol{\Psi}$ is calculated in a low-cost fashion. Besides, σ in Equation 2.13 and b in Equation 2.14 are two parameters that depend on the problem at hand, and therefore should be carefully chosen.

For the purpose of principal component extraction, the projections of raw data on the j^{th} eigenvectors in $\mathbb{F}$ are computed as

$$\boldsymbol{\alpha}_j = (\boldsymbol{u}^j)^{\mathrm{T}}\boldsymbol{K}, \tag{2.15}$$

where $\boldsymbol{u}$ are eigenvectors solved from

$$M\lambda\boldsymbol{u} = \boldsymbol{K}\boldsymbol{u}. \tag{2.16}$$

Besides, for an arbitrary observation $\boldsymbol{\chi}$ that has not been considered when constructing $\boldsymbol{K}$, its nonlinear principal components may also be found with the aid of the kernel function

$$\boldsymbol{\alpha}_k = \sum_{i=1}^{M} \boldsymbol{u}_i^k (\Psi(\boldsymbol{\chi}_i)^{\mathrm{T}} \Psi(\boldsymbol{\chi})), \tag{2.17}$$

One should be aware that, even if $\boldsymbol{\chi}$ is centered within the input space $\mathbb{R}^N$, it is non-trivial to achieve this in $\mathbb{F}$, as we can not explicitly compute the mean of the observations in feature space. A work-around for this issue involves slight modifications of the above equations, and can be found in [134].

Isomap

As described above, both PCA and MDS are "distance-preserving". However, the distance between points that are far apart (in the sense of geodesic, or shortest path distance) on the underlying manifold could sometimes be deceptively low, measured by their straight-line Euclidean distance in the high-dimensional input space, Figure.2.1. To deal with the non-linearity of data, Isomap preserves the *intrinsic geometry* of the data as captured in the geodesic manifold distances [147]. Meanwhile, the major algorithmic features of PCA and MDS (i.e., computational efficiency and global optimality) are inherited.

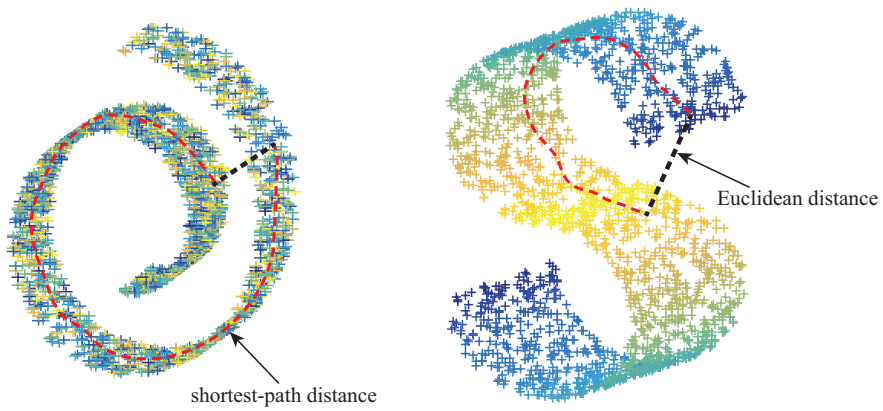

(a) Swiss-roll (b) S-shape

FIGURE 2.1 Inappropriate use of Euclidean distance (red line) in non-linear shape manifold.

The crux of matter is then estimating the geodesic distances between data points. For neighboring points, their geodesic distances may readily be approximated by the Euclidean distance, while for faraway points they are approximated by adding up a series of "short hops" connecting neighboring points, Figure 2.1(a). The three main stages of Isomap include :

1. Depict the neighborhood graph $\boldsymbol{W}$ for the input pattern, where $W_{i,j}$=0 if $\boldsymbol{\chi}_j$ is not in the vicinity of $\boldsymbol{\chi}_i$. The neighborhood can be determined by two different strategies : either we choose all the k nearest neighbors of a given point, or we take all the data points within an *a priori* defined radius r. We note that $\boldsymbol{W}$ may not necessarily be symmetric ;
2. For the graph $\boldsymbol{W}$, we define the edges weighted by the shortest paths $d_{\mathrm{G}}(i,j)$. One must be aware that $d_{\mathrm{G}}(i,j)$ is merely an estimate of the geodesic distance along the manifold (hyper-surface) $d_{\mathrm{M}}(i,j)$, and may be obtained by using Floyd's algorithm, while other algorithms are found in [79] ;
3. Apply MDS to the resulting short-path distance matrix $\boldsymbol{D}_{\mathrm{G}}$ to track the features of original data and embed in low-dimensional space.

We note that the Isomap method is trustworthy only if the local metric structure in the input space is correctly estimated, i.e. a sufficient number of points must be sampled from the structure. In this sense, the shortest path matrix converges to the geodesic distance.

Locally Linear Embedding (LLE)

Like many other algorithms, LLE discovers the nonlinear structure of high dimensional data by exploiting their local symmetries of linear reconstruction. Generally, two common steps are involved : learning the local geometry around each point and embedding high dimensional data into a low dimensional space using the "learned" local information.

For the first step, the underlying geometric properties of the high dimensional data are characterized by a weight matrix. The weights assembled in the i^{th} row minimize the reconstruction error of point $\boldsymbol{\chi}_i$ by its neighbors

$$\boldsymbol{\omega}_i = \underset{\omega_{ij}}{\operatorname{argmin}} \left\| \boldsymbol{\chi}_i - \sum_{j \neq i} \omega_{ij} \boldsymbol{\chi}_j \right\|^2, \tag{2.18}$$

where $\omega_{ij} = 0$ if point $\boldsymbol{\chi}_j$ is not the neighbor of point $\boldsymbol{\chi}_i$. Like in Isomap, this weight matrix is not necessarily symmetric, which may be explained by two reasons : on the one hand $\boldsymbol{\chi}_i$ is the neighbor of $\boldsymbol{\chi}_j$ does not guarantee that $\boldsymbol{\chi}_j$ also lies in the neighborhood of $\boldsymbol{\chi}_i$; on the other hand, even if they are neighbors to each other, the weights ω_{ij} and ω_{ji} probably do not have the same value.

In LLE, the premise is that the local properties of the original data can be characterized by $\boldsymbol{W}$, which should, by design, interpret the embedded low dimensional data as well, leading to

$$\boldsymbol{\alpha}_i = \underset{\boldsymbol{\alpha}_i}{\operatorname{argmin}} \left\| \boldsymbol{\alpha}_i - \sum_{j} \omega_{ij} \boldsymbol{\alpha}_i \right\|^2. \tag{2.19}$$

The cost function in the above minimization problem defines a quadratic form [132]

$$\varepsilon_{\mathrm{LLE}}(\boldsymbol{\alpha}) = \sum_{ij} M_{ij}(\boldsymbol{\alpha}_i^{\mathrm{T}} \boldsymbol{\alpha}_j), \tag{2.20}$$

in which $\boldsymbol{M}$ is computed by

$$M_{ij} = \delta_{ij} - \omega_{ij} - \omega_{ji} + \sum_l \omega_{li}\omega_{lj}, \tag{2.21}$$

where $\delta_{ij} = 1$ if $i = j$, otherwise $\delta_{ij} = 0$. LLE then finds the optimal lower-dimensional embedding system by computing the bottom $d+1$ eigenvectors of $\boldsymbol{M}$, where d is the desired (used-defined) dimensionality of embedded space. Discarding the bottom eigenvector (the corresponding eigenvalue is zero), the remaining d non-zero eigenvectors will then provide an ordered set of orthogonal coordinates of original data in embedded space.

As a popular nonlinear dimensionality reduction method, LLE has key differences from PCA, notably :

— LLE attempts to preserve the centroid of the neighborhood during the mapping, whereas PCA does not make this hypothesis.
— LLE embeds the shapes into a lower dimensional space without explicitly providing us the basis for this space, unlike PCA which permits the insertion of additional points (belonging to the manifold) by projection, as opposed to re-performing the LLE.
— LLE is a global approach, and PCA can be implemented either globally or locally.

Comparison of algorithms

The properties of the algorithms discussed above are compared in Table 2.1. We note that PCA and MDS are both global, linear methods which discover the low-dimensional embedding by studying the connectivity of the dataset within a whole range, while the other three methods intend to characterize the manifold around only a neighborhood. Though being capable of discovering manifold's non-linearity, more parameters, e.g., the number of neighborhood points k, are required to be predefined for nonlinear methods. The choice of k depends however on the number of total points, as well as the configuration of manifold which in most cases is unknown and may vary depending on the problem at hand.

TABLE 2.1 A comparison of diverse dimensionality reduction algorithms

Algorithm	linear	Neighborhood required	Direct insertion of new points
PCA	✓		✓
MDS	✓		
k-PCA		✓	✓
Isomap		✓	
LLE		✓	

On the other hand, in the context of material characterization, we always need to locate/project new points (basically experimental measurements) into the embedding space. It turns out that only PCA and kPCA allow for direct insertion of new points in the reduced space, while a recalculation of basis is always needed for the other methods.

2.2 Characterization of material properties

Material characterization is a fundamental field in material science, without which no scientific understanding of engineering materials could possibly be ascertained. In practice, there exists a great number of mechanical testing methods that aim to determine a material's *geometry-independent* properties, i.e., those intrinsic to the bulk material. A non-exhaustive list of common tests includes : hardness testing, tensile testing, impact testing and fatigue testing, most of which have now been standardized.

In addition, some full-field techniques have been proposed in the last several decades and they are gaining an ever-increasing popularity in material characterization. [64] reviewed the application of full-field measurement techniques until 2004 with a special interest in composite materials. The nature of these techniques mainly includes the measurement of displacement, strain or temperature. Vibration testing has also been employed as an alternative mechanical test with the aim of characterizing mainly the *elastic* properties of materials. Its wide utilization takes root in the strong dependence of vibration behavior on material elastic parameters [83].

Tensile testing among others is commonly performed to characterize the constitutive behavior of a material. However, the development of new materials like plastically graded materials (PGM) [111] as well as the more recent developments in thin films [11] exposed some of the limitations of conventional tensile testing. Moreoever, real engineering structures seldom experience simple uniaxial states of stress in spite of the popularity of uniaxial tension/compression method. It is therefore of great importance to perform tests on small

scales, while stimulating a much complex stress state so as to fully capture the material's plastic behavior.

The instrumented indentation test [102, 143] has provided an exciting solution for this problem, given its non-destructive nature and the complex state of stress produced during the test. It has rapidly become an alternative to the conventional tensile test for characterizing mechanical properties of materials, more importantly, leading to the knowledge of their work hardening properties. This kind of test is similar to a standard hardness test [140], where the hardness is determined by forcing a particular indenter into the material surface by increasing the applied load until a user-defined value is reached, after which the load is either held constant for a short duration before removal or immediately removed. The difference, compared with a hardness test, being that we continuously record the indentation load P and the indenter displacement h during both the loading as well as the unloading phases, generating what we call the P-h curve, as shown in Figure 2.2.

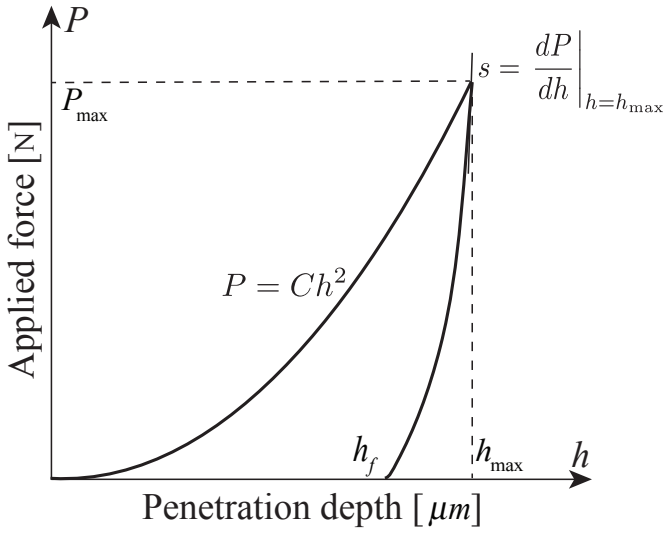

FIGURE 2.2 A typical force-displacement curve (h_f and $h_{\max}$ are the residual and maximum penetration depth, $P_{\max}$ the maximum force).

Together with an improved understanding of the indentation mechanism and advances in numerical methods, instrumented indentation has become an indispensable tool for probing mechanical properties in recent years. Its successful applications have been achieved not just for metals and alloys but also for ceramics [108, 107], hydrated nano-composites such as concrete [39, 154, 77], polymers [152, 87], single crystals [129] and plastically graded materials[106, 115, 59, 104, 103, 138, 4].

At this current stage, there are mainly two ongoing challenges that need to be addressed head-on, related to material characterization. The first is the analysis and processing of

massive data involved, for instance, the displacement field measured with a DIC system and the 3D residual imprint scanned by using a Confocal Laser Scanning Microscope (CLSM). This difficulty is due to the possible absence of direct/explicit relationship between the collected indentation response data and the material parameters to be determined. Though some specific procedures, like reverse and inverse identification, have been proposed to replace the time consuming and expensive trial and error strategy, their abilities need to be improved in order to deal with complex data. Secondly, more studies need to be carried out on the unicity of the identification which has been rarely questioned. This can be vitally important to choose *what* experimental testings need to be performed and *how* to perform them.

2.3 Identification using the indentation test

Over the past 30 years, a steady rise has been seen in the use of indentation test in material characterization. In this section, the two most employed methods, i.e., reverse and inverse method, are reviewed. The concept of "mystical materials" is also introduced.

2.3.1 Reverse analysis

In the pioneering works, the loading and unloading segments of a typical *P-h* curve are generally characterized by several geometric parameters (sometimes called "shape factors"), e.g., the curvature C of the loading phase, the slope s at the beginning of the unloading phase as well as the maximum and residual penetration depth, $h_{\max}$ and h_{f}, Figure 2.2. A group of closed-form dimensionless functions are constructed to relate indentation responses (mainly these shape factors) to elasto-plastic properties [86, 141, 144]. The material parameters are then "calculated" in reverse fashion by using these functions from the shape factors measured from experimental *P-h* curve.

This procedure is accomplished by dimensional analysis (DA), the basic idea of which is that physical laws do not depend on the arbitrariness in the choice of units of physical quantities, and thus should allow the reduction of number of arguments in the functions involved in a complex physical system. The strategy of dimensional analysis is :

1. select dependent/independent variables as well as independent parameters ;
2. identify independent dimensions among the independent parameters ;
3. apply the Buckingham $\Pi-$theorem [1] and define the dimensionless functions.

1. The $\Pi-$theorem states that if there exist a complex physical function which involves a certain number n_0 of physical parameters, it can always be rewritten in terms of only $n_2 = n_0 - n_1$ dimensionless parameters as well as n_1 independent parameters which correspond to the involved physical parameters [66].

Assume we perform the test with a conical indenter (of half apex angle θ) on a material whose constitutive behavior is governed by three parameters : Young's modulus E, initial yield stress σ_y and isotropic hardening coefficient n. If the indentation force P is chosen as a dependent variable, then the indenter penetration depth h, as a consequence, must be the independent variable. Other parameters, like the mechanical properties of specimen as well as those of the indenter can be classified as independent parameters. We consider the indenter to be rigid and the friction between indenter and specimen is negligible, the independent parameters include : E, σ_y, n, θ and Poisson's ratio (ν). The P-h relationship then has the form

$$P = f_L(h, E, \sigma_y, n, \nu, \theta). \tag{2.22}$$

Except n, ν and θ which are dimensionless, we identify two independent dimensions for the other three governing parameters, $[E] = [\sigma_y] = \text{MPa} = \text{N/m}^2$ and $[h] = \text{m}$. Now using the $\Pi-$theorem, we obtain

$$P = Eh^2\Pi(\frac{\sigma_y}{E}, n, \nu, \theta), \tag{2.23}$$

where Π is a dimensionless function whose explicit expression does not exist for complex physical problem, for example, indentation test. By consequence, a smooth functional form can be calculated over a wide range of parameter space by fitting sufficient number of numerical forward analysis [44, 37].

We emphasise that the square dependence in Equation 2.23 between loading force and penetration depth still holds true (except for the definition of the dimensionless function Π) for pyramidal indenters since, like conical indenters, they are geometrically self-similar. Besides, it should also be valid when the friction between indenter and specimen is non-negligible. This is simply because no length scale is introduced in the modeling system as given in Equation 2.22.

Note that, Equation 2.23 is in line with the analytical solution provided by [86], where the force P is proportional to h^2 during both loading and unloading phases, assuming a rigid indenter is forced into *elastic* materials

$$P = \frac{2Eh^2}{(1-\nu^2)\pi} tan\theta = C_e h^2. \tag{2.24}$$

This observation was later generalized to the loading portion of the indentation test of a *rigid-plastic*, or more general, an *elasto-plastic* material. The indentation loading curve can subsequently be described by Meyer's law

$$P = Ch^b \tag{2.25}$$

where b is not necessary an integer ($b = 2$ for conical indenters) and C is a constant determined by material parameters and indenter geometries. Moreover, for cases where the indenter is not necessarily rigid, the load required to penetrate into the solid may be written as

$$P = f_L(h, E^*, \sigma_y, n, \theta) \tag{2.26}$$

where

$$E^* = \left[\frac{1-\nu^2}{E} + \frac{1-\nu_i^2}{E_i} \right]^{-1} \tag{2.27}$$

is the reduced Young's modulus, commonly introduced to include elasticity effect (E_i, v_i) of indenter [74].

Despite fruitful results reported[112, 75, 34, 2], we need to be aware that the functional forms are no longer applicable when either the indenter geometry or material constitutive model is changed. As a consequence, a large number of simulations are required to recalculate the coefficients of these dimensionless functions, which can however be both time-consuming and computationally expensive. We underline also that the $\Pi-$theorem only provides a way of generating sets of dimensionless functions without indicating the most "physically meaningful" expression and the choice of dimensionless parameters is thus non-unique. This explains why different expressions were presented in the available literature [23, 28, 26].

2.3.2 Inverse identification

With the help of deterministic algorithms and FE simulations, the inverse method probes material parameters by minimizing the discrepancy between the measured and simulated indentation responses. Our literature review shows that the recorded *P-h* curve is the primary information adopted, with the corresponding objective function defined in point-wise fashion :

$$J_h(\boldsymbol{\mu}) = \sum_{i=1}^{N_1} \left(\frac{h_i^s(\boldsymbol{\mu}) - h_i^e}{h_{\max}^e} \right)^2, \tag{2.28}$$

where $\boldsymbol{\mu}$ is the vector of material parameters to be identified ; h_i is the instantaneous penetration depth of indenter at time instant $i = 1, 2, 3 \cdots N_1$; the superscript "s" refers to "simulated" by FEM, while the superscript "e" denotes "experimental". Mathematical programming procedures are then used to identify the material properties $\boldsymbol{\mu}$ by solving

$$\boldsymbol{\mu}^* = \arg\min \Big(J_h(\boldsymbol{\mu}) \Big). \tag{2.29}$$

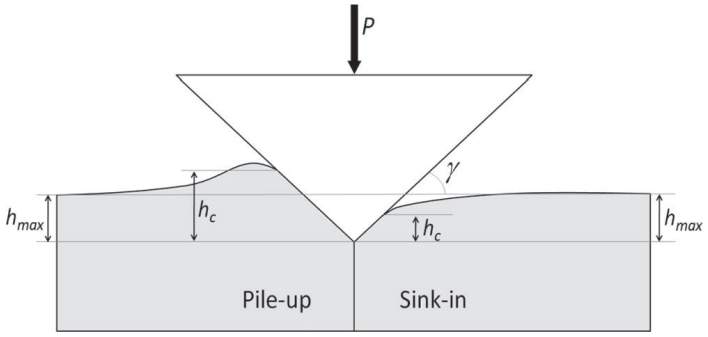

FIGURE 2.3 Schematic diagram showing pile-up/sink-in effects around the indenter tip [126].

Another approach consists of taking into account the residual deformation of the specimen's surface at the end of the indentation test, as additional information to complement the *P-h* curve [1, 145], since different materials generally exhibit diverse plastic pile-up or elastic sink-in effects (Figure 2.3). A review of the existing literature reveals extensive research on combining the traditional indentation test with the mapping of residual deformation (indentation imprint) in order to provide more information for a reliable identification of material properties [109, 105, 90, 13]. An atomic force microscope (AFM) was used by [106] to measure the maximum pile-up observed at the end of the test and eventually obtain a well-defined inverse problem for the Al2024 alloy. Imprint mapping was also employed for the identification of bi-dimensional states of stress [14]. This method was later applied to the identification of graded material properties of thin layers on a substrate in [11]. In the inverse problem of property identification including the imprint shape, the cost function J_h in Equation 2.29 is enriched with the term

$$J_u(\boldsymbol{\mu}) = \sum_{j=1}^{N_2} \left(\frac{u_j^s(\boldsymbol{\mu}) - u_j^e}{u_{\max}^e} \right)^2 , \tag{2.30}$$

where u_j denotes the vertical coordinate of a measured point j with the initial surface of specimen serving as the reference plane ; N_2 is the number of sample points chosen from the specimen surface, and this value depends both on the resolution of the imprint scanning instrument and the density of the FE mesh used. One issue is that the two sources of errors given by $J_h(\boldsymbol{\mu})$ and $J_u(\boldsymbol{\mu})$ cannot be compared numerically. To alleviate this, [106] proposed calibrating each term by a weighting coefficient so as to render them comparable, however, this approach is somewhat *ad hoc*.

The traditional approach for the determination of plastic mechanical properties requires that the indentation load/penetration depth response be obtained with sufficient accuracy and precision [8, 153, 78]. It has been reported that even a small noise in the input data makes

the accurate identification of parameters difficult [29, 156]. Our literature review shows that the indenters have sometimes been simulated as perfectly rigid bodies with the aim of eliminating the nonlinear tip deformation during the indentation test [22, 16]. Other works, like [84], corrected a possible elastic deformation of the indenter by using a system reduced modulus (Equation 2.27) computed from the Young's modulus and the Poisson's ratio of both the indenter and the specimen.

Except for the deformation of the indenter tip, another factor that can greatly affect the accuracy of the *P-h* curve is the indentation frame/machine compliance. Various methods used for the determination of machine compliance can lead to different values of compliance [111], and this is especially difficult in the nanometer scale [155, 78]. Moreover, for spherical indenters (always not mono-bloc), the presence of compound between the indenter and the indenter-holder can lead to a load-dependent compliance [153]. As a result, the obtained *P-h* curve is inexploitable.

Moreover, another difficulty lies in determining the reference point, or detecting the moment when the indenter comes into contact with the specimen surface. The importance of detecting the start point has been pointed out by [63] to guarantee the accuracy of *P-h* curve. [17] recommended to calculate the derivative of the indentation curve in order to limit the effects of a false determination of the zero position. However, if we are interested in solely using the imprint, this problem can be mitigated since a prescribed force is more easily controlled even without knowing the initial contact.

2.3.3 Uniqueness of solution to inverse identification

In a typical identification procedure, it is expected that there exists a one-to-one correspondence between the recorded data and the desired material parameters defining a postulated constitutive law. Unfortunately, the indentation problem is frequently ill-posed, and the existence of different "sibling" materials with distinct properties but nearly identical indentation curves has been revealed more than once, almost since the emergence of the identification method by inverse analysis [34, 148, 2].

Representative work has been reported in [32], where the authors employed the term "mystical materials" to interpret the phenomenon of different parameter sets leading to almost identical indentation *P-h* curves. A mystical material pair $(M_1, M_2)_{\theta=74^\circ}$ is obtained by enforcing the equality of the curvature C of the loading curve (Figure 2.2) using a conical indenter with apex angle $\theta = 74^\circ$. The obtained *P-h* curves for the two materials are observed to overlap with each other, Figure 2.4. Their corresponding uniaxial σ-ε curves are given in the top-left inset.

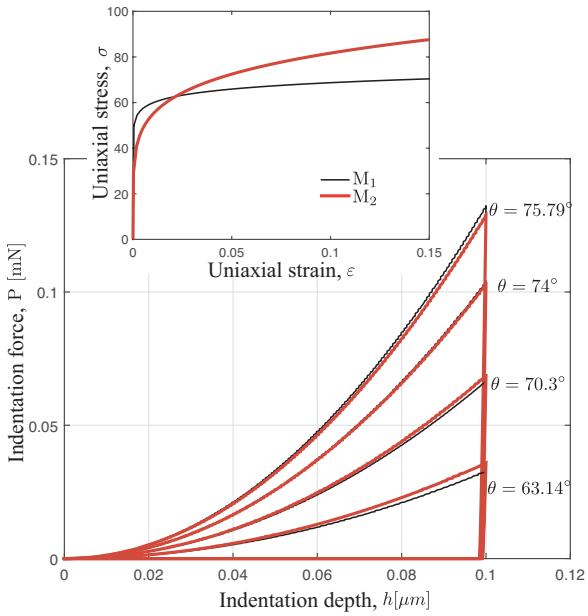

FIGURE 2.4 A mystical material pair, $(M_1, M_2)_{\theta=74°}$, observed by Chen *et al. 2007.*

Therefore, it is of great interest to improve the reliability of the inverse analysis by including more information for parameter identification. Many researchers [37, 54] have proposed adopting a dual sharp indenter to alleviate the non-uniqueness issue [53, 23, 26]. Taking the mystical pair illustrated in Figure 2.4 as an example, Chen *et al.* pointed out that the curves may be distinguished by using dual-sharp indenters, and the difference increases for extreme angles, e.g., $\theta = 63.14°$ and $\theta = 75.79°$ due to differences between the plastic strain fields underneath differently shaped indenter tips [45]. On the other hand, accompanied by the development of high-resolution scanning probe microscopy (e.g., AFM), other solutions were also provided in [15, 12, 11, 125] to also take into account the residual imprint measured with high precision and accuracy.

Although it has been shown that richer information may produce more reliable identification results, the underlying reason has not been revealed or fully discussed, motivating the study of identifiability of parameters in consideration of different indentation responses. Besides, in spite of the information adopted, the identifiability seems to have a close relationship with the geometry of the indenter in view of the fact that the non-uniqueness issue reported mainly focused on sharp indenters [34, 32]. Moreover, to our knowledge, different simulation setups (i.e., prescribed force or displacement) need to be compared to better understand the problem, since the identifiability of parameters (or the sensitivities of cost function of inverse optimization w.r.t. material parameters) may be influenced not only by the measured

experimental response, but also by the way the simulation is carried out. To summarize, the identifiability analysis carried out in this dissertation will answer the following questions :

- What is the influence of the indenter shape (spherical or conical) on the identification result ? Is the non-uniqueness issue also present for spherical indenters ?
- Does the *simulation* setup, i.e., prescribed force or prescribed displacement in indentation, have an influence on the identifiability of parameters ?
- How does the identifiability of parameters differ if different indentation responses (*P-h* curve or imprint shape) are taken into account ?
- Finally, how many parameters can be identified with the measured response data ?

Chapitre 3

Nonlinear shape-manifold learning in computational mechanics

This chapter is devoted to integrating the concepts of manifold learning in the field of computational mechanics. The main reasons that motivate this multidisciplinary integration include : the modern-day maturity of computational engineering producing vast amounts of numerical and experimental data, and the availability of machine learning techniques aimed at the automatic detection of data's underlying structure. Some basic concepts as well as several fundamental techniques will be presented in this chapter and these will serve as a basis for the material characterization protocols presented in the subsequent chapters.

As a preamble to this chapter, we informally introduce the intuition of "manifold" and "shape-manifold". As an important concept in mathematics, a manifold can be thought as a surface of any shape within an arbitrarily high dimension. It does not necessarily have to be a plane, i.e., it may be shaped like a folded sheet, a Mobius ring or a Klein bottle. Employing the term "shape manifold", we intend to mean a group of shapes (after dimensionality reduction) that confine themselves to a manifold. Within the context of computational mechanics, the "shape" refers, in most cases, to diverse structures. It can however, in other cases, be the physical fields of simulation. Note that "structure" and "shape", or even "field" will be employed without special distinction in this chapter.

In the following, we firstly clarify in Section 3.1 some basic concepts involved in the shape-manifold, which include the description of "*shapes*", shape admissibility, hypothesis of shape manifold as well as shape interpolation and projection. Manifold construction and local manifold walking algorithms are explained in Section 3.2. Other involved techniques like Level set method (LSM) and intrinsic dimensionality estimation are presented in Section 3.3. For illustration purpose, we provide a simple 2D example drawn from the field of shape optimization in Section 3.4.

3.1 Basic concepts

In computational mechanics, the term ”shape” is defined in a rather wide range. It could be either a regular geometric shape (design optimization), a final configuration of a structure after plastic deformation (springback in metal forming) or even a continuous physical field (flow field in engine design), depending on the problem at hand.

3.1.1 Shape description

Traditionally, geometric assessment in mechanics uses the Lagrangian approach that attempts to represent a structural shape $\mathbf{\Gamma}$ using a set of primitives : i.e., an array of radii, lengths/thicknesses and angles. This is a very convenient approach in many cases with straightforward geometries, but we quickly get in trouble with problems involving complex structural shapes, e.g., an intricate design such as an engine intake with close to a hundred geometric parameters [92], a formed/deep drawn post-springback shape that cannot be easily expressed as a sum of primitives [121], a residual imprint of indentation test, etc.

The shortcomings of this approach in such cases are due to its inability to adequately describe a complex structural shape $\mathbf{\Gamma}$ without using a very large number of parameters, often exceeding the intrinsic dimensionality d_{int} of the design problem [164, 119]. In addition, the Lagrangian technique does not allow us to easily perform operations such as comparing two different shapes $\mathbf{\Gamma}^{(1)}$ and $\mathbf{\Gamma}^{(2)}$, or calculating the distance between two such shapes, i.e., $dist(\mathbf{\Gamma}^{(1)}, \mathbf{\Gamma}^{(2)})$, which is important for many applications, such as material property characterization, among others. Another implication is the potential generation of inadmissible/infeasible structural shapes before the meshing/solver phase in a computational chain, which could lead to crashes of either the mesh generator or the FE/CFD solver. This is due to the difficulties in expressing all the topological and software-related constraints needed to convert a set of geometric parameters to an *admissible shape* for the problem at hand. The difficulty of calculating gradients is another disadvantage when considering optimization.

Eulerian parameterization approaches are a very attractive option for describing complex shapes or shapes with differing topologies without using geometric primitives. The idea is to use a fixed cartesian grid to represent curves and surfaces using an indicator function $\boldsymbol{\chi}$. Examples of Eulerian representations include pixel/voxel maps, and the more popular level set approach first devised by Osher and Sethian [114] for numerically tracking fronts and free boundaries. Allaire *et al.* [3] then combined the shape derivative introduced by Murat-Simon [110] with the level set concept and recast the shape optimization problem into the topology optimization framework of finding $\boldsymbol{\chi}_{\text{opt}}$ using a Hamilton-Jacobi front propagation algorithm.

Following this, the level set method has also been successfully used to characterize complex shapes, for tracking damage growth [100] as well as for characterizing microstructures [82].

In all, using level set method, we can represent both the idealized shape as well as the actual shape measurement from experiment.

3.1.2 Concept of shape admissibility

Interpolating between neighboring shapes (in Eulerian form) is an attractive and relatively straightforward possibility. There remains however one factor of great importance : shape admissibility for the problem at hand. Admissibility of a shape is a problem-dependent characteristic and this can mean different things in different situations.

In shape optimization, an admissible shape is a shape that satisfies all the technological constraints which are sometimes difficult to express (*e.g.,* tangentiality, connectedness of two sections). For a forming problem, an admissible shape, as defined in [121], represents an actual post-springback shape that is possible to obtain with a given model by manipulating the tool and process parameters in some fashion. This means that a desired target shape may not be possible to obtain, and may therefore be an inadmissible shape for the forming problem if we limit ourselves to realistic post-springback shapes. For a material identification problem based on indentation imprint, using any kind of postulated constitutive law, an admissible shape is a final deformed shape obtainable by manipulating the parameters in said law. However, even though it is *real*, the experimental measured shape may not be admissible for two reasons : the modeling error and the measurement error (although the first could change depending on the chosen law and the second by applying an adapted smoothing procedure).

It should be noticed that the shape admissibility is a completely user-defined concept. Users or engineers need to determine what shapes are ”acceptable” and what shapes are not, according to the case-specific problem at hand.

3.1.3 Concept of shape space

In most cases, we prefer to avoid generating inadmissible shapes, the key then is to interpolate between neighboring admissible level set functions in a way that implicitly satisfies all the admissibility constraints. Traditional shape morphing [48] is not useful in this regard since it assigns an arbitrary set of control points and cannot guarantee admissibility of intermediate shapes generated. So, we intend to develop the shape space $\mathbb{R}^m$ for a given problem using a meta-model for the structural geometry based on the level set formulation.

Some other work in this regard are those of [161] and [158], both of whom used radial basis functions (RBFs).

Basically, the "shape space" (the vector space in which the solution to the mechanical problem evolves) is determined by the problem as well as the manner in which the problem is posed. While this concept, as an abstract notion, has been used in the field of Riemannian geometry [135], there was no tangible way to manipulate this shape space in the context of real life mechanical problems. To get a tangible description of shape space for a design problem, we first assume a discrete representation of "shape" $\mathbf{\Gamma} \in \mathbb{R}^N$, where N is the number of points of definition of the complex shape. For a group of such complex shapes, numerous algorithms exist to find out a reduced-order space, in which each point shall represent a particular shape.

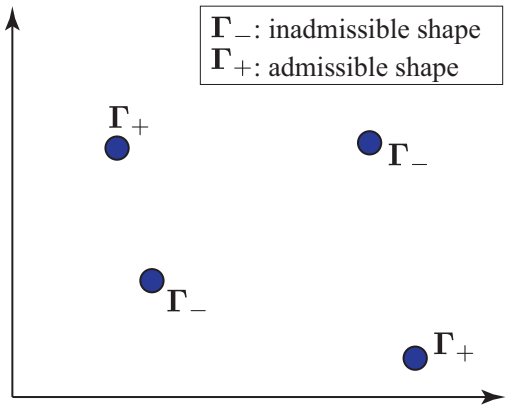

FIGURE 3.1 Concepts of shape space.

According to the concept of shape admissibility in Section 3.1.2, different shapes are distinguished in shape space, Figure 3.1. The admissible and inadmissible shapes are denoted by $\mathbf{\Gamma}_+$ and $\mathbf{\Gamma}_-$, respectively. Now let $\mathbb{A}$ be a set that collects all admissible shapes, then any $\mathbf{\Gamma} \notin \mathbb{A}$ should be inadmissible.

3.1.4 Hypothesis of the shape manifold

According to [119, 124], real-life data points are observed to fill up the space in which they are represented in a non-uniform fashion, in fact, they appear to conglomerate around a lower-dimensional hyper surface. We propose thus a fundamental hypothesis of the existence of a smooth "shape manifold" $\mathscr{M}$ connecting all admissible shape, in the reduced dimensional space $\mathbb{R}^m, m \ll N$, (see in Figure 3.2). The manifold $\mathscr{M}$, on the other hand, may be regarded as a continuous form of $\mathbb{M}$ and the space in which it evolves approaches the true "shape space" of the particular problem with increasing m until N. Furthermore, even though the

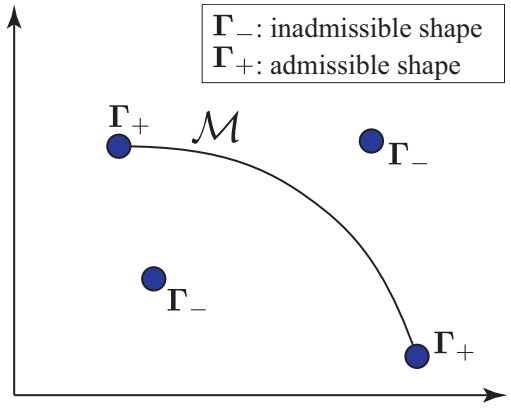

FIGURE 3.2 Shape manifold in shape space.

shapes are much more elegantly described in the shape space, the possible inter-dependence of controlling parameters for a given problem prevents us from representing admissible shapes exclusively. We thus make the assertion that in the m-dimensional shape space, there lies a d_{int}-dimensional manifold, where $d_{\text{int}} \leq m \leq N$ is the *intrinsic* dimensionality of the problem at hand.

In summary, the characteristics of the shape manifold are :

1. all points on the manifold correspond to admissible shapes for the given problem ;
2. any point that lies outside the manifold corresponds to a NON-admissible shape ;
3. the manifold approaches the true shape space for a given design problem with increasing *grid resolution* and sampling density ;
4. the manifold dimensionality d_{int} is the *intrinsic* problem dimensionality.

That said, for some problems, the manifold can be composed of sub-manifolds unconnected to each other due to various constraints and non-continuity of the design space. One can observe such an example in [92].

3.1.5 Shape interpolation

In optimization problems we look for an admissible shape that minimizes a given cost function. We thus need to develop a way of interpolating between admissible instances of shapes while *staying* in the *shape space* restricted to $\mathscr{M}$. This means that the interpolation itself must implicitly satisfy the full set of problem constraints so as to generate solely admissible shapes. The reason for this is that a simple linear combination of two admissible shapes will not necessarily be an admissible shape. This situation is illustrated in Figure 3.3 where linear interpolation between two admissible shapes $\mathbf{\Gamma}_+^{(1)}$ and $\mathbf{\Gamma}_+^{(2)}$, at a given time

t, yields an inadmissible shape $\mathbf{\Gamma}_-^{(t)}$, while an interpolation on the manifold $\mathscr{M}$ gives an admissible shape $\mathbf{\Gamma}_+^{(t)}$. This interpolation in reality must rely on a numerical expression of the manifold in the vicinity of an admissible shape, which will be presented in Section 3.3.2.

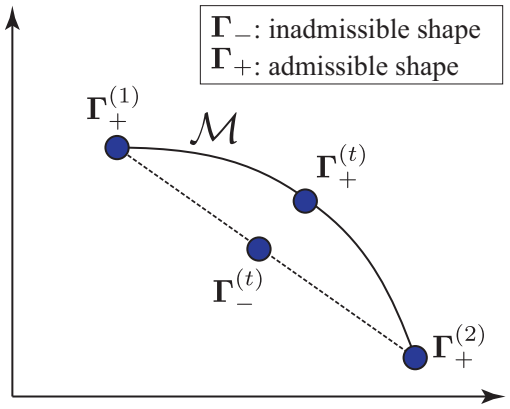

FIGURE 3.3 Shape interpolation along the manifold.

3.1.6 Shape projection

In inverse problems, we typically look for an admissible shape that is closest to the (generally inadmissible) target shape obtained from experimental data. We can obtain the closest admissible shape by simply projecting an inadmissible point onto the manifold. This situation is illustrated in Figure 3.4 where the target shape is denoted by $\mathbf{\Gamma}^{\mathrm{T}}$ and its projection on $\mathscr{M}$ is $\mathbf{\Gamma}^*$.

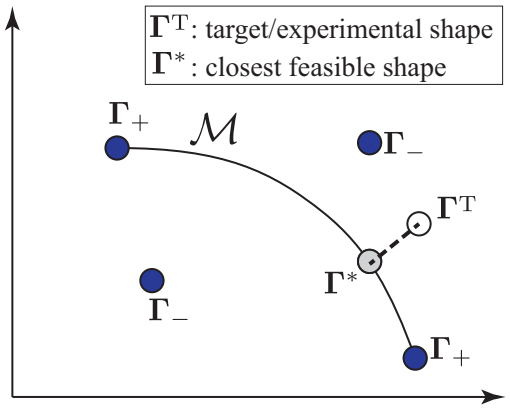

FIGURE 3.4 Projecting a shape on to the manifold.

In identification problems with actual experimentally determined shapes, the target shape $\mathbf{\Gamma}^{\mathrm{T}}$ is clearly not admissible due to the cumulative modeling and measurement errors involved. In other words, the shape $\mathbf{\Gamma}^*$ is the best shape that can be obtained with regard

to the experimental data within the given constitutive law and the experimental setup. The projection error is the distance between $\mathbf{\Gamma}^{\mathrm{T}}$ and $\mathbf{\Gamma}^{*}$.

In springback minimization, the target shape, even without measurement error, may still (and generally will) be inadmissible for design reasons. $\mathbf{\Gamma}^{*}$ corresponds then to the shape that is closest to the target shape, again within a given process model.

3.2 Step-by-step manifold construction

According to our fundamental hypothesis, a *global manifold* is defined as a smooth hyper surface that connects *all* the admissible shapes for a given problem in applied mechanics. However, generating this manifold for a large problem would entail heavy off-line simulations for sufficient accuracy, since it is usually high-dimensional and nonlinear. The main idea here is to project the desired shape onto the surface of shape manifold $\mathscr{M}$ *without* explicitly constructing the global manifold. Instead, we propose an *on-line* approach which constructs only the *useful* portion of $\mathscr{M}$ (local manifold) progressively and the final shape $\mathbf{\Gamma}^{*}$ is then estimated step-by-step.

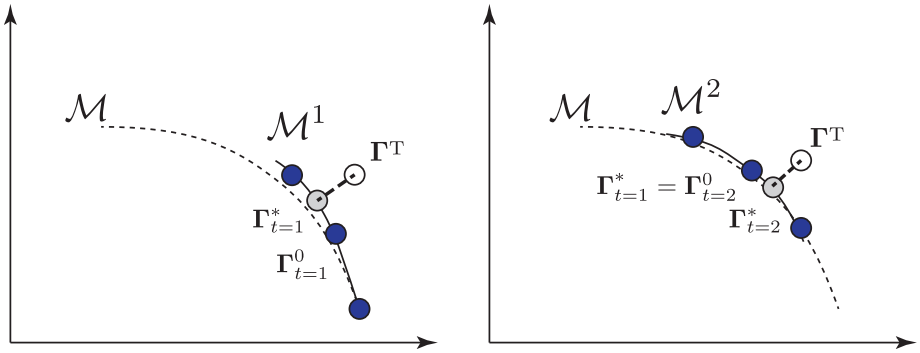

FIGURE 3.5 Local manifold construction by "walking" along the global manifold.

Generally, we begin by obtaining a family of structural shapes $\mathbf{\Gamma}^{(i)}_{t=1}$ for an initial parameter set $\boldsymbol{\mu}^{0}_{t=1}$ and its k neighbors. These shapes can be described in a reduced shape-space, leading to a point-set manifold $\mathbb{M}^1$ in using dimensionality reduction algorithms presented in Section 2.1.2. We then approximate the manifold locally around $\mathbf{\Gamma}^{0}_{t=1}$ by a hyper surface $\mathscr{M}^1$. The desired shape $\mathbf{\Gamma}^{\mathrm{T}}$ is then projected on to this local manifold to get the first estimation $\mathbf{\Gamma}^{*}_{t=1}$ and its corresponding parameters $\boldsymbol{\mu}^{*}_{t=1}$ in design space. In the third step, another hyper surface $\mathscr{M}^2$ is generated around the new point $\mathbf{\Gamma}^{0}_{t=2}$ (which is equivalent to $\mathbf{\Gamma}^{*}_{t=1}$) and we project once again $\mathbf{\Gamma}^{\mathrm{T}}$ on the newly constructed local manifold. This procedure is repeated till convergence.

Note that the choice of k depends on the complexity of the problem (for example $k = 3$ in Figure 3.5), and the transition between point-set to smooth manifold can be completely by Diffuse Approximation [120], as will be presented in Section 3.3.4

3.3 Numerical tools and methods

In order to define the "shape space" in an exploitable manner, we will first use LSM to represent structural shapes. Next we can rely on the dimensionality reduction algorithms proposed in Section 2.1.2 to compute the projection coefficients in the reduced shape space. The inter-relationship between these projection coefficients will then be analyzed to obtain the underlying shape manifold. Due to the simplicity of PCA, it will be adopted as an example.

3.3.1 Level set representation of structural shape

The level set function φ is interpreted here as a signed distance function which describes the propagating front by the minimum distance of an arbitrary point $\mathbf{x}$ to $\mathbf{\Gamma}$ (boundary of shape or structure). By convention, the sign is positive if the point is outside and negative if the point is inside the closed surface Ω. For open surfaces, the sign is positive if the point is above and negative if the point is below, depending on the convention chosen for the normals. The level set approach can thus represent a real-life structural shape $\Omega \in \mathbb{R}^3$ using a three-state indicator function φ where

$$\begin{cases} \varphi(\mathbf{x}) < 0, \ \mathbf{x} \text{ inside } \Omega \\ \varphi(\mathbf{x}) = 0, \ \mathbf{x} \in \Gamma \\ \varphi(\mathbf{x}) > 0, \ \mathbf{x} \text{ outside } \Omega \end{cases}$$

Therefore, the boundary of interest or the *zero level set* at any given time t can be located by finding $\mathbf{x}(t)$ that satisfies

$$\varphi(\mathbf{x}(t), t) = 0. \tag{3.1}$$

The normal direction $\bar{\mathbf{n}}$ to the shape is obtained from

$$\bar{\mathbf{n}} = \frac{\nabla \varphi}{|\nabla \varphi|} \tag{3.2}$$

and the curvature $H = \mathrm{div}(\bar{\mathbf{n}})$. The typical approach to use the level set equation to propagate a moving front over time is to differentiate with respect to time t which yields

$$\frac{\partial \varphi}{\partial t} + \frac{\partial \mathbf{x}}{\partial t} . \frac{\partial \varphi}{\partial \mathbf{x}} = 0 \tag{3.3}$$

giving the Hamilton-Jacobi equation to capture the front propagation of φ with a speed of v

$$\frac{\partial \varphi}{\partial t} - v|\nabla \varphi| = 0. \tag{3.4}$$

Since the analytical form of φ is limited to simple geometries, we need to solve the above equation to track the evolution of a general Γ. But for a given structural shape, the level set function may be efficiently constructed using a fast marching algorithm and a fixed mesh of a cloud of points representing the box $\mathbf{D}$. A discrete value is assigned to each node of this mesh corresponding to the closeness of the node $\mathbf{x}$ to the boundary Γ (Figure 3.6). This gives us a signed distance function $\boldsymbol{\chi}$ whose zero level set is then found using interpolation.

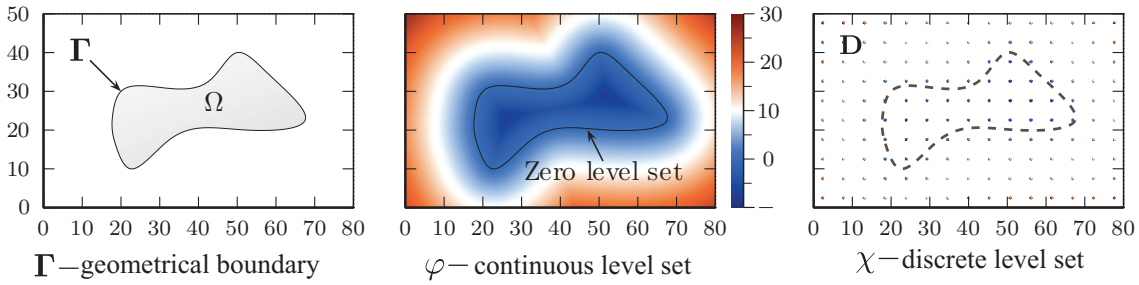

FIGURE 3.6 Generating the signed distance function for a shape Ω using fixed mesh grid.

3.3.2 Shape space constructed by PCA

Now that we have a versatile and complete representation of a structural shape with a discrete level set function $\boldsymbol{\chi}$, the next step is to develop a *tangible* representation of the "shape space" where the structural shape evolves. There are, in theory, various ways to construct the reduced space for complex "shapes". Any of the algorithm presented in Section 2.1.2 is applicable. We focus here on PCA which shall provide us with not only the projection coefficients but also the orthogonal basis, allowing us to project new shapes to the same space.

Considering M level set functions $\boldsymbol{\chi}^{(i)}, i = 1,2\cdots M$, who correspond to M *admissible* shapes (or snapshots), we compute the deviation matrix

$$\boldsymbol{S} = \left[\begin{array}{cccc} \boldsymbol{\chi}^{(1)} - \bar{\boldsymbol{\chi}}, & \boldsymbol{\chi}^{(2)} - \bar{\boldsymbol{\chi}} & \ldots & \boldsymbol{\chi}^{(M)} - \bar{\boldsymbol{\chi}} \end{array} \right] \tag{3.5}$$

centered around the mean snapshot $\bar{\boldsymbol{\chi}}$. Any $\boldsymbol{\chi}^{(i)}$ can then be reconstructed by

$$\boldsymbol{\chi}^{(i)} = \bar{\boldsymbol{\chi}} + \sum_{j=1}^{M} \alpha_j^{(i)} \boldsymbol{\phi}_j \tag{3.6}$$

where

$$\alpha_j^{(i)} = (\boldsymbol{\phi}_j)^{\mathrm{T}} (\boldsymbol{\chi}^{(i)} - \bar{\boldsymbol{\chi}});\ i, j = 1,2\cdots M \tag{3.7}$$

is the projection coefficient for the i^{th} individual snapshot $\boldsymbol{\chi}^{(i)}$ on $\boldsymbol{\phi}_j$. The projection basis, or in other words the orthogonal basis of the constructed shape space, is derived from the eigenvectors of the covariance matrix

$$\mathbf{C}_s = \frac{1}{M} \boldsymbol{S}\boldsymbol{S}^{\mathrm{T}}. \tag{3.8}$$

As a result, the shape space is a M-dimensional space with $\boldsymbol{\phi}_1, \boldsymbol{\phi}_2 \cdots \boldsymbol{\phi}_M$ serve as its basis and each single point in this space described by α-coordinates represents a shape in question. Lastly, we have two remarks to make :

3.3.3 Intrinsic dimensionality estimation

A regular design problem usually involves a parameter array $\boldsymbol{\mu}$ that may include the primitives of geometrical shape, material and process parameters, etc. However, these variables are not always independent, for example in the springback correction problem, the *ad hoc* chosen parameters are sometimes redundant for the shape definition. For a better understanding of the problem itself, the intrinsic dimensionality analysis is necessary. Intrinsic dimensionality is basically the *minimum* number of variables needed to fully describe a problem. In this work, it is denoted by d_{int}. Several algorithms to detect intrinsic dimensionality of dataset are critically reviewed in [25]. In the present work, motivated by [62], a criterion based on LLE neighborhood preservation is proposed as an alternative solution.

LLE "discovers" the underlying nonlinear structure of high dimensional data by exploiting the local symmetries of linear reconstruction. We recall from Section 2.1.2 that two common steps are involved : learn the local geometry around each point and embed high dimensional

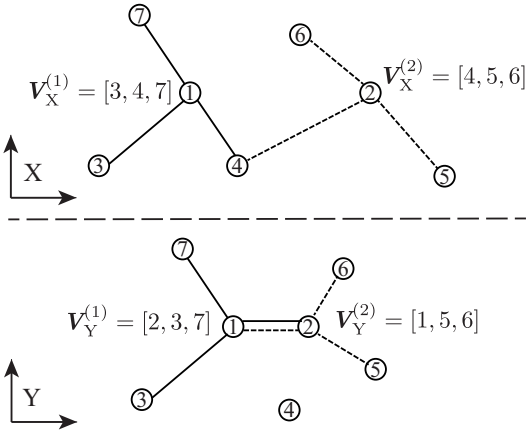

FIGURE 3.7 The connectivity/vicinity of points before and after embedding.

data into low dimensional space using the local information. According to [132], LLE was considered as a neighborhood preserving approach, meaning that neighboring points in a typical vicinity probably remain in the same neighborhood in embedded system. However, this property is not guaranteed by neither Equation 2.18 nor 2.19.

Here, one should be clear about the relationship between weights and neighborhoods. In the original space, weights are calculated from neighborhoods, while in embedded space, this weight matrix allows us to reconstruct a given point from its neighbors in the original space, whereas these points could either be nearby or faraway in the embedded space provided that the reconstruction error in Equation 2.19 is minimized. In this regard, LLE may be considered as a *weight preserving* rather than a neighborhood preserving algorithm. Based on this feature, we thus propose an intrinsic dimensionality criterion by evaluating the faithfulness of embedding (or embedding error).

For illustration purpose, we define two coordinate systems X and Y, referring to the initial and the embedded system, respectively. Let $\boldsymbol{V}^{(i)}$ collect the k closest neighbors of $\boldsymbol{X}^{(i)}$. We first define an intersection operation "$\cap$" between $\boldsymbol{V}^{(i)}$ and $\boldsymbol{V}^{(j)}$ which returns the number of common components in the two sets. Then $card(\boldsymbol{V}_{\mathrm{X}}^{(i)} \cap \boldsymbol{V}_{\mathrm{Y}}^{(i)})$ provides the number of preserved neighbors for point $\boldsymbol{X}^{(i)}$ in two systems. As illustrated in Figure 3.7, $card(\boldsymbol{V}_{\mathrm{X}}^{(1)} \cap \boldsymbol{V}_{\mathrm{Y}}^{(1)}) = card(\boldsymbol{V}_{\mathrm{X}}^{(2)} \cap \boldsymbol{V}_{\mathrm{Y}}^{(2)}) = 2$. Consequently, we propose the concept of "neighborhood preserving ratio" that quantifies the evolution of neighborhood before and after embedding,

$$\gamma(d) = \frac{\sum_{i=1}^{M} card(\boldsymbol{V}_{\mathrm{X}}^{(i)} \cap \boldsymbol{V}_{\mathrm{Y}|d}^{(i)})}{k \cdot M}. \tag{3.9}$$

where M is the number of sample points at hand. By design, this ratio varies between 0 and 1 and could provide us with an insight on the fidelity of embedding in low dimensional

space. Generally, the bigger this value is, the better the neighborhood is preserved. We also expect that the neighborhoods of each point change slightly if the embedding preserves the original information, while change dramatically if the embedded dimensionality d is too small to describe data properly. A telltale gap between $\gamma(d_{\text{int}})$ and $\gamma(d_{\text{int}}-1)$ indicates that the original data lie in a d_{int}-dimensional space. Another way of evaluating the intrinsic dimensionality is to choose a proper threshold value γ_{crit} and calculate the neighborhood preserving ratio in Equation 3.9 while increasing d until $\gamma(d) > \gamma_{\text{crit}}$.

Detecting the intrinsic dimensionality is important in order to explicitly construct the manifold in the reduced space, especially since we do *not* truncate the basis and retain all coefficients. Note that while the algorithm is based on LLE, the actual embedding may be computed using any of the methods introduced in Section 2.1.2.

3.3.4 Shape manifold construction

We now have the projection coefficients for different shapes, giving us a point-set manifold in α-space. The next step then is to globally/locally approximate the shape manifold $\mathbb{M}$ by interpolating between these "shape snapshots" by a smooth α-manifold

$$\mathscr{M}(\alpha^1....\alpha^m) = 0 \tag{3.10}$$

and thus *implicitly* represent all the technological/shape admissibility constraints on the family of structural shapes $\boldsymbol{\chi}(\boldsymbol{\mu})$. Instead of employing all the M coordinates, only the first m dominant ones will be chosen based on an estimate of the intrinsic dimensionality of the problem at hand. In the Diffuse Approximation framework, the parametric representation of $\mathscr{M}$ is approximated with polynomial basis $\mathbf{p}$ and the coefficient vectors $\mathbf{a}^{(j)}$

$$\alpha_j(\boldsymbol{\mu}) = \mathbf{p}^{\mathbf{T}}(\boldsymbol{\mu})\mathbf{a}^{(j)}, j = 1,2\cdots m, \tag{3.11}$$

by minimizing the moving least-square error

$$\mathbf{a}^{(j)} = \arg\min \frac{1}{2}\sum_{i=1}^{m} \omega\left(\boldsymbol{\mu}^{(i)},\boldsymbol{\mu}\right)\left(\mathbf{p}^{\mathbf{T}}(\boldsymbol{\mu}^{(i)})\mathbf{a}^{(j)} - \boldsymbol{\alpha}_j^{(i)}\right)^2. \tag{3.12}$$

Here, ω is the weighting function depending on the distance between evaluation point $\boldsymbol{\mu}$ and the selected snapshots $\boldsymbol{\mu}^{(i)}$, i.e., $\omega := \omega(\|\boldsymbol{\mu} - \boldsymbol{\mu}^{(i)}\|)$. The weights ω_i plays a crucial role in determining how the scattered points influence the smooth manifold, and it insures the continuity and the locality of the approximation. It is defined as positive at $\boldsymbol{\mu}^{(i)}$ and decreases

within a fixed region (called domain of influence) and vanishes outside. One such example is

$$\omega(\|\boldsymbol{\mu}-\boldsymbol{\mu}^{(i)}\|)=\left(1-\frac{\|\boldsymbol{\mu}-\boldsymbol{\mu}^{(i)}\|}{14}\right)^2. \tag{3.13}$$

Though Diffuse approximation allows the transition from the *point-set* to *smooth* manifolds, it would be difficult to make a general assessment for the accuracy of the approximation, since the numerical error due to interpolation would depend on the problem dimensionality, the neighborhood density (distances), number of neighbors, the degree of polynomial used etc. A detailed analysis of the approximation error for a general problem, although not within the context of the manifold is a central subject in [21].

3.4 An illustrative example : manifold approach in material characterization

To help understand the manifold-related concepts presented above, we simply construct in this section a series of manifolds considering diverse material constitutive behaviors as special *"shapes"*. The advantage of manifold protocol in predicting the number of identifiable material parameters is illustrated on three different laws : the Hooke's, the Hollomon's and the Voce law.

3.4.1 Material laws

In view of its simplicity, the Hooke's law characterizing an elastic deformation using one single parameter (Young's modulus E) is omitted here, while the two other laws are briefly presented as below.

Two-parameter Hollomon's power law

Following [15, 32], the power Hollomon's law is generally assumed for studying metallic material. The stress-strain curve under uniaxial tension is given in the form

$$\begin{cases}\sigma=E\varepsilon, & \text{for } \varepsilon<\dfrac{\sigma_y}{E}\\ \sigma=K\varepsilon^n, & \text{for } \varepsilon\geq\dfrac{\sigma_y}{E}\end{cases} \tag{3.14}$$

where σ is the uniaxial stress, σ_y the initial yield stress, ε the total strain and n the work hardening exponent. The constant $K=\sigma_y\,(E/\sigma_y)^n$ is obtained from the continuity constraint

at $\sigma = \sigma_y$. This constitutive law generally defines a quasi-static material with isotropic power hardening.

Three-parameter Voce equation

The Voce uniaxial σ-ε relationship is defined in piecewise fashion [163]

$$\begin{cases} \sigma = E\varepsilon \\ \sigma = \frac{\sigma_y}{1-m_1}(1 - m_1 e^{-m_2 \varepsilon_p}) \end{cases} \tag{3.15}$$

with three parameters : σ_y and dimensionless m_1 and m_2, that control the plastic hardening behavior. This description is of potential interest for calculating the so-called "representative strain" using dimensional analysis [34, 44]. Its another variant

$$\sigma = \sigma_y + Q(1 - e^{-\gamma \varepsilon_p}) \tag{3.16}$$

depends on $Q = \sigma_s - \sigma_y$, which is the difference between the saturation stress σ_s and the

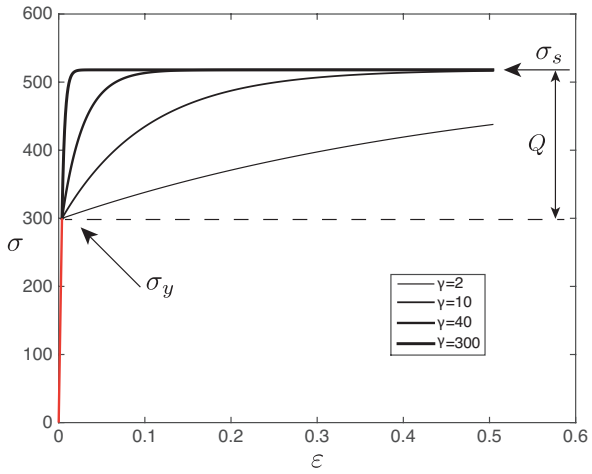

FIGURE 3.8 Voce law with three hardening parameters : σ_y, Q and γ.

initial elastic limit. Essentially, $Q = \frac{m_1}{1-m_1}\sigma_y$ is a function of σ_y and m_1. Like m_2 in Equation 3.15, the parameter γ controls how "rapidly" the stress approaches the saturation level, and it may vary in a range wide enough to accommodate large class of strain hardening engineering materials : from bilinear elasto-plastic ($\gamma = 2$) to elastic-perfectly plastic ($\gamma = 300$), Figure 3.8.

Generally, in the identification of these two latter laws, we focus rather on the material hardening/plastic properties whereas the Young's modulus is considered known a priori. In

this sense, respectively 2 and 3 parameters are to be probed in the identifications of the two constitutive laws.

3.4.2 Comparison of manifolds based on σ-ε curves

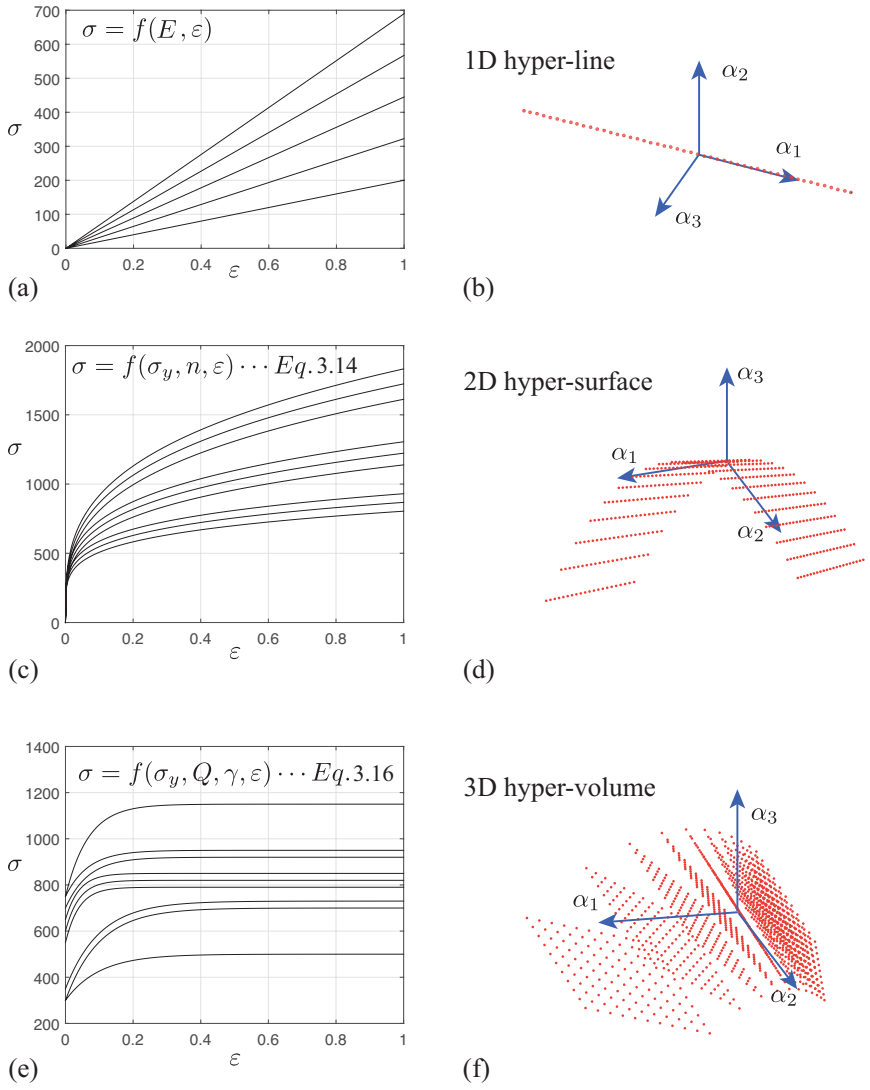

FIGURE 3.9 Illustrative stress-strain curves and the corresponding low-dimensional embeddings for (a)-(b) perfectly elastic (Hooke's law), (c)-(d) Hollomon's power law hardening, and (e)-(f) Voce law hardening

For the Hooke's law, we define a group of 50 tensile curves varying $E \in [200\,\text{Gpa}, 800\,\text{Gpa}]$. For the other two material laws, a series of σ-ε curves are constructed based on an 11 levels full factorial Design of Experiments (DoE) within the following parameter intervals (with

fixed $E = 210$ GPa) : $\sigma_y \in [100\text{ Mpa}, 300\text{ Mpa}]$ and $n \in [0.1,\ 0.4]$ for Hollomon's law, and $\sigma_y \in [300\text{ Mpa}, 800\text{ Mpa}]$, $Q \in [200\text{ Mpa}, 400\text{ Mpa}]$ and $\gamma \in [10,\ 60]$ for Voce hardening.

On the left of Figure 3.9, we show a series of representative stress-strain curves for the three selected material constitutive laws. In this example, these σ-ε curves are *directly* considered as the high-dimensional input "shapes". Instead of employing the level set method as presented in Section 3.3.1, they can be easily characterized by a vector of stresses interpolated on a fixed grid of strains varying between 0 and 1. Following Equation 3.5-3.7, for the corresponding stress-strain curves of each material law, we find out a reduced shape space, into which the synthetic curves are projected. The analysis of resulting patterns of points in the embedded space illustrated on the right of Figure 3.9 allows us to conclude that :

— for Hooke's law, the set points corresponding to different instances of stress-strain behavior of perfectly elastic material is readily observed to lie on a straight line in the reduced space, Figure 3.9 (b) ;

— for Hollomon's power law hardening materials, we observe that the projections are arranged in a regular fashion, showing an intrinsicly 2D hyper-surface, Figure 3.9 (d) ;

— for Voce hardening law, we observe that the material behavior curves are mapped to a 3D cloud of points, taking the form of a "multi-layer sandwich", Figure 3.9 (f) (indicating an intrinsic dimensionality of 3 as expected).

We conclude that in all cases, the parameters defining the constitutive laws are independent in view of an intrinsic dimensionality of 1, 2 and 3, respectively. Figure 3.9 may also promote us to hypothesize a relationship between the number of identifiable parameters and the intrinsic dimensionality of the manifold of admissible shapes within the reduced-order space. This will be further validated in Section 6.1.

3.4.3 Classifying material behaviors

Then, we also try to plot the three manifolds w.r.t different material behaviors within the same shape space. Unlike in Section 3.4.2, the sampled tensile curves are assembled in a single snapshot matrix, on which we perform a global PCA, resulting in a reduced basis $\mathbf{\Phi}^{\text{ela, ep}}$. In this space we depict the projections of σ-ε curves for the three laws using different colors, Figure 3.10.

Quite obviously, we observe that all the stress-strain curves are automatically clustered into three groups of point clouds, which illustrates one of the potential advantages of manifold method in predicting according to which law a material hardens. Suppose now that we have an experimentally measured tensile curve for an unknown material, employing the manifold hypothesis, we may try to predict which constitutive law the material most probably follows

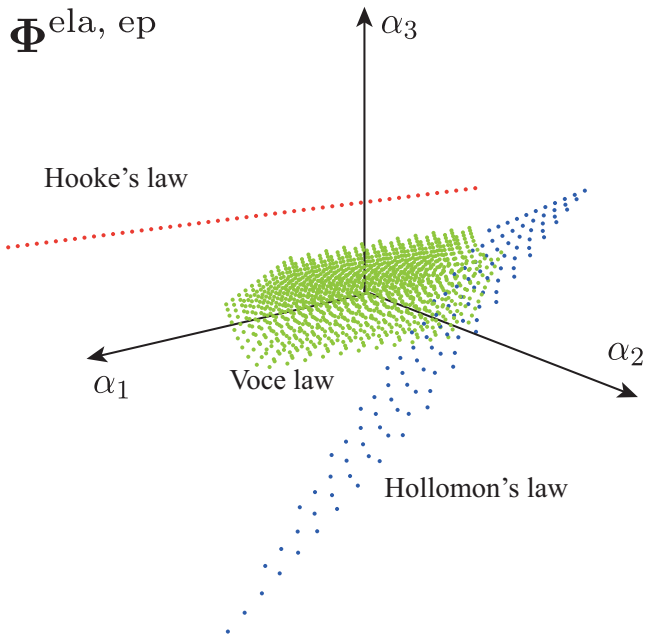

FIGURE 3.10 Reduced shape space constructed for three different constitutive laws.

by simply projecting this curve into the common shape space and examine its distances to different point clouds.

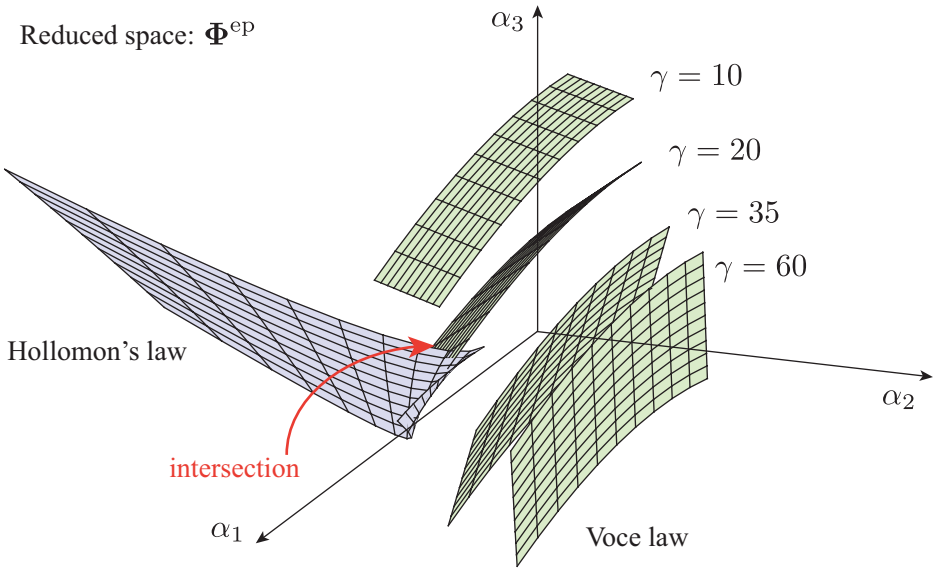

FIGURE 3.11 Reduced space constructed for elasto-plastic materials hardening according to either Hollomon's or Voce law.

We notice also that the 3D manifold w.r.t the Voce law in Figure 3.9 (f) seems to degrade to a 2D one as in Figure 3.10. We attribute this to the possible influence of the Hooke's law, since its elastic behavior was designed to vary in a large range ($E \in [200,\ 800\text{GPa}]$) in contrast to a fixed Young's modulus for the other two laws. To verify this, we subsequently focus only on elasto-plastic material behaviors and the curves belong to Hooke's law are thus eliminated form the snapshot matrix, and consequently another reduced shape space $\mathbf{\Phi}^{\text{ep}}$ is reconstructed in Figure 3.11 for materials having the same elastic property, i.e., $E = 210$ GPa. We observe a regular 3D point cloud for the three-parameter Voce law.

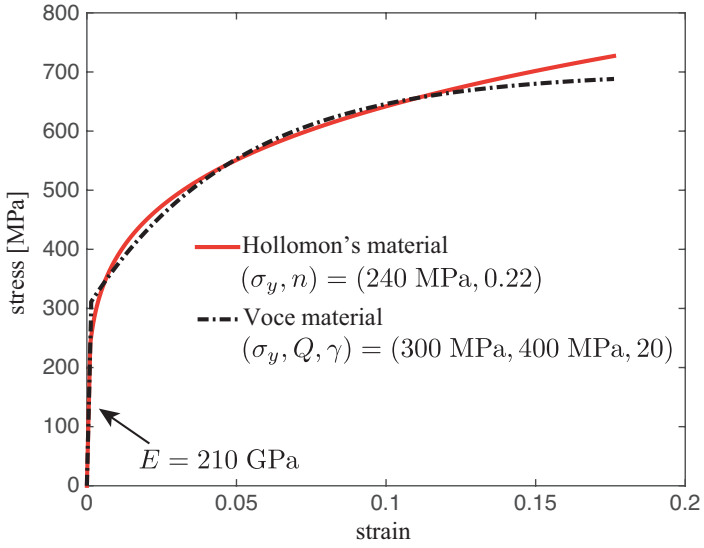

FIGURE 3.12 Possibility of using two different laws to characterize similar materials.

More interestingly, an intersection is observed between the Hollomon's and the Voce manifold, Figure 3.11. We therefore choose, from this intersection zone, two close points belonging to different material behaviors and reconstruct their tensile curves in Figure 3.12. It is observed that the two material behaviors defined by two constitutive laws are quite similar, which signifies that some materials could be characterized by either models. This will be further investigated in Chapter 7 with engineering materials.

3.5 Closing remarks

In this chapter, we have first introduced the basic concepts involved in manifold learning approach. Several related numerical techniques, including level set method, intrinsic dimensionality estimation, and manifold construction by dimensionality reduction algorithm, were also presented. We have also provided a synthetic example based on several material

constitutive laws to demonstrate the advantage of manifold method by illustrating the correlation between the intrinsic dimensionality of problem and that of the corresponding manifold. Moreover, another potential advantage of manifold in predicting which law a material follows is also discussed.

In the next chapter, we make a further step towards the application of the proposed approach to indentation-based material characterization. The data to be reduced will be more complex, capturing the nonlinearity of the tested material. By using the same protocol, we intent to investigate the identifiability of different plastic parameters while considering different indentation responses : *P*-*h* curve and imprint.

Chapitre 4

Global manifolds based on diverse indentation responses

In this chapter, we will concentrate on applying the manifold-learning approach developed in Chapter 3 to the problem of indentation-based material characterization. Unlike conventional methods that focus on correlating *P-h* curves, the full-field measurement of residual imprint will be considered in addition. This subject is challenging from both the aspects of *dimensionality reduction* as well as of *material characterization*, in view of the complexity of the measured data and possible influences of indentation setup, e.g., the indenter geometry and the applied boundary conditions.

Throughout this chapter, synthetic imprints and *P-h* curves are used without adding any noise with the aim of first validating the manifold approach. A series of indentation responses simulated by varying the material parameters will then be compared in the constructed reduced order shape-space. Note that, in contrast with iterative identification process, only analysis of objective function is involved at current stage. The existence or not of one-to-one correspondence between material parameter set and indentation response is investigated. Moreover, the advantages of imprint profile over *P-h* curve and the benefit of prescribing displacement in simulation are also demonstrated.

This chapter is organized in the following manner : the indentation simulation model is first presented in Section 4.1 with several fundamental hypothesis to set the stage for the study in current chapter. Different conditionings in inverse identification are briefly discussed in Section 4.2. Section 4.3 demonstrates the construction of diverse snapshots with regard to different indentation boundary conditions. A series of global manifolds are then compared in Section 4.4 for the purpose of visualizing possible existence of "mystical materials" that can not be well distinguished by a single indentation test. In Section 4.6 some discussions are anticipated with a view to the conditioning of indentation-based identification. We finally

illustrate the existence of a unique solution in identifying Hollomon's law in Section 4.7. Closing remarks are given in Section 4.8

4.1 Finite element simulation

In the simulation of the indentation test, most of the forward analysis models [33, 16, 151, 22, 11] are based on the following hypotheses about the specimen and the indenters :

— the small compliances of the measuring system and of the indenter tip may be neglected ;

— the bulk materials are considered as homogeneous and free from surface residual stresses ;

— the penetration depth of the indenter tip is sufficiently deep, rendering both the "size effect" and indenter tip bluntness negligible ;

— the Poisson's ratio, albeit having a slight impact on the indentation response, is considered as known *a priori*.

While some of these hypothesis may be too restrictive to be applicable to other cases, they are still considered as acceptable when indenting the large majority of bulk materials in micro-scale, especially for investigating the idenfiability of material parameters in using different indentation responses.

4.1.1 Finite element model

Two different indenters are studied. One has a spherical tip with a radius of $R = 0.5$ mm, the other is conical with a semi-opening angle of $70.3°$. The simplicity of their cylindrical symmetry makes them appealing from a modeling standpoint, since the hypotheses of homogeneity and isotropy of the material allows us to use a 2D axisymmetric model. On the other hand, the conical indenter is also attractive because the complications associated with stress concentrations at the sharp edges of the indenter are absent (in comparison with pyramidal ones). The spherical indenter, available from many manufacturers, is widely used especially for micro-scale indentation.

The discretizations of indenters and of the specimen are shown in Figure 4.1. A dense mesh is employed near the interest zone where contact is present between the two pieces. Besides, to approximate the semi-infinite domain condition, a rather large size of the specimen is chosen, 50 mm $\times$ 50 mm, and axisymmetric boundary conditions are selected for both the specimen and the indenters. The indentation system is modeled with ABAQUS/Standard involving 4394 four-node axisymmetric elements CAX4R for the specimen, 6070 elements

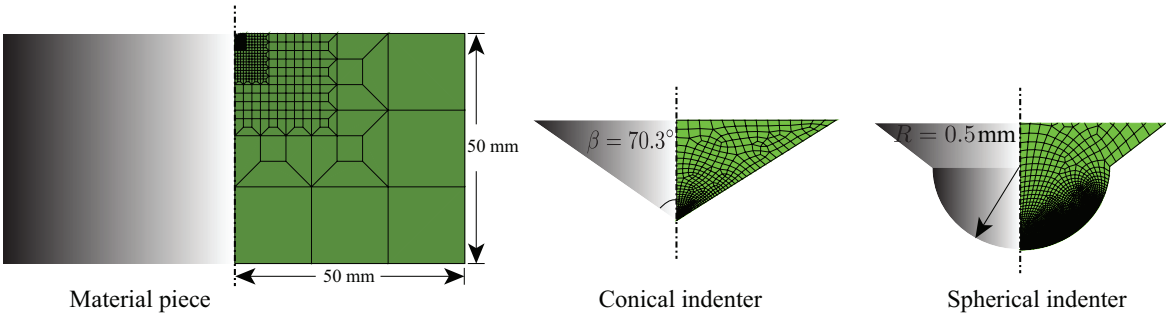

FIGURE 4.1 Finite element model of specimen and different indenter tips.

for spherical indenter and 510 elements for conical indenter. The contact interface between the two pieces is characterized by Coulomb friction coefficient μ. For the two indenters, Young's modulus $E_i = 600$ GPa and Poisson's ratio $\nu_i = 0.23$ are assigned to approximate the elastic properties of Tungsten carbide. The elasto-plastic behavior of the specimen is defined by multi parameters of different constitutive models. In this chapter, the elastic deformation of the specimen is characterized by $E_s = 210$ GPa and $\nu_s = 0.3$, referring to the mechanical parameters of steel.

In this chapter, the power Hollomon's law is assumed for the studied metallic material following research works in the domain [15, 32]. In Abaqus simulation, the corresponding plastic hardening property is interpreted in FE model by defining a table of von Mises stress versus the equivalent plastic strain despite that both the stress and strain are second rank tensors. This is simply based on the underlying assumption that the hydrostatic components of both stress and strain are negligible which is fairly reliable for our case, i.e., elasto-plastic metallic material.

It is also noticed that both indenters are considered geometrically perfect and no wear-out is present. Though an elastic singularity is likely to be present at the tip of the cone [58], the plasticity tends to decrease this effect and more evenly distribute the pressure [113].

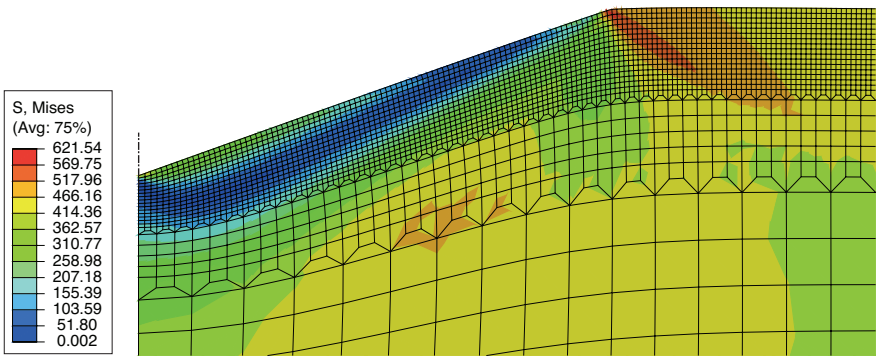

FIGURE 4.2 Stress field in the specimen after indentation with a perfectly sharp indenter.

Therefore, from numerical point of view, the elastic singularity will be attenuated when an elasto-plastic model is concerned. By consequence, the material around the indenter tip starts to plastify immediately from the beginning of contact while the maximal stress will always be bounded by the current elastic limit according to the hardening model. This is coincident with the simulation result (Figure 4.2) obtained with no finite radius on indenter or modification to the standard FE procedure. As observed, the stress concentration is present around the pile-up zone rather than at the indenter tip after indenter removal. The influenced zone of singularity, in good agreement with [58], is rather small (around an element size) thus can be neglected without an impact on the simulation.

4.1.2 Different boundary conditions

The typical indentation curve in Figure 2.2 is generally obtained from two main components in the facility : the displacement sensor and the load cell. In the majority of situations, the indentation test is carried out by forcing an indenter into the material surface by increasing the applied load until a pre-defined threshold value is reached (namely *prescribed force*). Another possibility is to control the whole procedure by a maximum penetration depth of the indenter in the specimen, called *prescribed displacement* control. In both cases, the test cycle involves two phases : the loading phase and the unloading phase.

From the experimental point of view, the same indentation response and therefore the same kind of experimental information shall be obtained regardless of the way the experiment is controlled (by force or displacement). In the context of numerical simulation, though both boundary conditions are applicable to match with a given final state of loading phase (that of the experiment), the choice may influence the difficulty level of inverse identification, thus is studied in Section 4.4.

4.2 The conditioning of the inverse identification problem

The condition number, or conditioning of a numerical problem, is a frequently used concept to determine whether or not a problem is well-behaved. In the problem of the inverse identification of material properties by indentation, we always "hope" to find the *unique* parameter set that will produce the desired, i.e., the experimentally measured mechanical response, which could either be the *P-h* curve or the residual imprint. For a simple two-variable problem, Figure 4.3 shows the different types of conditioning that are frequently encountered in inverse identification, they are :

— **ill-posed** : A one-to-one correspondence does not exist between the material property pairs, (μ_1, μ_2), and the indentation responses, or in other words, more than one pair of material properties will produce nearly "indistinguishable" indentation responses, cases (b) and (d).
— **well-posed** : Any two different materials may be distinguished by their indentation responses, and as a result, there must be one and only one material parameter set that will lead to the "desired" response after FE simulation, case (c) ;
— **ill-conditioned** : The unique identification of model input (material parameters) from the indentation response, though possible in theory, is prone to large numerical errors due to an attenuation of the difference between their indentation responses, case (e).

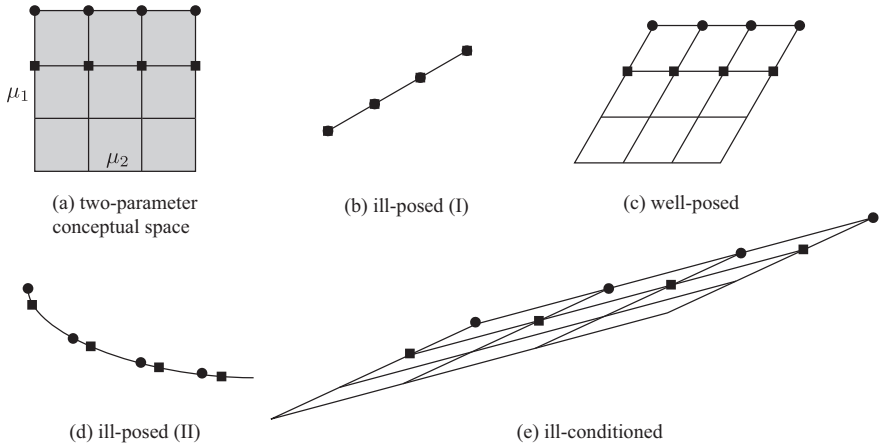

FIGURE 4.3 The three possible conditionings of an inverse problem : (a) input space of a two-variable physical model, and (b)-(e) diverse situations of model outputs within condensed space.

We observe that, for case (b), the output of the analysis model is insensitive to one of the two parameters, μ_1, and thus only μ_2 can be correctly identified. Similarly, the simultaneous identification of two parameters is impossible for (d) as well, since an interdependent influence of the two parameters on the simulation output is observed. However, we still note that the identification of one of the parameters is achievable if the other is known *a priori*. In addition, for cases like (e), the identification of both parameters, though theoretically possible, can prove to be a thorny task, especially with the presence of measurement errors. (c) presents the only situation where we can readily identify both parameters.

Note also that the conditioning of the inverse analysis may vary significantly when different sets of data are used, or when different boundary conditions are employed. The main objective of this section is to understand the non-unicity in identification and to alleviate it by designing different indentation tests. A general solution would be to involve additional experimental data. However, the major concern is whether the supplementary data provides

new information that is *independent* of that already obtained from the existing data. Therefore, the study of the conditioning of the problem is of vital importance.

On the other hand, both the indentation curve and the residual imprint are high-dimensional [91]. This renders the relationship between material parameters and indentation response much less intuitive as illustrated in Figure 4.3. A condensed expression of the indentation responses is therefore needed. The machine learning-inspired nonlinear dimensional reduction algorithms showcased in Section 2.1.2 may serve this purpose and will be employed on indentation responses in the following of this chapter.

4.3 Describing indentation quantities in reduced space

In Section 4.3.1 we present first the characterization of indentation responses. After performing dimensionality reduction on a series of indentation responses, these indentation curves and imprints are then described in the reduced shape-space in Section 4.3.2.

4.3.1 Constructing snapshots from indentation quantities

As stated in the preamble, three kinds of information are employed for identification in literatures : the *P-h* curve [112, 75, 34, 2], the residual imprint [94, 24, 136, 157] and the combination of *P-h* curve and total/partial imprint[15, 11]. We shall start with a typical imprint profile obtained for a homogenous material with an axisymmetric spherical indenter, Figure 4.4. The vertical displacements of the surface nodes are interpolated over a grid of l points and are stored in vector form

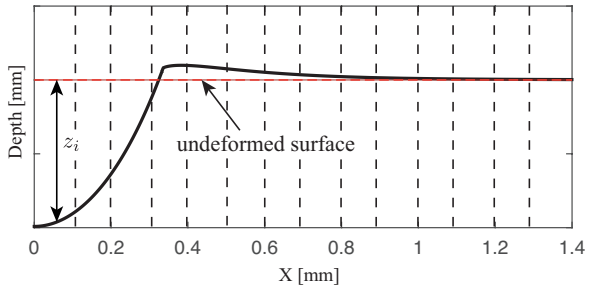

FIGURE 4.4 Snapshot definition depending on a typical imprint obtained from a spherical indenter.

$$\boldsymbol{s}_{\mathrm{I}} = (z_1, z_2, \cdots, z_l)^{\mathrm{T}} \tag{4.1}$$

where l is chosen according to the density of FE mesh (for simulated imprints) or the resolution of microscope (for experimental measured ones). The subscript "I" refers to "imprint".

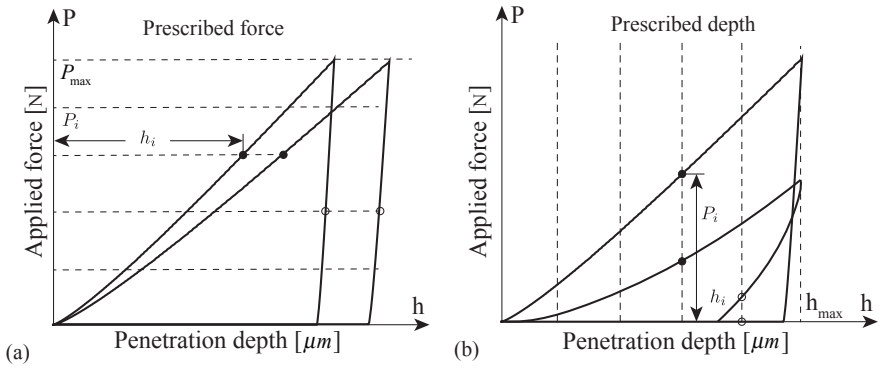

FIGURE 4.5 Snapshot definition depending on *P-h* curves with different boundary conditions.

Unlike imprint, the indentation curve is a multi-value function between the force and penetration depth. For the purpose of interpolating between different indentation curves, the loading and unloading parts are considered separately. As a consequence, the *P-h* snapshots have different descriptions, depending on the chosen boundary condition (natural/essential). For a prescribed force case, Figure 4.5 (a), the penetration depths h_i in both phases can be interpolated over a series of given load increments, yielding $h_i = h(P_i), i = 1,2,\cdots,p+q$, where p and q are the number of loading and unloading increments. The two phases are then characterized by the snapshot vectors with subscript "L" and "U", respectively

$$\boldsymbol{s}_{\mathrm{L}} = (h_{\mathrm{L},1}, h_{\mathrm{L},2}, \cdots, h_{\mathrm{L},p})^{\mathrm{T}}, \quad \boldsymbol{s}_{\mathrm{U}} = (h_{\mathrm{U},1}, h_{\mathrm{U},2}, \cdots, h_{\mathrm{U},q})^{\mathrm{T}}. \tag{4.2}$$

Similarly, for the case where a maximum penetration depth $h_{\max}$ is prescribed (Figure 4.5 (b)), the same interpolation steps are followed except that we record forces for different penetration depths : $P_i = P(h_i)$. It should be noted here that the unloading portion also includes the segment overlying the h-axis. Consequently, the snapshot of indentation curve obtained with prescribed displacement consists of

$$\boldsymbol{s}_{\mathrm{L}} = (P_{\mathrm{L},1}, P_{\mathrm{L},2}, \cdots, P_{\mathrm{L},p})^{\mathrm{T}}, \quad \boldsymbol{s}_{\mathrm{U}} = (P_{\mathrm{U},1}, P_{\mathrm{U},2}, \cdots, P_{\mathrm{U},q})^{\mathrm{T}}. \tag{4.3}$$

The concatenated *P-h* snapshot

$$\boldsymbol{s}_{\mathrm{C}} = \begin{pmatrix} \boldsymbol{s}_{\mathrm{L}} \\ \boldsymbol{s}_{\mathrm{U}} \end{pmatrix} \tag{4.4}$$

then characterizes the whole indentation curve and guarantees the comparability of *P-h* snapshots in identification. Finally, we can also construct a snapshot (of dimensionality $N = l + p + q$) which combines the indentation curve with the imprint, reading

$$\boldsymbol{s} = \begin{pmatrix} w \times \boldsymbol{s}_{\mathrm{I}} \\ (1-w) \times \boldsymbol{s}_{\mathrm{C}} \end{pmatrix}, \; w \in [0,1] \tag{4.5}$$

where w is the weighting coefficient. We underline here that $\boldsymbol{s}_{\mathrm{I}}$ and $\boldsymbol{s}_{\mathrm{C}}$ are normalized before concatenation since they may contain quantities with greatly differing units. This snapshot degrades to Equation 4.1 for $w = 1$ and to Equation 4.4 for $w = 0$, and $w = 0.5$ signifies an equal-weighted contribution of *P-h* curve and imprint profile. The influence of the parameter w is studied in Section 4.6.3.

We point out that the level set method [96] can be generally used for indentation curve without special attention paying to different boundary conditions. The reason why we choose the current description rests with the formation of raw data (point-wise) collected during indentation test. Similarly, a typical imprint can also be characterized using level set function considering it as an open surface.

4.3.2 Reducing dimensionality of indentation snapshot by SVD

We begin with M numerical experiments defined by an appropriate DoE for the varying set of design parameters $\boldsymbol{\mu}^{(i)}$, $i = 1, 2 \cdots M$ representing the material parameters to be identified. Different indentation responses $\boldsymbol{s}^{(i)} = \boldsymbol{s}(\boldsymbol{\mu}^{(i)})$ extracted from FE simulation results are then considered as snapshots. In this section, the imprints are employed to present the method (Figure 4.6), and the general notation "$\boldsymbol{s}$" is employed without any distinction. The centered snapshot matrix $\boldsymbol{S}$ is given by

$$\boldsymbol{S} = [\boldsymbol{s}^{(1)} - \overline{\boldsymbol{s}}, \boldsymbol{s}^{(2)} - \overline{\boldsymbol{s}}, \cdots \boldsymbol{s}^{(M)} - \overline{\boldsymbol{s}}], \tag{4.6}$$

where $\overline{\boldsymbol{s}}$ is the mean snapshot

$$\overline{\boldsymbol{s}} = \frac{1}{M} \sum_{i=1}^{M} \boldsymbol{s}^{(i)}. \tag{4.7}$$

Singular value decomposition [61] of $\boldsymbol{S}$ yields

$$\boldsymbol{S} = \boldsymbol{\Phi} \boldsymbol{\Sigma} \mathbf{V}^{\mathrm{T}}, \tag{4.8}$$

where the diagonal matrix $\boldsymbol{\Sigma}$ contains the singular values σ_i, $i = 1, 2 \cdots M$; the left singular vectors $\boldsymbol{\Phi} = [\boldsymbol{\phi}^{(1)}, \boldsymbol{\phi}^{(2)} \cdots \boldsymbol{\phi}^{(M)}]$ are right the eigenvectors of the covariance matrix $\boldsymbol{C} = \boldsymbol{S}\boldsymbol{S}^{\mathrm{T}}$

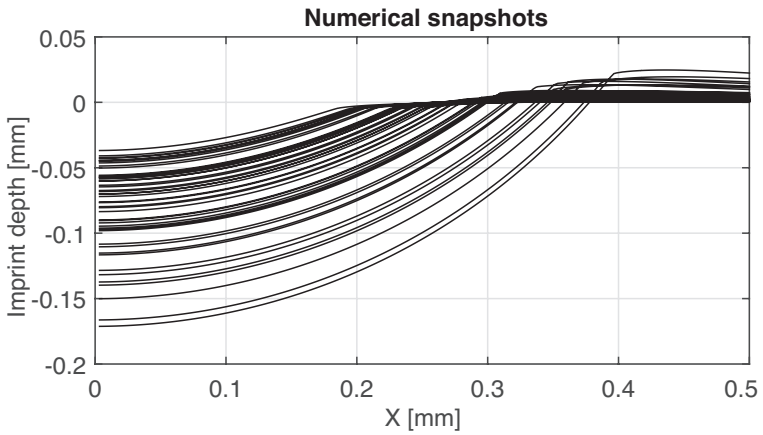

FIGURE 4.6 A series of snapshots obtained for varying material parameters.

and are also called POD modes. Figure 4.7 gives the mean of all imprint snapshots from Figure 4.6, as well as the modes scaled by the corresponding eigenvalues $\lambda_i = \sigma_i^2$. All the imprints are thus described in the reduced space

$$\alpha_j^{(i)} = \left(\boldsymbol{\phi}^{(j)}\right)^{\mathrm{T}} \left(\boldsymbol{s}^{(i)} - \bar{\boldsymbol{s}}\right), \; j = 1, 2 \cdots M. \tag{4.9}$$

In standard POD, one considers only $m \ll M$ significant modes corresponding to the largest eigenvalues of the covariance matrix using the following criterion

$$err = 1 - \frac{\sum_{i=1}^{m} \lambda_i}{\sum_{j=1}^{M} \lambda_j}. \tag{4.10}$$

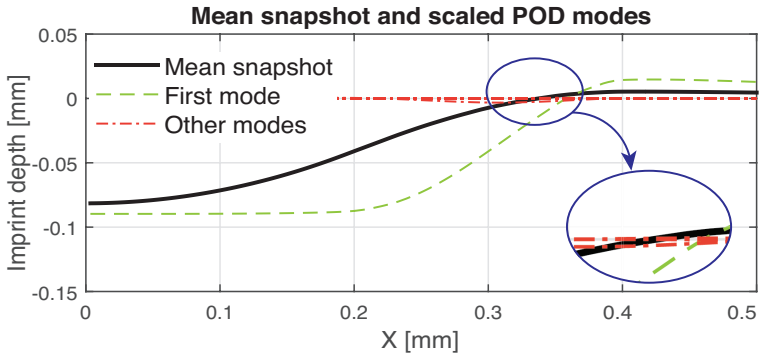

FIGURE 4.7 The mean snapshot and different POD modes scaled by the corresponding eigenvalues.

and by fixing a threshold for *err*. However, the difficulty lies in the choice of a proper value for *err*. Another option to truncate the basis is inspired by estimating the *intrinsic dimensionality*, where a telltale gap between eigenvalues can be observed. In this way, the high-dimensional imprints are finally described in a reduced space of m-dimensionality. Note that, in very rare cases, we will keep all the modes if the snapshots are already orthogonal. However, in most cases, the reduction of the number of modes is still possible, and the effect of adopting different numbers of modes will be analyzed in Appendix C.

4.4 Example shape manifold of indentation responses

To construct example manifolds considering different information, we perform a series of simulations over a design/parametric space where $n \in [0.2,\ 0.3]$ and $\sigma_y \in [200\,\text{MPa},\ 240\,\text{MPa}]$. The parameters are equal-spaced sampled from the design space to provide a graphical interpretation of manifold's dimensionality in the shape space. We are aware that these intervals chosen for the two parameters are narrow, yet they allow us to depict a small patch of the manifold which is sufficient to illustrate the manifold approach.

A series of databases, each containing $21 \times 21 = 441$ snapshots, are built up for indentation curves and imprint mappings or their combinations, with respect to different indenter shapes and simulation setups. The corresponding manifolds are constructed using the protocol detailed in Section 4.3.2. As mentioned, the manifolds are presented in 3D in spite that they evolve in $\mathbb{R}^M$ without mode truncation. For illustration purpose, only the first three coefficients are presented in subsequent figures although any other triplet of coefficients could also be used to demonstrate the inter-relationship between α-coefficients.

4.4.1 *P-h* curve manifolds

We first consider only the indentation curves ($w = 0$). For the loading and unloading phase, the same number of steps is chosen, i.e., $p = q = 201$, and the strategies presented in Figure 4.5 are employed to characterize each *P-h* curve with a vector of dimensionality 402×1. It is noticed that the size of the snapshot corresponds to the number of loading/unloading steps in experimental regime, while for simulation curves interpolation is always performed to be coincident with the experimental one. While the relative influence of loading and unloading parts could be studied separately, we still consider them as a whole, and a standard manifold construction process is then followed to transform each indentation curve to a single point in low-dimensional space. The results are shown in Figure 4.8 for different combinations of experimental setups and indenter geometries.

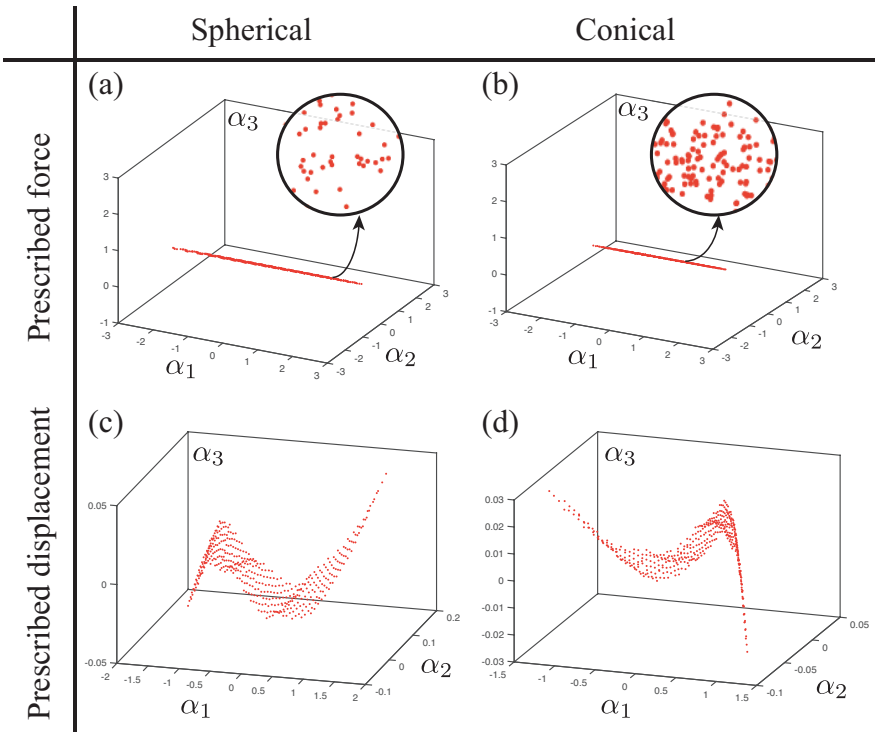

FIGURE 4.8 Manifolds based on indentation curve snapshots $\boldsymbol{s}_{\mathrm{C}}$, $p = q = 201, w = 0$.

It is observed that we obtain almost a single line if the indentation test is force-driven, regardless of the indenter geometries (Figure 4.8 (a) and (b)), yet 2D manifolds in Figure 4.8 (c) and (d) for prescribed displacement boundary condition. According to different conditionings illustrated in Figure 4.3, it appears therefore that, by modeling a displacement-driven indentation processes, we shall have more chance to obtain a unique identification solution. However, if we examine carefully different scales with which the manifolds in Figure 4.8 (c) and (d) are depicted, it is immediately noticeable that these two manifolds, in reality, are stretched along α_1 direction and present an extreme *"thin-and-long"* characteristic. With this consideration, the identification of both parameters remains difficult.

In this part, we observe with our reduced-order approach that the choice of prescribed boundary conditions in simulation may have an impact on the identifiability of the measured *P-h* curve, while the indenter geometries show less influence.

4.4.2 Imprint manifolds

Four different manifolds are also generated for the corresponding databases of residual imprint mappings following the same routine as for indentation curves. Each imprint is

characterized by the vertical displacements of 540 points sampled from one of the profile, and is mapped into $\alpha-$space, Figure 4.9.

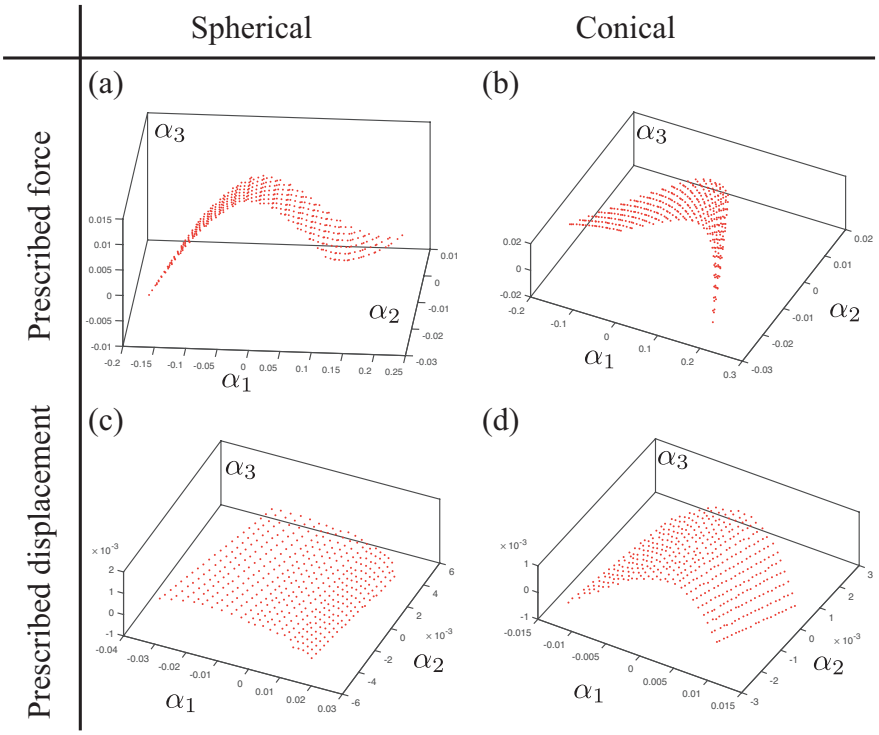

FIGURE 4.9 Manifolds based on imprint snapshots $\mathbf{s}_\mathrm{I}$, $l = 540, w = 1$.

Unlike *P-h* curve manifolds, these obtained from the imprint mappings indicate, all of them, a dimensionality of two. Thus the imprint is supposed to interpret more material properties than the indentation curve, and we postulate that we are able to identify two material parameters simultaneously. It is also suggested by the difference of curvature of the manifolds that the inverse problem is slightly better-conditioned when the simulation is a displacement-driven one. This will be further explored in Section 4.5.

Besides, we notice again that the same observation concerning the *thin-and-long* property also holds for imprint manifolds, especially when the maximum force is controlled in simulation. Therefore, scaling the manifold may help to distinguish the imprint shapes represented by points in $\alpha-$space. We expect this improvement will help us more accurately identify both parameters, or at least, accelerate the convergence. However, this scaling operation should be based on the knowledge of intrinsic dimensionality (we are not allowed to scale the first two α-coordinates if the intrinsic dimensionality of the manifold is one, otherwise a meaningless cloud of points is obtained). The influence of this scaling operation, though pointed out here, will be further studied in Section 5.3 along with identification procedures.

4.4.3 Manifolds combining *P*-*h* curve and imprint

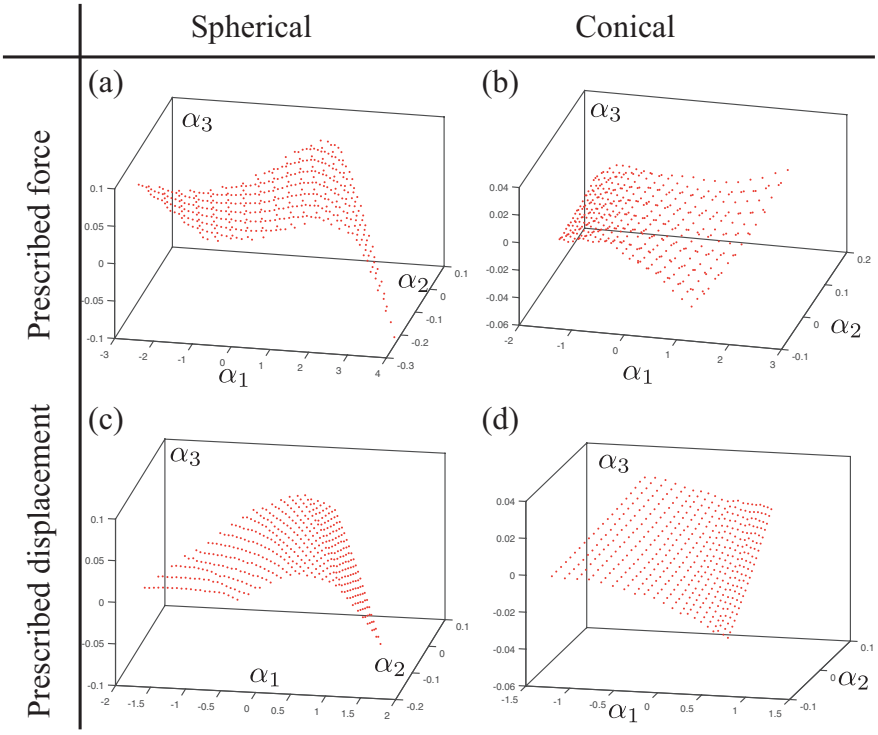

FIGURE 4.10 Manifolds based on combined snapshot $\boldsymbol{s} = [0.5\boldsymbol{s}_{\mathrm{I}},\ 0.5\boldsymbol{s}_{\mathrm{C}}]^{\mathrm{T}}$.

Now we will employ all available information, i.e., the *P*-*h* curve $\boldsymbol{s}_{\mathrm{C}}$ and the imprint mapping $\boldsymbol{s}_{\mathrm{I}}$. Both of them are normalized before concatenating. First, $w = 0.5$ is adopted to assign an equal-weighted contribution to the cost function defined by Equation 4.11.

The obtained manifolds are compared in Figure 4.10. Obviously, small difference is observed in comparison with the forms of manifolds drawn from imprints in Figure 4.9. Nevertheless, instead of a regular distribution of the snapshots, slight oscillations can be observed, especially in Figure 4.10 (a) and (b). On the other hand, when inspecting the respective scales on Figure 4.9 and 4.10, we observe that the ratio between the lengths of the two primary axes (α_1 and α_2) is around 15 in Figure 4.10 (d) while 5 in Figure 4.9 (d). This observation may be influenced by the choice of w thus is further studied in Section 4.6.3.

4.5 Solving the inverse identification problem in reduced space

In a typical inverse identification problem, the experimental shape $\boldsymbol{s}_{\mathrm{exp}}$ does not necessarily belong to the manifold due to two main sources of errors : the model error and the

measurement error. In this way, the solution to the inverse analysis is the set of parameter values $\boldsymbol{\mu}^*$ with which the simulated admissible shape $\boldsymbol{s}(\boldsymbol{\mu}^*)$ has the closest distance to the experimental measured quantities, or in other words, minimizing the cost/objective function in the reduced shape-space

$$\varepsilon = \|\boldsymbol{\alpha}_{\text{exp}} - \boldsymbol{\alpha}(\boldsymbol{\mu})\|, \tag{4.11}$$

in which $\boldsymbol{\alpha}_{\text{exp}}$ is the coordinate of experimental imprint $\boldsymbol{s}_{\text{exp}}$ in shape space, and is computed as follows

$$\boldsymbol{\alpha}_{\text{exp}} = \boldsymbol{\Phi}^{\text{T}}\Big(\boldsymbol{s}_{\text{exp}} - \bar{\boldsymbol{s}}\Big). \tag{4.12}$$

In the present section, we focus only on the manifolds for a *spherical* indenter. In place of performing inverse identification, the objective function is computed over a large design space, with respect to a pseudo-target $\boldsymbol{s}_{\text{exp}}$ simulated by using $\sigma_y = 216$ MPa and $n = 0.255$. By ruling out possible model and measurement errors, we expect to observe a unique minimum from the distribution of the objective function.

4.5.1 Objective function based on *P-h* curve

The distribution of the objective function in Equation 4.11 for $w = 0$ is presented in Figure 4.11. It is not surprising that no unique solution can be found when we employ only the *P-h* curve while using a prescribed force since the intrinsic dimensionality of the corresponding manifold is one, Figure 4.8 (a). This is also consistent with the observation in [104], where the error is computed as conventional point-wise discrepancy between measured and simulated quantities.

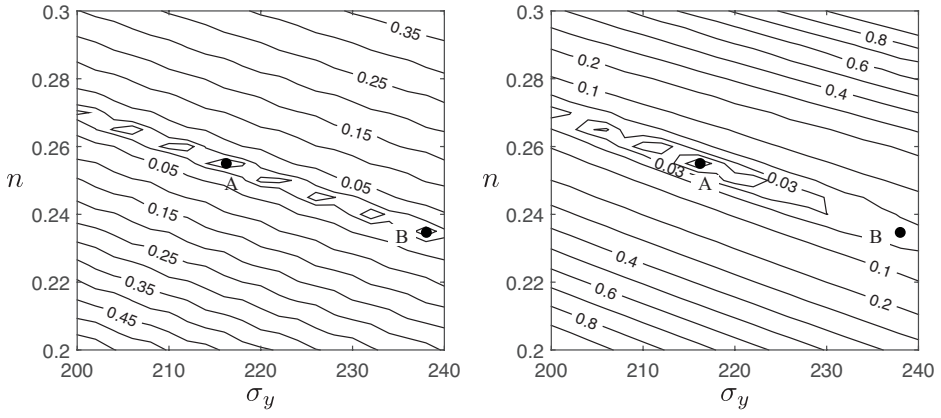

(a) Prescribed force (b) Prescribed displacement

FIGURE 4.11 Objective function distribution when employing *P-h* curve snapshots with spherical indenter, $p = q = 201$, $w = 0$.

Besides, we note again that different boundary conditions in simulation may lead to slight difference in the identifiability of material parameters with *P-h* curve. In Figure 4.11 (b), the solution to inverse problem is still not unique despite that the number of local minima is decreased. We consider thus, by controlling the displacement during inverse analysis, the inverse problem should be slightly better posed. Here, by "better conditioned", we mean that the parameters can be identified more easily, rather than that more parameters can be identified.

4.5.2 Objective function based on imprints

Then, the residual imprint is considered and the error distributions computed from imprint manifolds (Figure 4.9 (a) and (c)) are presented in Figure 4.12. Unlike in Figure 4.11 (a), even if the parameter sets (σ_y, n) that give almost the same minimal error lie in a *"thin-long valley"*, we are still able to extract the exact constitutive parameters $\boldsymbol{\mu}^*$ without being caught by local minimum. The contour lines of the error distribution show a single global minimum which allows the accurate identification of *both* material properties. These results show a clear advantage of imprint in the identification procedure in comparison with indentation *P-h* curve. On the other hand, we observe again that the situation is improved when switching the boundary condition in simulation from prescribed force to displacement, and the improvement is significant for imprint manifolds. The possible reasons behind this phenomenon are discussed in Section 4.6.2.

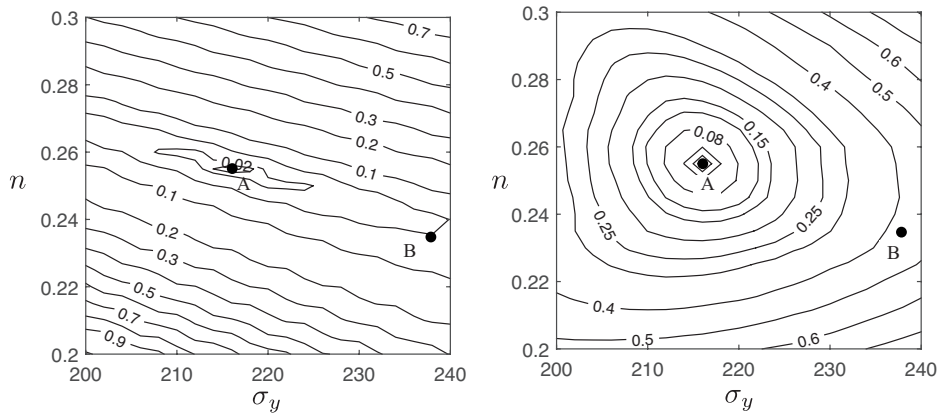

(a) Prescribed force (b) Prescribed displacement

FIGURE 4.12 Objective function distribution when employing imprint snapshots with spherical indenter, $l = 540,\ w = 1$.

4.5.3 Objective function based on *P-h* curve and imprint

Finally, we consider the snapshots which combine the *P-h* curves and the residual imprints in Figure 4.13. Once again, the contour lines demonstrate the possibility of identifying two parameters simultaneously. A slightly better conditioning may be observed for Figure 4.13 (a) against Figure 4.12 (a) since more information is provided for identification. However, when comparing Figure 4.12 (b) and Figure 4.13 (b), this influence seems to depend on the choice of the value of *w*. Thereby, it can be concluded from the manifolds as well as the corresponding error distributions that more information does not necessarily result in a better-conditioned inverse problem, and a compromise needs to be found on both indentation quantities.

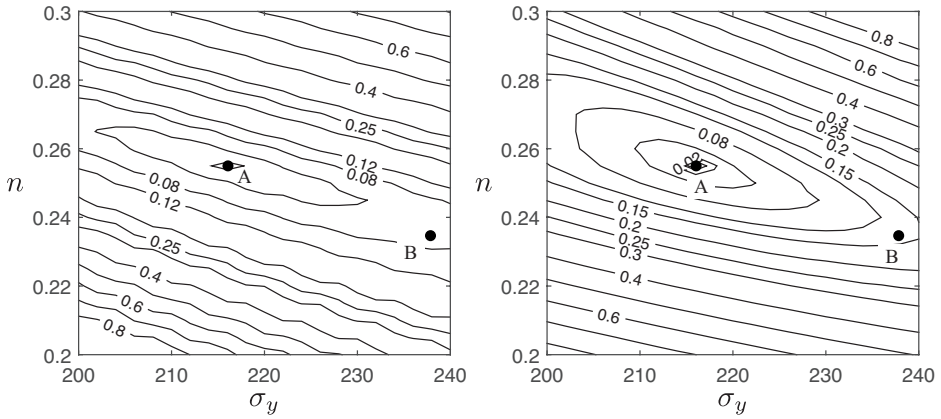

(a) Prescribed force (b) Prescribed displacement

FIGURE 4.13 Objective function distribution when employing the combined snapshots with spherical indenter, $p = q = 201, l = 540, w = 0.5$.

4.6 On the identifiablity of different parameters

In this section, the condition number is adopted to compare the quality of the global and one of the local minima, i.e., point A and B in Figure 4.11-4.13. The influence of BCs and the choice of weighting coefficient *w* in combining *P-h* curve and imprint are also investigated in detail.

4.6.1 Sensitivity analysis

To enhance the understanding of identifiability of different material parameters, especially when different simulation boundary conditions are employed, the sensitivity analysis is

performed to quantify the influence of different parameters on the optimization criterion (Equation 4.11). For consistency, the identification error was calculated with respect to a pseudo-target $\boldsymbol{s}_{\text{exp}}$ simulated by using $\sigma_y = 216$ MPa and $n = 0.255$, allowing us to reuse the error distributions calculated in Figure 4.11- 4.13. The two components of the gradient $\nabla(\varepsilon) = (\partial\varepsilon/\partial\sigma_y, \partial\varepsilon/\partial n)$ are computed as :

$$\begin{cases} \dfrac{\partial \varepsilon(\boldsymbol{\mu})}{\partial \sigma_y} = \dfrac{\Delta\varepsilon}{\Delta\sigma_y}(\sigma_y^{\max} - \sigma_y^{\min}) \\ \dfrac{\partial \varepsilon(\boldsymbol{\mu})}{\partial n} = \dfrac{\Delta\varepsilon}{\Delta n}(n^{\max} - n^{\min}) \end{cases} . \tag{4.13}$$

Here, the derivatives of the two parameters are approximated by a first-order forward finite difference scheme. To avoid extra simulations, a step length of $\Delta\sigma_y = 2$ MPa and $\Delta n = 0.005$ are chosen in view that they are right the step length of the sampling grids in design space. Superscripts "max" and "min" are employed for the upper and lower boundaries of the two parameters in the purpose of rendering the two derivatives dimensionless. We notice that, despite using the finite difference method, these sensitivities may be computed analytically with an approximated polynomial expression of global manifold [20].

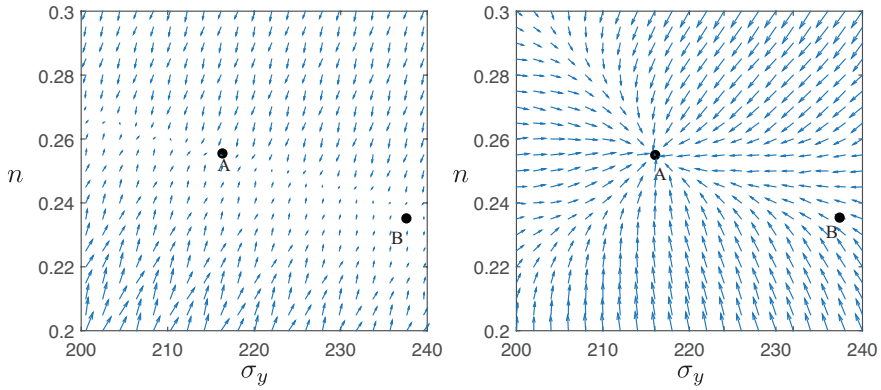

(a) Prescribed force (b) Prescribed displacement

FIGURE 4.14 Maps of $-\nabla(\varepsilon)$ obtained from imprint manifolds in Figure 4.12 : (a) prescribed force and (b) prescribed displacement.

Taking the graphs of cost functions for imprint manifolds (Figure 4.12) as an example, the possible optimization trajectories are depicted by $-\nabla(\varepsilon)$ for different simulation boundary conditions in Figure 4.14. By design, the arrows point in the direction of the greatest rate of decrease of the cost function. Therefore, as observed, the minimization problem converges easily to point A regardless of the staring point in Figure 4.14 (b), while it is not the case of Figure 4.14 (a).

4.6.2 Conditioning number

Thus, to examine the quality of the optimal solution, the Hessian matrix, containing the second-order partial derivatives of the cost function is computed by forward finite difference

$$\boldsymbol{H} = \begin{bmatrix} \dfrac{\partial^2 \varepsilon}{\partial \sigma_y^2} & \dfrac{\partial^2 \varepsilon}{\partial \sigma_y \partial n} \\ \dfrac{\partial^2 \varepsilon}{\partial n \partial \sigma_y} & \dfrac{\partial^2 \varepsilon}{\partial n^2} \end{bmatrix} \tag{4.14}$$

for point A : (216 MPa, 0.255), where a global minimum should be found. By convention, the condition number of the inverse problem $\kappa(\boldsymbol{H})$ is defined as the ratio of the biggest to the smallest singular values of the Hessian. It is a property of the problem and with a low condition number a problem is said to be well-conditioned, while ill-conditioned for a high condition number. All eigenvalues have to be positive for a minimum. We find that the prescribed displacement boundary condition renders a better-conditioned inverse problem by showing a condition number of 1.326 (Figure 4.12(b)), while $\kappa = 6.1617$ if the maximal force is controlled (Figure 4.12(a)).

The above explains, from a mathematical point of view, why the inverse problem is better conditioned when we perform the simulation with a prescribed maximal displacement. From physical standpoint, we deem that, by the end of the loading phase, the imprint shapes obtained with the same prescribed force are quite different for diverse material properties, while this difference should be much smaller when maximal displacement is prescribed. As a consequence, the unloading phase shall start with almost the same geometric imprint configuration, but deforms differently from material to material due to different stress fields at maximal penetration depth, allowing for easier differentiation between materials. For the case of prescribed force, the residual imprint depends on both the loading and unloading phases. The possibility of interference between the two phases may lead to less sensitive indentation responses in the scope of our protocol.

4.6.3 The choice of weighting coefficient w

On the other hand, the conditioning numbers with respect to cost functions in Figure 4.13 ($w = 0.5$) are also calculated for solution point A, giving the value of 3.5269 and 3.5231 for (a) and (b), respectively. This result is in line with the conclusion drawn at the end of Section 4.5 that more information employed for identification can, but not always, lead to a better-conditioned problem. For this reason, we further study the influence of weighting coefficient w. Results are given in Figure 4.15. The conditioning of inverse problem is improved and is

approximately constant for $0.6 \leq w \leq 1$. We also notice that, increasing the weight of the indentation curve by reducing w decreases the quality of the optimum.

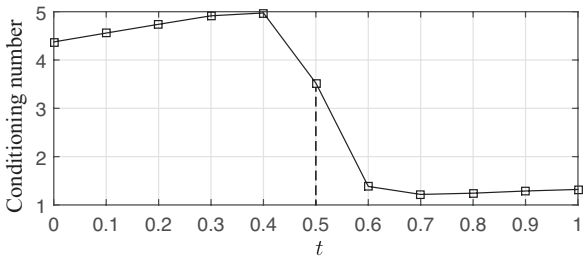

FIGURE 4.15 The conditioning of the inverse problem for different values of weighting coefficient w in Equation. 4.5 (prescribed displacement).

4.7 Unique identification of Hollomon's law with only a conical indenter

In the previous sections, we have observed from the manifolds that the power law parameters can be identified using solely the residual imprint, and the well known non-unicity issue presented in Section 2.3.3 appears to be alleviated, at least for spherical indentation (Section 4.5 - 4.6). In this section, we attempt to confirm the validity of this observation for self-similar *conical* indenters by observing distinguishable imprints for mystical material pairs.

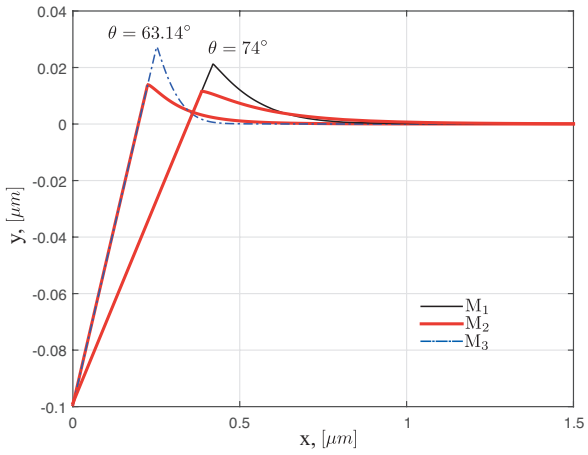

FIGURE 4.16 Distinguishable residual imprints for the two mystical material pairs using conical indenters.

Besides the mystical pair presented in Section 2.3.3, another pair with regard to $\theta = 63.14°$ is also considered. Figure 4.16 shows the residual imprints of the two mystical material

pairs, $(M_1, M_2)_{\theta=74^\circ}$ and $(M_2, M_3)_{\theta=63.14^\circ}$, after unloading at a maximum penetration depth $h_{\max} = 0.1$ mm. Similar to the case of spherical indentation, clear differences are, as expected, observed around the pile-up zones, and both material pairs are no longer "mystical" when we consider the residual imprint profiles.

We speculate therefore that the imprint mapping may possibly contain more "complete" information of the material's plastic behavior, thus rendering the inverse problem "better-posed", at least for the current case (as far as isotropic elastoplastic materials with isotropic hardening and rate-independent J2 plasticity are concerned). However, we must still be cautious to rule out the existence of mystical materials for the imprint-based inverse problem. In other words, we need to answer the question of *whether or not there exist different materials that reveal indistinguishable residual imprints*.

For this purpose, we will compare a series of imprints in the low-dimensional space constructed by using the approach presented in Section 4.3.2. FE simulations (assuming *conical* indentation with $\theta = 74^\circ$) are performed on 11×11 instances from a factorial DoE with material intervals : $n \in [0.2, 0.3]$ and $\sigma_y \in [200\text{ MPa},\ 240\text{ MPa}]$. According to Equation 4.6-4.9, every imprint corresponds to a single point in the shape space. Since the intrinsic dimensionality of the shape space can not *exceed* the number of material parameters being manipulated in the DoE ($d = 2$ for Hollomon's hardening materials), the indentation responses may be readily visualized in a 3D Cartesian coordinate system (Figure 4.17).

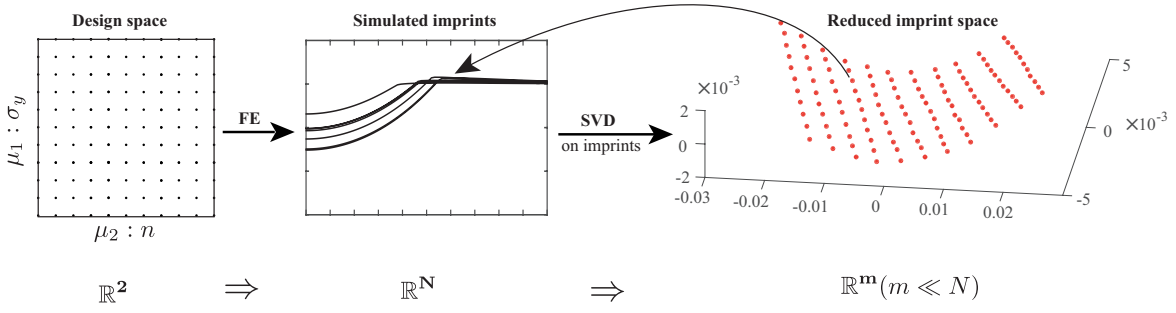

FIGURE 4.17 Correspondence between the Design of Experiments and residual imprint mappings in "shape space".

We observe that all imprints, reduced to single points, are clearly separated and show a regular distribution (without overlapping or intersection). This clearly demonstrates a one-to-one correspondence between the material parameters and the residual imprint mappings, and further suggests the absence of two different material parameter sets that may lead to the same (conical) imprint profile upon indenter withdrawal. For this reason, we may consider the inverse identification problem based on the indentation imprint as well-posed.

4.8 Closing remarks

In this chapter, a uniform pattern is developed for the characterization of diverse indentation responses, i.e., the *P-h* curve and the imprint shapes. In addition, the identification problem is transformed to a reduced shape-space by using dimensionality reduction algorithms. Based on a series of databases built for imprint mappings and indentation curves, the identifiability of two Hollomon's parameters from an indentation test is studied using the shape-manifold approach.

This chapter highlights the use of the manifold approach to estimate the maximum number of independent material parameters that may be determined from an indentation model. The computational findings through manifold and sensitivity analysis reveal that more parameters can be identified when we consider the *residual mapping* of the specimen after indentation, *regardless* of the indenter geometry or the experimental setup. However, there are still fewer situations, e.g., employing the *P-h* curve with prescribed force boundary condition, from which inaccurate identification results may be obtained.

On the other hand, the manifolds provide us with insight into different levels of difficulty in material characterization when diverse boundary conditions are employed in simulation. It is suggested to control the maximum penetration/displacement in simulations with the aim of identifying material parameters more easily. However, we need to be aware that the number of identifiable parameters still depends upon the experimental information at hand.

While proposed in the scope of instrumented indentation, the same approach is obviously applicable to other methods of mechanical testing. In the next chapter, the insights gleaned from Hollomon's parameter identification using the global manifolds will be further validated using local manifold approaches, and we will also attempt to generalize these conclusions to the Voce hardening parameter identification.

Chapitre 5

Material characterization based on local manifolds

We have so far applied the manifold protocol to simulated indentation responses in Chapter 4, and a series of *global* manifolds were studied to investigate the identifiability of Hollomon's power law parameters. Some insights have also been gained on the influence of simulation boundary conditions and the adopted indentation responses on the uniqueness of the solutions to the identification problem. The computational findings based on both manifolds and sensitivity analysis illustrated that the residual imprint may allow for an easier and unique identification of Hollomon's parameters, even for conical indenters, for which the non-uniqueness issue has been extensively reported by different authors in the literature.

In the current chapter, these conclusions will be further verified by iterative identification procedures, where the manifold will be constructed in piece-wise fashion at moderate computational expense, with the help of local-manifold learning algorithms. We note on the other hand that the insights gained in Chapter 4 are based on the hypothesis that the material in study hardens according to the Hollomon's power law. It is therefore natural to expect that all these conclusions may be generalized to other similar material laws which may involve more parameters. In this regard, this chapter is partly devoted also to the characterization of the three-parameter Voce law.

In the following, the inverse identification problem is defined in Section 5.1 within the framework of local manifolds. Several manifold learning approaches are then developed in Section 5.2 to explore the design space either by exploration or intensification. The unique identification of Hollomon's parameters is verified using local-manifolds in Section 5.3, while a failure with respect to that of the Voce law is presented in Section 5.4. Closing remarks are finally given in Section 5.5

5.1 Inverse identification problem based on local manifolds

To further illustrate the advantage of residual imprint over *P-h* curve in identification, we propose in this section an *on-line* approach that constructs only the *useful* portion of $\mathscr{M}$. For this purpose, the inverse problem is generally solved in iterative fashion. The "pseudo-time" of the identification, i.e., the iteration step number, is indexed by t.

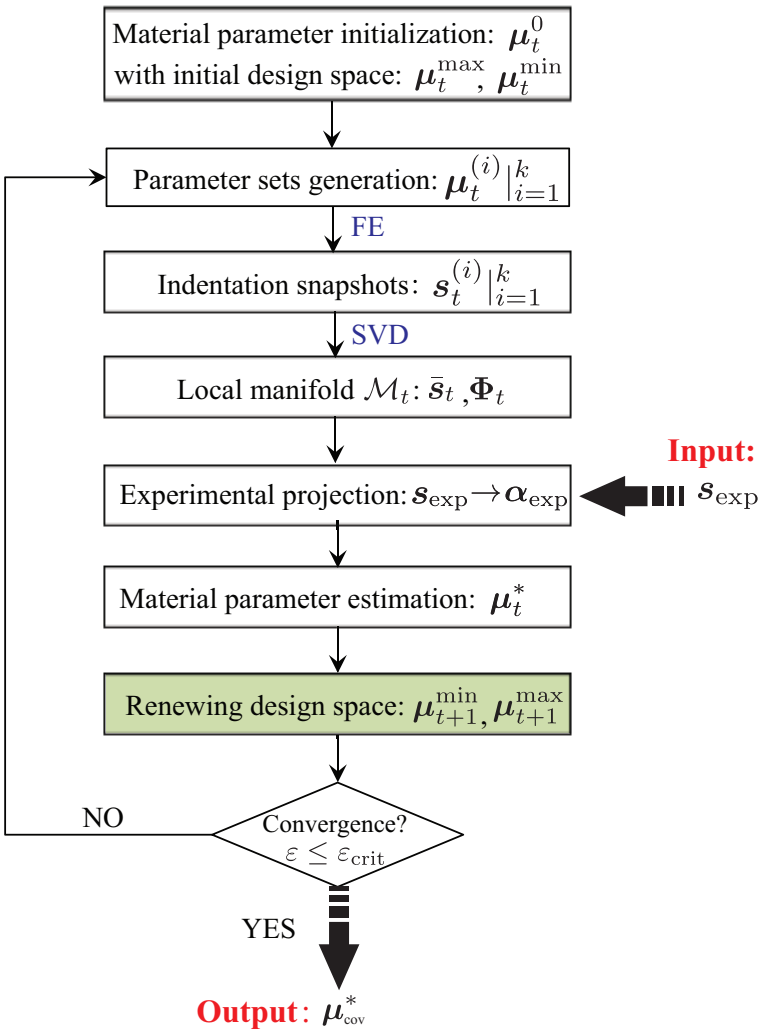

FIGURE 5.1 Framework of material characterization using local manifold approach.

Within each iteration step t, instead of simulating a considerable number of M imprints like in Section 4.3.2, only a few k snapshots are sampled around $\boldsymbol{\mu}_t^0$ (the current estimate of material parameters) in the *local* searching domain. A portion of the global manifold $\mathscr{M}_t$ will then be constructed from these snapshots, and we achieve an intermediate estimate $\boldsymbol{\mu}_t^*$ by virtue of the one-to-one correspondence between material set and points on manifold. This

new estimate will then be chosen as the center of the vicinity to be exploited, i.e., $\boldsymbol{\mu}_{t+1}^0 = \boldsymbol{\mu}_t^*$. The above procedure are repeated until convergence is achieved for material parameters.

According to the fundamental hypothesis of imprint manifold, even assuming that the indented material behaves exactly according to the postulated material law, the projection of experimental imprint will not lie on the manifold $\mathscr{M}$. The offset of $\boldsymbol{\alpha}_{\text{exp}}$ from the imprint-manifold takes roots in the measurement noise. Consequently, we propose performing the identification in shape space by finding, in each iteration step t, the closest point $\boldsymbol{\alpha}_t^*$ on $\mathscr{M}_t$ such that

$$\boldsymbol{\mu}_t^* = \arg\min_{\boldsymbol{\mu}} dist(\boldsymbol{\alpha}_{\text{exp}},\ \boldsymbol{\alpha}(\boldsymbol{\mu})),\ \alpha(\boldsymbol{\mu}_t^*) \in \mathscr{M}_t, \tag{5.1}$$

where $dist(\boldsymbol{\alpha}_{\text{exp}},\ \boldsymbol{\alpha}(\boldsymbol{\mu}))$ is the distance between the simulated $\boldsymbol{s}(\boldsymbol{\mu})$ and experimental imprint $\boldsymbol{s}_{\text{exp}}$ shapes in α-space. Therefore, the identification of material properties can be carried out in at most an k-dimensional space. We recall that $k \ll N$, where N is the dimensionality of the imprint shape vector $\boldsymbol{s}$ used in Equation 4.6, and k is the number of neighborhoods to construct each local-manifold.

Finally, we summarize the above mentioned steps in the flowchart in Figure 5.1. We note that both the construction and approximation of local manifold are similar to the corresponding steps for the global manifold as presented in Section 3.3.2 and 3.3.4, respectively. The only difference is the use of less (k in stead of M) snapshots and lower-order polynomials. However, different strategies may be adopted to define the local searching space in each iteration step, evoking different local manifold algorithms which will be presented in detail in the next section.

5.2 Local manifold learning algorithm families

In local-manifold learning, each local-manifold is constructed only using a part of the whole design space, which is then explored based on the predictor-corrector strategy issued from [81, 122]. In this section, we informally propose two manners of iteration : exploration and intensification. The former corresponds to relocating iteratively the local-manifold of interest (the neighboring manifold within which the experimental projection is projected), while the latter attempts to gradually improve the accuracy of local-manifold for accurate identification.

For illustration purposes, we adopt a global two-parameter-design space and a local design window, with the width and height referring to the range of variation of the two parameters at the current iteration step.

5.2.1 *panning*

In this algorithm, the design window pans in the whole design space while the window size remains unchanged (Figure 5.2). For the sake of clarity, only the snapshot located at the center of each DoE is depicted. For the first iteration step, we calculate a prediction with the points sampled within the initial design window. If the new prediction lies outside of this window, we limit it to the window boundary and the next iteration window will be centered around this new prediction. We repeat this process until the predicted point is positioned almost in the *center* of the current window and no evolution of the searching domain is observed. This strategy can be realized by using the following pseudo code, Algorithm 1.

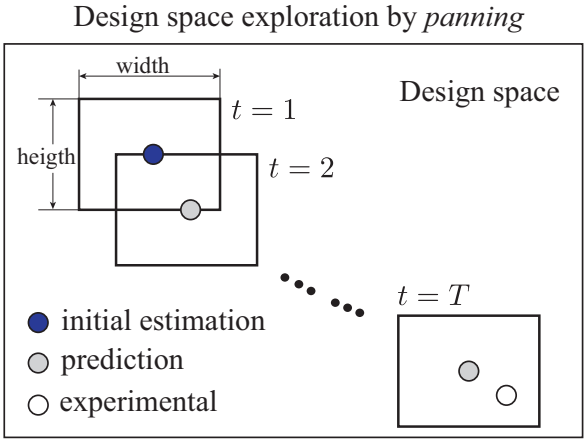

FIGURE 5.2 *Panning* iterations.

5.2.2 *zooming*

In this algorithm, the first DoE covers the entire (rather large) design space, after which the window size is cut down with each subsequent iteration, as shown in Figure 5.3. Unlike in *panning* algorithm, the new design window may not be centered around the estimate. Rather, we compute an intermediate estimate to locate the subsequent searching domain with the greatest possibility of capturing the properties of the experimental imprint. The new design window is always reduced by half along each direction. Notice that, except renewing the design space to be explored (green block), other procedures in the flowchart Figure 5.1 should not be perturbed by either exploration manner. This process is repeated until the convergence criterion in Equation 5.1 is satisfied.

Algorithm 1 : panning

Initial parameter set : $\boldsymbol{\mu}_{t=1}^{0}$;
% Define local-space to be explored
Fixed (small) window size : $\Delta\boldsymbol{\mu}$;
$\boldsymbol{\mu}_t^{\max} = \boldsymbol{\mu}_t^0 + \Delta\boldsymbol{\mu}$;
$\boldsymbol{\mu}_t^{\min} = \boldsymbol{\mu}_t^0 - \Delta\boldsymbol{\mu}$;
while TRUE **do**
    Design of experiments by LHS : $\boldsymbol{\mu}_t^{(1)}, \boldsymbol{\mu}_t^{(2)}, \cdots, \boldsymbol{\mu}_t^{(k)}$;
    Indentation response simulation : $\boldsymbol{s}_t^{(1)}, \boldsymbol{s}_t^{(2)}, \cdots, \boldsymbol{s}_t^{(k)}$;
    Local-manifold space construction : $\bar{\boldsymbol{s}}_t$ and $\boldsymbol{\Phi}_t$;
    Experimental indentation measurement projection : $\boldsymbol{s}_{\text{exp}} \rightarrow \boldsymbol{\alpha}_{\text{exp}}$;
    Material parameters estimation : $\boldsymbol{\mu}_t^*$;
    % Checking convergence
    if $\text{dist}(\boldsymbol{\mu}_{t+1}^*, \boldsymbol{\mu}_t^*) < \varepsilon_{\text{crit}}$ **then**
        EXIT LOOP ;
    else
    end if
    Update material parameters : $\boldsymbol{\mu}_{t+1}^0 = \boldsymbol{\mu}_t^*$; $t = t+1$;
    $\boldsymbol{\mu}_t^{\max} = \boldsymbol{\mu}_t^0 + \Delta\boldsymbol{\mu}$;
    $\boldsymbol{\mu}_t^{\min} = \boldsymbol{\mu}_t^0 - \Delta\boldsymbol{\mu}$;
end while

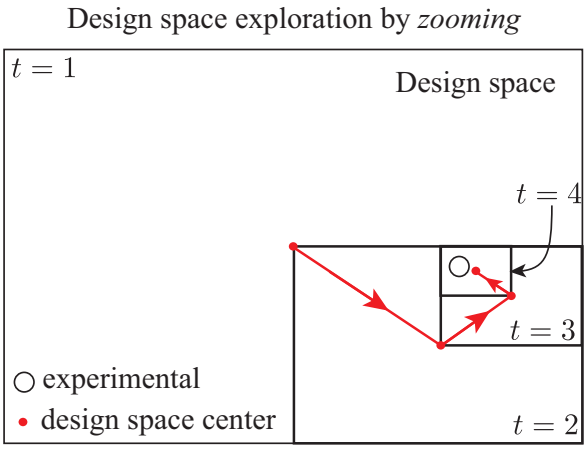

FIGURE 5.3 *Zooming* iterations.

5.2.3 *panning & zooming*

The *panning & zooming* method essentially combines both of the previous approaches. As illustrated in Figure 5.4, the general idea behind this algorithm is the use of a panning

Algorithm 2 : zooming

Initial parameter set : $\boldsymbol{\mu}_{t=1}^{0}$;
Initial design space to be explored : $[\boldsymbol{\mu}_t^{\min}, \boldsymbol{\mu}_t^{\max}]$;
while TRUE **do**
    Line 7-17 in Algortihm 1 ;
    if $\boldsymbol{\mu}_t^* < 0.5(\boldsymbol{\mu}_t^{\max} + \boldsymbol{\mu}_t^{\min})$ **then**
        $\boldsymbol{\mu}_{t+1}^{\max} = 0.5(\boldsymbol{\mu}_t^{\max} + \boldsymbol{\mu}_t^{\min})$;
    else
        $\boldsymbol{\mu}_{t+1}^{\min} = 0.5(\boldsymbol{\mu}_t^{\max} + \boldsymbol{\mu}_t^{\min})$;
    end if
end while

search at the beginning until the estimate for the next iteration lies inside the current design space instead of on the boundary, after which the search scheme will be switched to *zooming* in order to improve the accuracy of the local manifold.

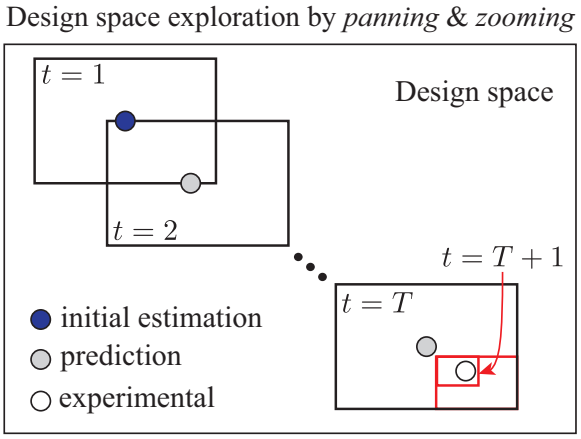

FIGURE 5.4 Combination of *panning* and *zooming*.

5.2.4 *Floating search*

We aware that the three above-mentioned algorithm should be chosen in considering the existence of different priori information regarding the material properties. For instance, it is suggested to employ the panning method to explore in a rather big space without (or with less) priori knowledge of material properties, while the zooming method is suitable if we have located a moderate space for given materials. The combined *panning* & *zooming*, almost not restricted by the pre-knowledge, has a limitation of complex programming. Besides, in rare cases, we may risk missing the optimal solution since the search zone is explored using a dichotomizing strategy.

Algorithm 3 : panning & zooming

1: Initial parameter set : $\boldsymbol{\mu}_{t=1}^{0}$;
2: % Define local-space to be explored
3: Fixed (moderate) window size : $\Delta\boldsymbol{\mu}$;
4: $\boldsymbol{\mu}_{t}^{\max} = \boldsymbol{\mu}_{t}^{0} + \Delta\boldsymbol{\mu}$;
5: $\boldsymbol{\mu}_{t}^{\min} = \boldsymbol{\mu}_{t}^{0} - \Delta\boldsymbol{\mu}$;
6: Initial design space to be explored : $[\boldsymbol{\mu}_{t}^{\min}, \boldsymbol{\mu}_{t}^{\max}]$;
7: **while** TRUE **do**
8: Line 7-17 in Algortihm 1 ;
9: **if** $\boldsymbol{\mu}_{t+1}^{0}$ on the boundary of design space **then**
10: panning strategy (Line 18-19 in Algorithm 1) ;
11: **else**
12: zooming strategy (Line 5-9 in Algorithm 2) ;
13: **end if**
14: **end while**

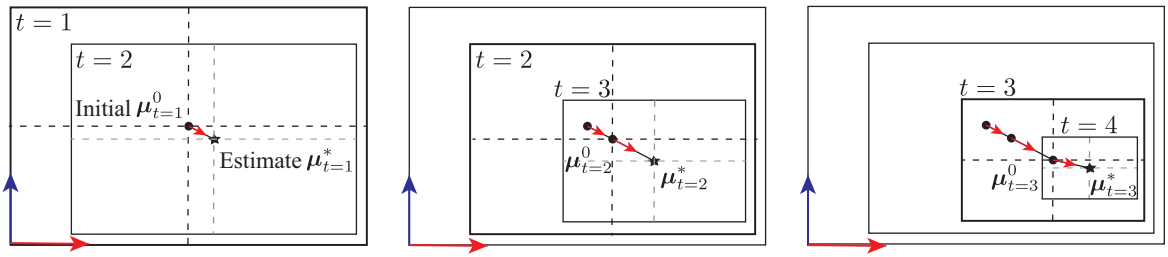

FIGURE 5.5 Floating search strategy.

Algorithm 4 : Floating search

Initial parameter set : $\boldsymbol{\mu}_{t=1}^{0}$;
Initial window size : $\Delta\boldsymbol{\mu}_{t=1}$;
while TRUE **do**
$\boldsymbol{\mu}_{t}^{\max} = \boldsymbol{\mu}_{t}^{0} + \Delta\boldsymbol{\mu}_{t}$;
$\boldsymbol{\mu}_{t}^{\min} = \boldsymbol{\mu}_{t}^{0} - \Delta\boldsymbol{\mu}_{t}$;
Line 7-17 in Algortihm 1 ;
%Update parameters with shrinking coefficient
$\boldsymbol{\mu}_{t+1}^{0} = \boldsymbol{\mu}_{t}^{*}$; $t = t + 1$;
$\Delta\boldsymbol{\mu}_{t+1} = \Delta\boldsymbol{\mu}_{t} * \beta$;
end while

Therefore, we additionally propose a *modified zooming* method, with which the already-searched space could be searched *again* in order to make up for possible bad-estimation from the previous step. In this algorithm, first of all, we use a user-defined multiplier β, namely the

"shrinking ratio" of design space after iteration, that is designed to control the convergence of the identification procedure. Secondly, and more importantly, each searching window needs to be centered on $\boldsymbol{\mu}_t^0$, which is also the estimate from last iteration $\boldsymbol{\mu}_{t-1}^*$, making it possible to cover a portion of the design space that has already been searched. We have named this algorithm a *"Floating search"*, and the search pattern is shown in Figure 5.5. Quite obviously in the figure, $\boldsymbol{\mu}_t^*$ is equal to $\boldsymbol{\mu}_{t+1}^0$. The floating search strategy is presented in the following pseudo code, Algorithms 4.

5.3 Inverse identification of Hollomon's parameters

Further validation examples involve the identification of material parameters employing either the indentation curve or the imprint mapping. Two representative cases are studied for brevity, and the advantage of imprint over indentation curve is underlined again by presenting diverse identification results. The two cases involve the use of :

i. Spherical indenter & prescribed force & *P-h* curve ;

ii. Conical indenter & prescribed displacement & imprint ;

Besides, according to the discussion in Section 4.4.2, we propose to scale the manifold coordinates according to its intrinsic dimensionality, providing us with a third case :

iii. Scaled manifold by conical indenter & prescribed displacement & imprint.

For the simulated experiment, the *P-h* curve and the imprint are obtained for elastic limit $\sigma_y^* = 200$MPa and isotropic hardening coefficient $n^* = 0.275$. The FE model presented in Section 4.1 is employed for simulations. We intend to retrieve the two "missing" constitutive parameters by considering different snapshot setups. For simplicity sake, only the floating search algorithm is used, while others will be verified with experimental data in later chapters. The same initial parameter set $(180, 0.2)$ and identical shrinking coefficient $\beta = 0.8$ are used to compare the influence of different measured quantities on identification. The final identified parameters summarized in Table 5.1 are compared with their target values.

TABLE 5.1 A comparison of identified material parameters using different measured quantities.

Case	σ_y	σ_y^*	Relative error	n	n^*	Relative error
(i)	194.33		2.84%	0.2808		2.1%
(ii)	199.90	200	0.05%	0.2750	0.275	0.01%
(iii)	200.00		0.00%	0.2746		0.15%

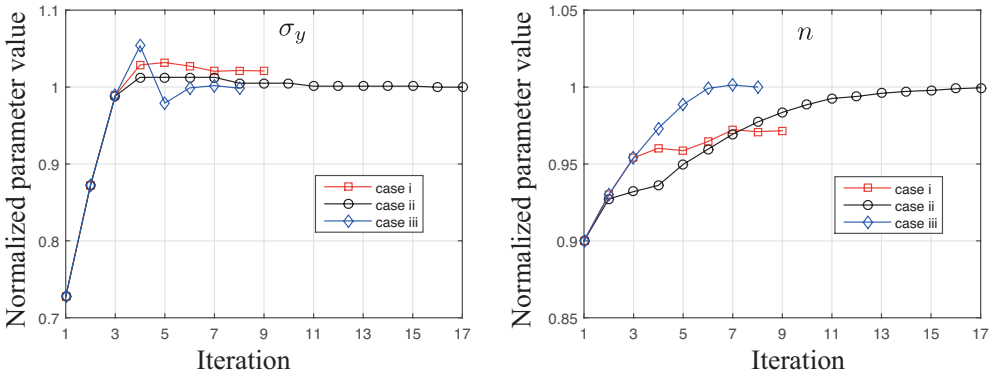

FIGURE 5.6 Convergence of σ_y(left) and n (right).

For case (i), based on our previous knowledge, the two parameters can not be estimated simultaneously since the identifiability of the *P-h* curve is poorer, demonstrated by the one dimensional manifold. Even if the parameters converged to the "final" values with less than 3% error, this identification result is still unacceptable in the absence of model and measurement errors. More importantly, we have also verified that this identification result turns out to be a local minimum of the error distribution in Figure 4.11 (a).

On the other hand, it is quite obvious that the two parameters are almost exactly retrieved for the cases (ii) and (iii), where the imprint mapping is employed. The identification result shows a maximum error of 0.05% for σ_y and 0.15% for n, highlighting once again the advantage of employing imprint mapping.

The convergence patterns for the two parameters are given in Figure 5.6. We note that the scaled manifold does not perturb the convergence, instead, the identification converges with only 9 iterations compared with 17 for the non-scaled manifold. This is simply due to the reason that the scaled manifold equilibrates the two sensitivity indices computed in Section 4.6.1. Finally, the approximations of numerical quantities to the experimental target

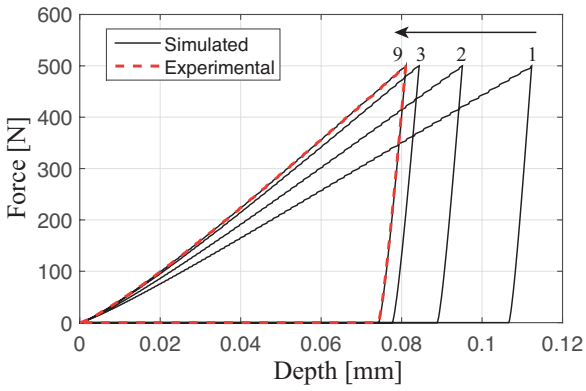

FIGURE 5.7 Convergence of the indentation curves (case i, iterations 1,2,3,9).

are presented in Figure 5.7 and 5.8. Good convergence is found for both the indentation curve and the residual imprint profile, thus validating the manifold-based identification protocol.

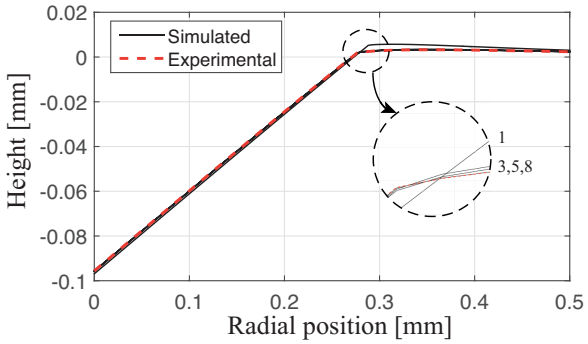

FIGURE 5.8 Convergence of the imprint mappings (case iii, iterations 1,3,5,8).

5.4 Inverse identification of Voce parameters

We have so far demonstrated that, by employing local manifold methods, we are capable of uniquely identifying the Hollomon's power law parameters from the residual imprint, regardless of the indenter geometry. In the current section, we intend to verify the validity of this conclusion on Voce law. The choice of this law is primarily based on the observation that many important engineering materials deviate significantly from the Hollomon's behavior [73, 163, 139], and the Voce law presenting a saturation stress is likely suitable for this family of alloys.

5.4.1 Identifying Voce parameters

Analogously, a numerical imprint is employed as the target shape, and this synthetic response is simulated following the protocol introduced in Section 4.1.1 with a maximal penetration depth $h_{\max} = 0.1$ mm, and using : $\boldsymbol{\mu}^{\text{Targ}} : (\sigma_y^*,\, Q^*,\, \gamma^*) = (300\,\text{MPa}, 200\,\text{MPa}, 14)$. By using the floating search algorithm along with $\beta = 0.8$, we attempt to identify the three constitutive parameters.

An arbitrarily chosen combination of constitutive parameters $\boldsymbol{\mu}_A : (430\,\text{MPa}, 350\,\text{MPa}, 100)$ is set as the initial guess for future iterations. The identified material is noted as M_4, and the three parameters are compared with their reference values in Table 5.2. We observe that we are able to retrieve the three parameters with reasonable accuracy by 16 iterations. A maximum error of 2.14% is observed for the third parameter γ.

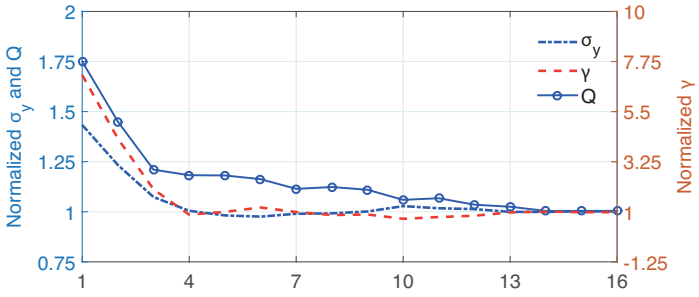

FIGURE 5.9 Convergence summary for the three Voce parameters (M_4) normalized by their corresponding reference values (initial point $\boldsymbol{\mu}_A$).

TABLE 5.2 Identified Voce parameters using different initial points, $E = 70$GPa, $\nu = 0.33$ and $h_{\max} = 0.1$mm.

Identified material	σ_y (MPa)	$\frac{\lvert\sigma_y^* - \sigma_y\rvert}{\sigma_y^*}$	Q (MPa)	$\frac{\lvert Q^* - Q\rvert}{Q^*}$	γ	$\frac{\lvert\gamma^* - \gamma\rvert}{\gamma^*}$
M_4	300.50	0.17%	200.88	0.44%	13.70	2.14%
M_5	260.29	13.24%	201.15	0.57%	41.50	196.43%

In Figure 5.9, we present the convergence histories for the three Voce parameters, normalized by their corresponding reference/nominal values, σ_y^*, Q^* and γ^*. Figure 5.10 shows the iteration history for the cost function Equation 5.1. Its steady decline confirms the robustness of the identification algorithm. Several selected imprints simulated using the parameter values $\boldsymbol{\mu}_t^*$ are also compared with the target shape at various stages during the identification.

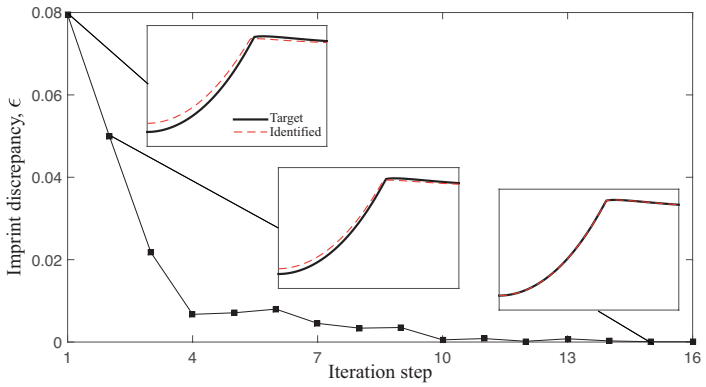

FIGURE 5.10 Minimizing the discrepancy between the simulated (M_4) and target (pseudo-experimental) imprints (initial point $\boldsymbol{\mu}_A$).

Next, we also select $\boldsymbol{\mu}_B$: (200 MPa, 600 MPa, 140) as another initial point for the algorithm. The convergence histories are shown in Figure 5.11, and the identified material is denoted by M_5. The final identified parameters are compared with those obtained when starting from $\boldsymbol{\mu}_A$, in Table 5.2.

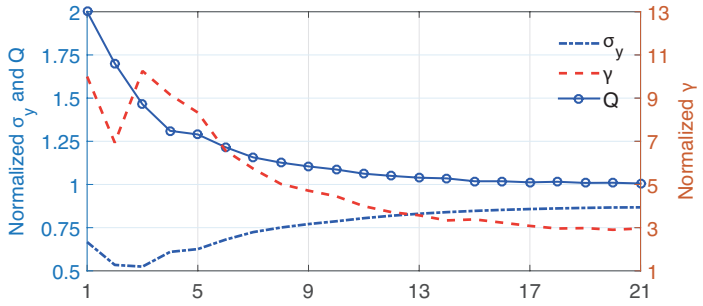

FIGURE 5.11 Convergence summary for the three Voce parameters (M_5) normalized by their corresponding reference values (initial point $\boldsymbol{\mu}_B$).

As observed from Figure 5.11, despite stabilizing around a particular set of values, only ONE of the three parameters (Q) converges correctly to the reference value. A large deviation is seen for γ in particular, with an error of up to 200% ! Nevertheless, Figure 5.12 shows a steady decline in the discrepancy between the identified and target imprints and we end up with an acceptable error of 0.002.

For the two identified materials, we reconstruct their constitutive behaviors by using the identified parameters listed in Table 5.2, and compare them in Figure 5.13. We observe that, even in the case where both measurement and model errors are absent, it appears difficult to accurately/uniquely identify the differences in the post-yield properties of the Voce law using only the indentation imprint. In other words, the two identified parameter sets supposedly form a "mystical pair", both minimizing the discrepancy with the "experimental" imprint.

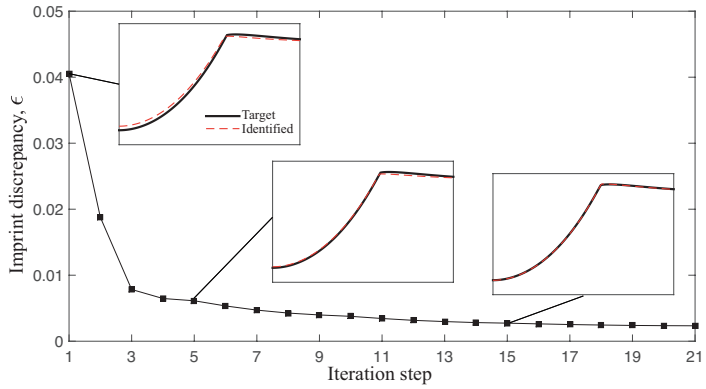

FIGURE 5.12 Minimizing the discrepancy between the simulated (M_5) and target (pseudo-experimental) imprints (initial point $\boldsymbol{\mu}_B$).

The corresponding indentation *P-h* curves are now compared to check whether the two "mystical sibling" materials can be distinguished from each other by using all available indentation responses. We note in Figure 5.14 that, despite the constitutive behaviors of the two materials being clearly distinct, the two indentation curves are nearly overlapping. With

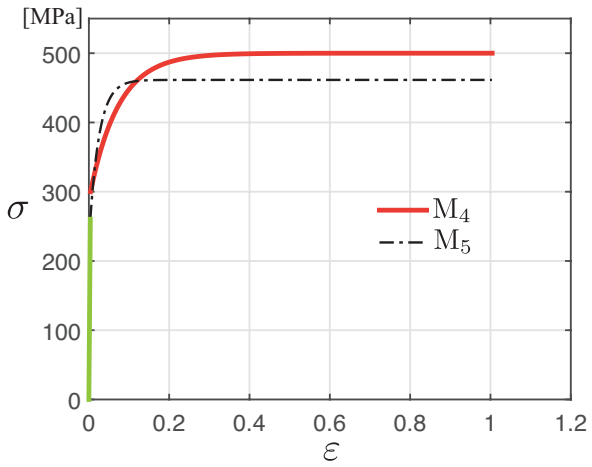

FIGURE 5.13 A comparison of tensile curves for (M_4, M_5) rebuilt using Voce law with the identified parameters.

these considerations, the combination of *P-h* curve and imprint does not seem helpful in the current case. The questions we are asking then are :

Q1 : is this failure in characterization of Voce parameters due to the reduced-order space and/or the optimization algorithm used in the inverse analysis ?

Q2 : does the collected/measured information from the indentation response not interpret material plasticity *adequately* ?

These two questions will be addressed in the following chapter to investigate the root of the problem of non-unicity with respect to Voce parameter identification.

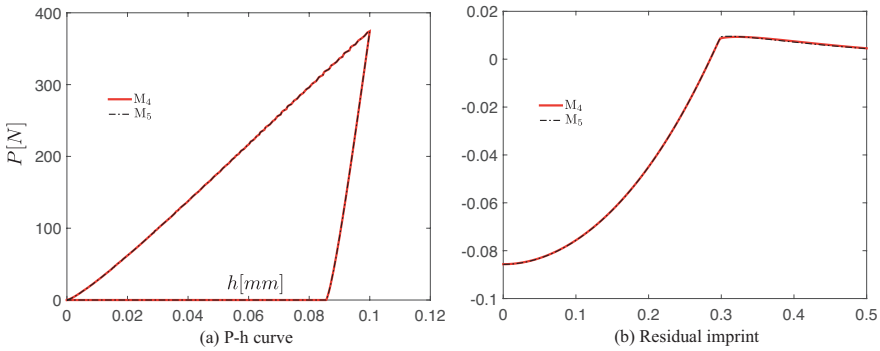

FIGURE 5.14 A comparison of indentation responses for a mystical material pair (M_4, M_5) for Voce law.

5.5 Closing remarks

In this chapter, to further verify this insights gained from global manifold, we proposed to iteratively construct a series of *local*-manifolds with a moderate cost. A family of local-manifold learning algorithms, including *panning, zooming*, *panning & zooming* as well as *floating search*, were developed to explore the parametric space by means of intensification and exploration. Three identification procedures were carried out to identify two Hollomon's parameters in considering different indentation responses. The identification results were found to be coincident with what we have concluded from global manifolds in Chapter 4.

Furthermore, we have also identified in Section 5.4 a three-parameter Voce law in the aim of generalizing the insights observed from Hollomon's law. For a synthetic imprint, free from model and measurement error, we obtained however two different material parameter sets, both minimizing the inverse cost function. The non-unique solutions underlined that a single imprint could be insufficient to characterize materials hardening according to Voce law. We noticed also that even by combining with the *P-h* curve the unique identification seems not to be possible either. With these considerations, new protocol needs to be proposed with respect to Voce law and this is the focus of the next chapter.

Chapitre 6

On the uniqueness of Voce law parameters' identification

In the two previous chapters, the uniqueness issue with respect to the identification of Hollomon's material has been thoroughly studied under the framework of global and local manifold. The mystical Hollomon's materials have been demystified taking into account the residual imprint. However, Section 5.4 indicates that the critical question of unicity still remains unanswered for Voce parameters' identification.

We therefore devote this chapter to investigating the source of this non-unicity. The two questions that we posed at the end of Section 5.4 will be answered one after the other. To first verify the efficacy of the manifold-based identification protocol, we will temporarily leave the indentation context and consider using a different representation of the constitutive behavior for the identification. Since the σ-ε curve is universally accepted to fully represent the material plastic behavior, the robustness of the identification *method* can be easily verified if we are able to perform a unique identification. Then, by examining the imprint manifold as well as its intrinsic dimensionality, the inadequacy of a single indentation test will be demonstrated. Finally, a deeper inspection is conducted on the "indistinguishable" materials, and a *new* protocol is finally proposed to alleviate the non-uniqueness issue in the identification problem.

In the remainder of this chapter, we first verify in Section 6.1 the efficacy of the manifold-based identification procedure using a series of synthetic σ-ε curves. In Section 6.2, with the help of the global manifold, we then illustrate the existence of indistinguishable materials by a single indentation test. The concept of "mystical material pair" is extended from Hollomon's materials to Voce materials, the only difference being that two groups owe their respective existence to different causes. The possibility of using the dual-sharp indentation technique to distinguish these mystical materials is investigated in Section 6.3.1, and finally we propose a

protocol to uniquely calibrate the Voce law using multi-depth indentation in Section 6.3.2. Closing comments are provided in Section 6.4.

6.1 Unique identification from σ-ε curve

In this section, to first answer the question Q1 raised at the end of Section 5.4, we will first verify the efficacy of the shape-manifold identification procedures for the three-parameter law using *tensile curves* in place of the indentation responses.

6.1.1 Comparison of global manifolds for Voce law

We temporarily leave the indentation context in this section and revisit the uniaxial stress strain (σ-ε) curves, *directly* considering them as the high-dimensional input "shapes". For the convenience of readers, we recall here in Figure 6.1 several global manifolds based on stress-strain curves of different constitutive laws in Section 3.4.2. It is observed from the global manifold (f) that the three Voce parameters can be identified *uniquely* from the *stress-strain curve* in view of the one-to-one correspondence between tensile curves and points from manifolds, using interpolation techniques.

6.1.2 Local manifold identification of Voce law

For the sake of completeness, we carry out eight different identification procedures for the Voce parameters by directly considering the uniaxial stress-strain behaviors as "shapes" within the manifold approach using different starting points. The σ-ε curve obtained from the set $\mathrm{M_{trg}} : (\sigma_y, Q, \gamma) = (300\ \mathrm{MPa}, 200\ \mathrm{MPa}, 25)$ is used as the "target shape", and the parameter set to be identified is located (by design) at the centroid of the cube enclosed by the alternative eight initial points as vertices, as illustrated in Figure 6.2.

Table 6.1 lists the final estimates for the three parameters and the number of iteration steps for each corresponding case. We note that, in all eight cases, we always converge to a unique combination of parameters. A maximal difference of 0.16% and 0.1% is observed for γ and Q with respect to their respective target values, thus the identification results are considered unique in view of possible inaccuracy of the local manifold. Analogously, two other identification procedures have also been carried out using Hooke's and Hollomon's power law and we reach similar conclusions in both cases, therefore we have omitted the corresponding iteration histories from this discussion. The inference proposed in Section 3.4.2 to correlate the number of identifiable parameters to the intrinsic dimensionality of manifold is therefore validated by identification results.

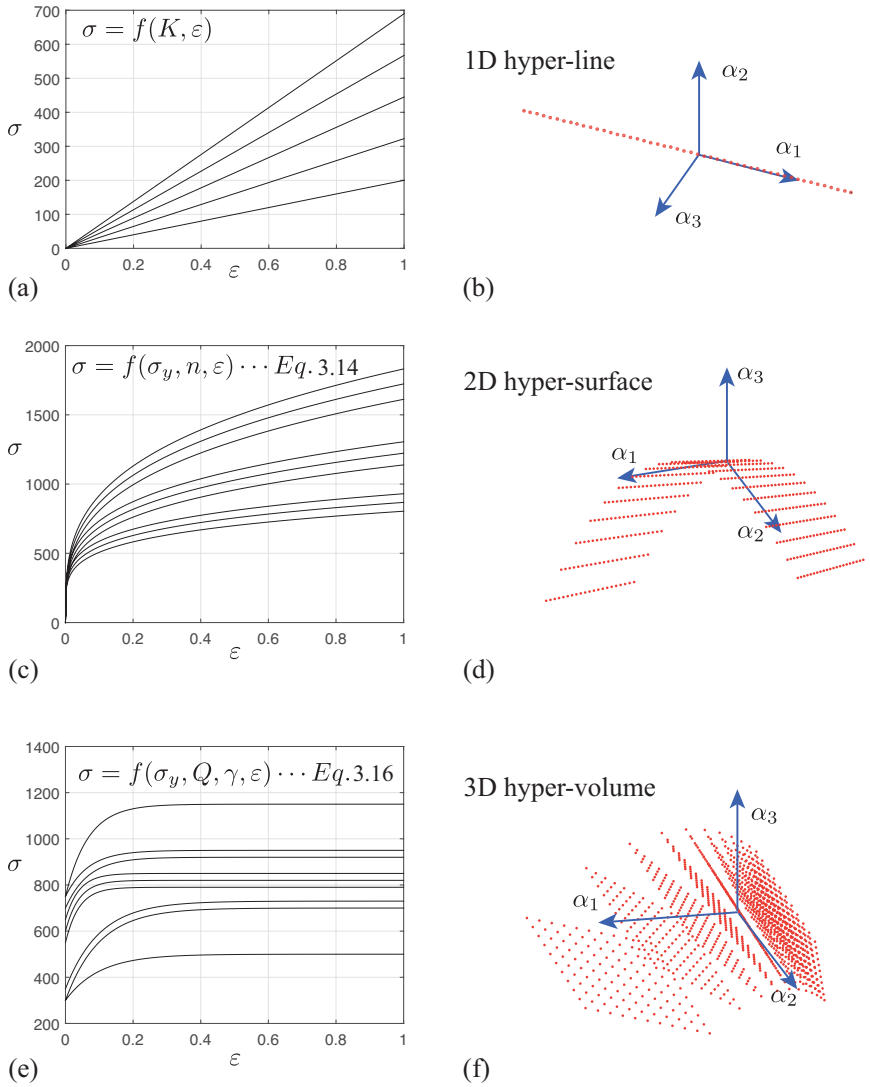

FIGURE 6.1 Illustrative stress-strain curves and the corresponding low-dimensional embeddings for (a)-(b) perfectly elastic (Hooke's law), (c)-(d) Hollomon's power law hardening, and (e)-(f) Voce law hardening

On the other hand, it goes without saying that no iteration is really required for probing material parameters from the uniaxial stress-strain constitutive law and that the identification could be readily accomplished by simple curve fitting provided that the target σ-ε curve has already been obtained from a tensile test. That said, the identification procedures presented above, though redundant and bordering on overkill for this simple problem, still help us to rule out any possibility of an inefficiency of manifold method or other issues surrounding either the manifold hypothesis or identification algorithm we have used, and the first question raised at the end of Section 7.4 is thus answered.

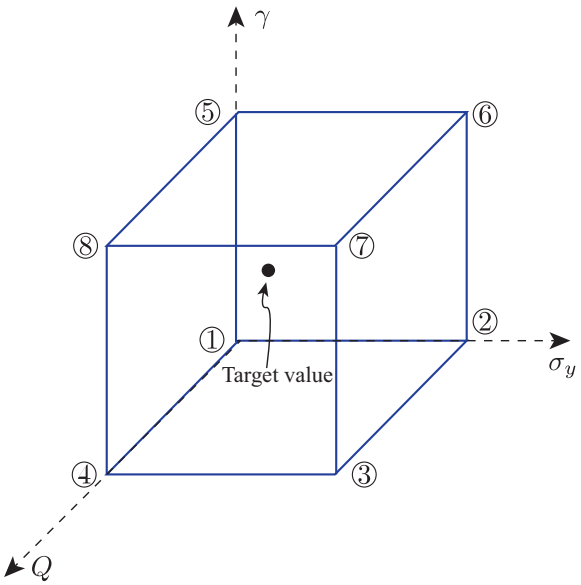

$\sigma_y \quad Q \quad \gamma$
①: (100, 100, 10)
②: (500, 100, 10)
③: (500, 300, 10)
④: (100, 300, 10)
⑤: (100, 100, 40)
⑥: (500, 100, 40)
⑦: (500, 300, 40)
⑧: (100, 300, 40)
●: (300, 200, 25)

FIGURE 6.2 The "target" material parameters (black dot) and eight different parameter combinations chosen as initial points in parameter space.

TABLE 6.1 Voce parameters identified from various starting points using the stress-strain curve.

Initial points	σ_y [MPa]	Q [MPa]	γ	Iter No.
①	299.96	200.08	25.02	34
②	300.08	199.86	24.96	34
③	299.92	200.12	25.04	25
④	299.93	200.10	25.04	21
⑤	299.93	200.19	25.03	23
⑥	299.97	200.03	25.02	28
⑦	299.96	200.11	25.02	23
⑧	300.02	199.95	24.99	33
M_{trg}	300	200	25	–
Max error	0.03%	0.10%	0.16%	–

6.2 Inadequacy of "single depth" indentation

6.2.1 Comparison of global indetation manifolds

We return now to the indentation responses : residual imprints for Hollomon's and Voce law, and *P-h* curve for Hooke's since no plastic deformation is present. An analogous procedure to the one explained in Section 6.1.1 is followed.

On the left of Figure 6.3, we show collections of representative indentation responses for varying material parameters according to the DoE in Section 6.1.1. The indentation

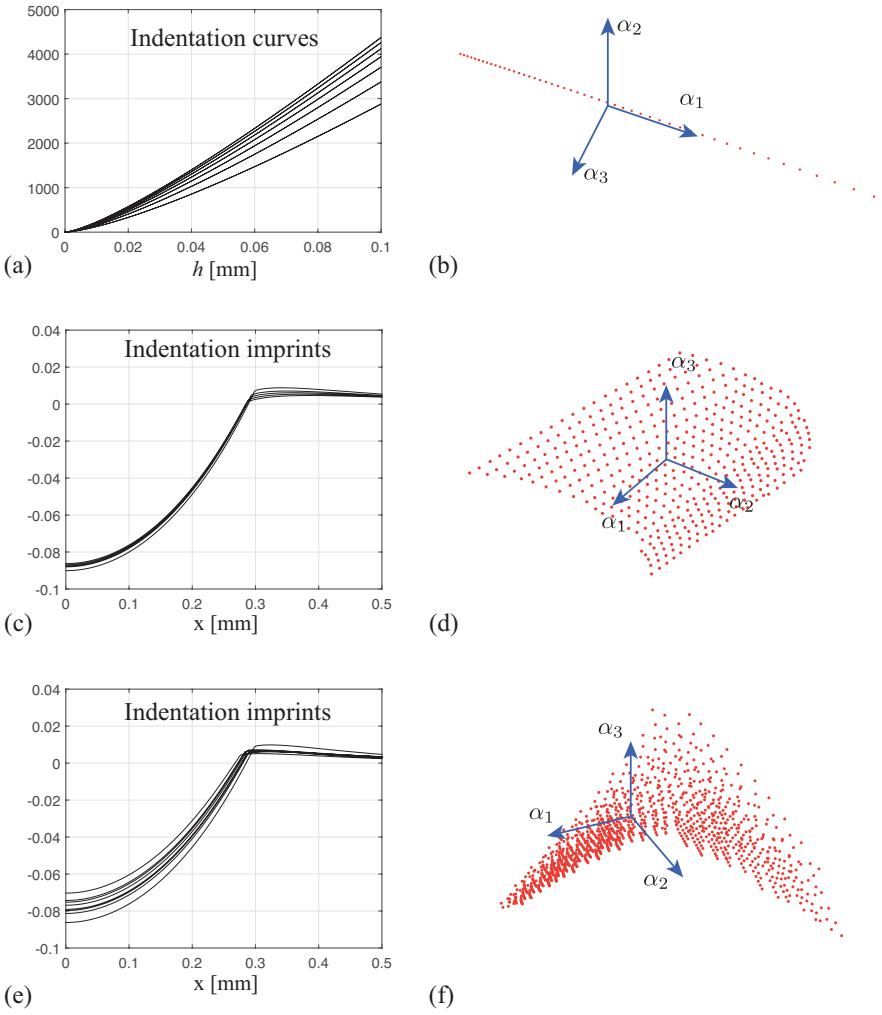

FIGURE 6.3 High-dimensional indentation responses and the corresponding embeddings for different constitutive laws : (a)-(b) perfectly elastic (Hooke's law) (c)-(d) Hollomon's law, and (e)-(f) Voce law.

responses projected into the shape space reduced to 3D are shown on the right, allowing for the following observations :

— the feature of the point cloud for Hooke's law is, once again, intrinsically unidimensional, Figure 6.3 (b) ;

— for residual imprints obtained according to Hollomon's power law, Figure 6.3 (c), their 2D distribution in reduced shape-space confirms that the non-unicity issue does not present itself in this case either, Figure 6.3 (d) ;

— for imprints based on Voce law (governed by three independent parameters, as shown in the previous section, Figure 3.9 (e)-(f)), the point cloud appears to follow a more complex behavior, locally approaching a quasi-2D hyper-surface, Figure 6.3 (f) ! As

a consequence, the combination of material parameters identified assuming the Voce law requires further investigation.

By excluding the inefficacy of manifold protocol in identification, we conclude that the possibility of unique identification of Voce materials rests with the employed measurements, which may or may not interpret all material plasticity in one test. We have by now answered the second question raised in Section 5.4.

6.2.2 The concept of "true" and "false" mystical pairs

In Section 5.4, we have observed a mystical pair (M_4, M_5) obtained from two identification procedures with different initializations. In this section, based on the manifold in Figure 6.3 (f), we intend to find out more mystical pairs and locate them in the parametric space to investigate the source of non-unicity. To this end, the similarity between imprints needs to be quantified so as to define mystical materials. Instead of using the objective minimization function ε in Equation 4.11, following [46] we quantify the level of agreement between experimental and simulated indentation responses with a *dimensionless* indicator : "goodness of fit"

$$g = 1 - \frac{\varepsilon}{\|\boldsymbol{s}^*\|_{L_2}}, \tag{6.1}$$

which varies between 0 and 1. A value of 1 represents a "perfect fit". Alternatively, imprints giving g values close enough to 1 are considered indistinguishable, and we thus consider the corresponding materials as a mystical pair.

For the 1331 imprint snapshots in Figure 6.3 (f), we plot in the σ_y-Q-γ space (Figure 6.4) the map of the goodness of fit, g, Equation 6.1, w.r.t the identification target M_t ($\sigma_y =$ 550 MPa, $Q = 300$ MPa and $\gamma = 110$). All materials that produce nearly identical imprints (with $g > 0.995$) after indentation—the blue points in the figure—are located within a "husk of corn"-shaped zone, stretching along the diagonal direction (dashed-line). This is similar to the results obtained for the case of non-unique identification of Hollomon's power law parameters for conical indenters in [104, 103].

We choose two siblings of M_t, i.e., M_6 and M_7, with extreme values of γ. Their corresponding constitutive behaviors are compared in Figure 6.5. For M_t and M_7, the σ-ε curves are very close to each other and their saturation stresses at high strain level are the same. We call them a *"false mystical pair"* due to the similarity of their constitutive behaviors. We suggest for this group of mystical materials that the difficulty in unique identification seems to be related to the parameterization of certain materials, rather than the indentation mechanism, partly due to the compensation of underestimating of σ_y by overestimating γ. Nevertheless, a clear difference can be observed between that of M_t and M_6, and we term

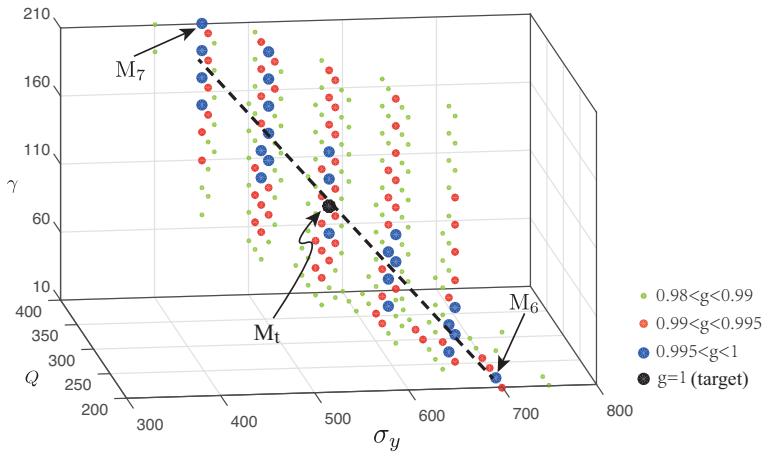

FIGURE 6.4 Goodness of fit (Equation 6.1) for the 1331 imprints using a spherical indenter.

them as a *"true mystical pair"*, referring to materials with completely *different rheological behaviors*, yet with nearly indistinguishable indentation responses.

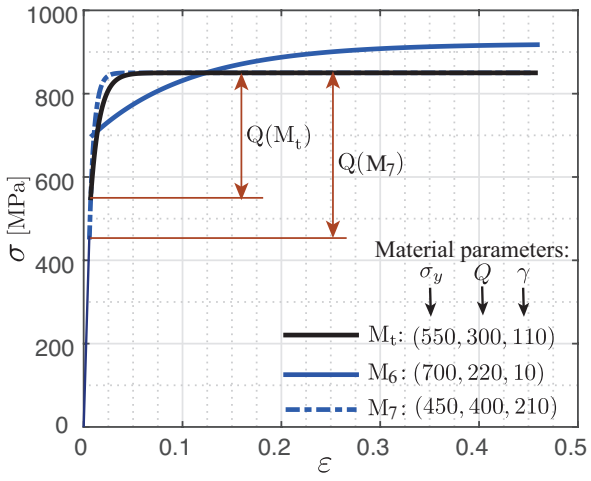

FIGURE 6.5 Two mystical material pairs using the Voce hardening law : (Mt, M_6) the *true* mystical material pair, and (Mt, M_7) the *false* mystical material pair.

Besides, by examining the corresponding material parameters, we note that there appear to be more mystical siblings for materials with a higher γ. This is understandable, since γ dominates mainly the transitional portion of the σ-ε curve, and for materials with higher γ, this transitional phase is relatively short and thus is difficult to be properly captured by the indentation test.

6.3 Alternative identification techniques

6.3.1 Dual-sharp indentation

Inspired by [27, 37, 32], dual-sharp indentation may be helpful to *uniquely* determine the Voce parameters. As proposed in [46], for each indenter shape, a g-map characterizing the similarity of imprints indented for different materials is first generated in form of " cloud" points within the design space. Then, after superimposing multiple clouds (corresponding to different indenter shapes), a "master cloud" is obtained (with the value associated with each point equal to the average/minimum for that point). Finally, the best fit solution would be the point in this master cloud with the highest value of g.

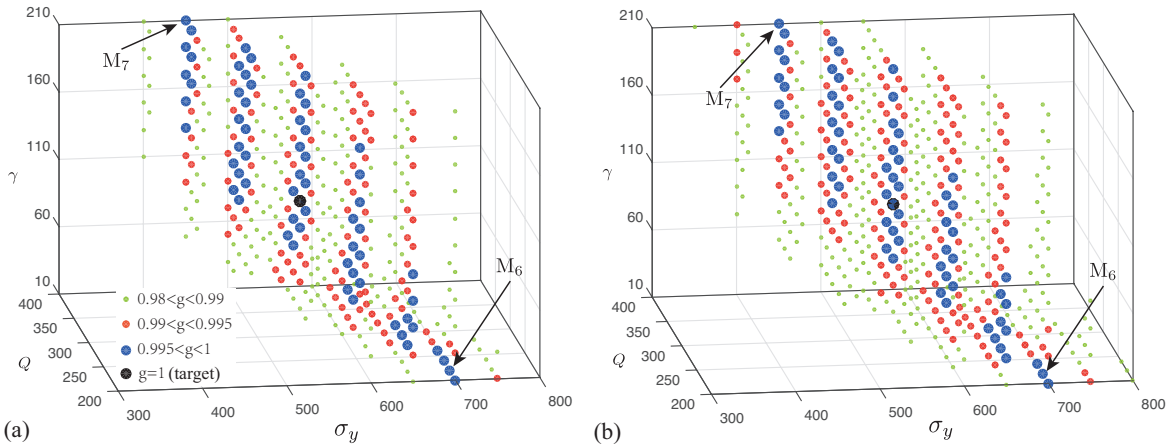

FIGURE 6.6 Goodness of fit for Voce imprints using dual-sharp indentation with : (a) $\theta = 70.3°$, and (b) $\theta = 63.14°$.

We therefore build two other databases for the two sharp conical indenters with half apex angle $\theta = 70.3°$ and $\theta = 63.14°$, respectively. Contrary to what one may expect, both M_6 and M_7 *remain* mystical siblings for M_t, as indicated in Figure 6.6. Even when the two clouds are superimposed, the two materials are still present in the master cloud (the corresponding cloud is omitted here). On the other hand, we observe additional mystical material siblings, the distribution of which appears to follow the same direction as indicated in Figure 6.4. We attribute this deterioration to the self-similarity of conical indenters.

In light of the above, we conclude that dual-sharp indentation may *not improve* the identification results, and the unique inverse identification of Voce hardening parameters is not guaranteed.

6.3.2 Multi-depth indentation protocol

As seen in Figure 4.16, the difference between mystical materials can be observed around the pile-up zone, and we speculate that this difference may be more pronounced with deeper indenter penetration, producing an alternative way to differentiate between mystical siblings of Voce hardening materials. Therefore, we propose in this section performing multiple indentation tests using *different* indentation depths.

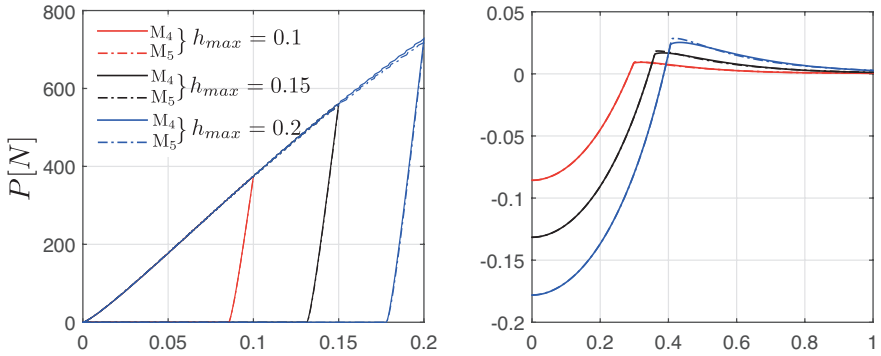

(a) P-h curve (b) Residual imprint

FIGURE 6.7 Multi-depths indentation responses for the mystical material pair $(M_4, M_5)_{R=0.5}$ (Figure 5.14).

For the mystical material pair (M_4, M_5) in Table 5.2, we perform three indentation tests using the same spherical indenter. The maximal penetration depths are designed to equal to 0.1 mm, 0.15 mm and 0.2 mm, respectively. The indentation responses are observed in Figure 6.7. Also, we list in Table 6.2 the maximal pile-up heights observed from different imprints, and we note that M_4 and M_5 become distinguishable in view of their increasing difference of the pile-up heights.

TABLE 6.2 Comparison of pile-up heights for M_4 and M_5 with diverse penetration depths.

Indentation depth	$h_{\max} = 0.1$ mm	$h_{\max} = 0.15$ mm	$h_{\max} = 0.2$ mm
M_4	0.0093	0.0169	0.0253
M_5	0.0096	0.0184	0.0285
Difference	0.0003	0.0015	0.0032
Relative difference	3.13%	8.15%	11.23%

Then, following the same routine as for the dual-sharp indentation, we combine the three databases obtained for different penetration depths by superposing the clouds of points in the map of goodness of fit (Figure 6.8) to obtain a master cloud. We note that more than one material parameter set lead to almost indistinguishable imprints for all levels of loads, which means that the mystical materials, either *"true"* or *"false"*, are still present for multi-depth

indentation. However, fewer mystical siblings (i.e., the blue points) are observed compared with either single (Figure 6.4) or dual-sharp indention (Figure 6.6). More importantly, it is observed that M_6, one of the true mystical material w.r.t. M_t, is excluded from the mystical siblings.

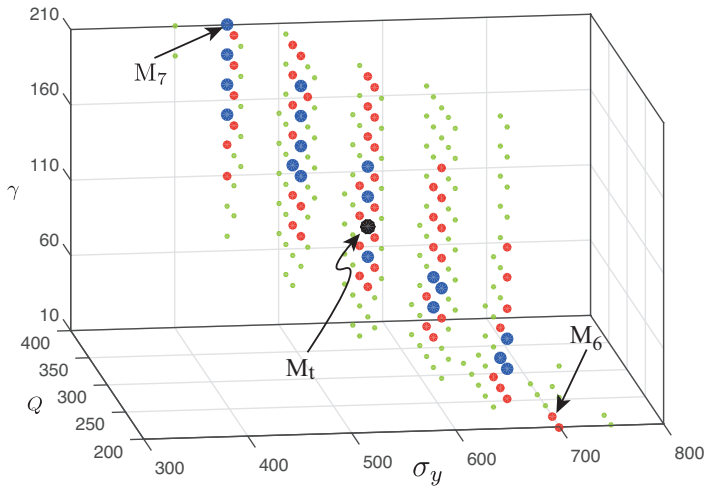

FIGURE 6.8 Goodness of fit for indentation imprints using multi-depths indentation : the "true mystical material" M_6 is readily separated from others.

In Figure 6.9, the material behaviors of all those mystical siblings are then plotted in blue lines. We notice that all of them are constructed with relatively large values of γ ($\gamma \geq 50$) and their saturation stresses are almost the same, belonging thus to the *"false mystical materials"* described in Section 6.2.2. On the other hand, we plot in the same figure the stress-strain curve of M_6 (red dashed line), which as a result can be readily distinguished from the *"false mystical materials"*. Thus, the *"true mystical material"* M_6 is demystified with multi-depths indentation.

To conclude, we consider multi-depth indentation as a possible approach to make the difference between *"true"* and *"false"* mystical pairs for materials following Voce law. The presence of false mystical siblings finds some of its roots in the parameterization of the constitutive law, and partly in the inefficiency of indentation in capturing certain material properties, γ for instance. However, this conclusion is based on a global manifold observation and purely synthetic data, more verifications are required, thus the unique identification of Voce parameters remains an unsolved problem to this day.

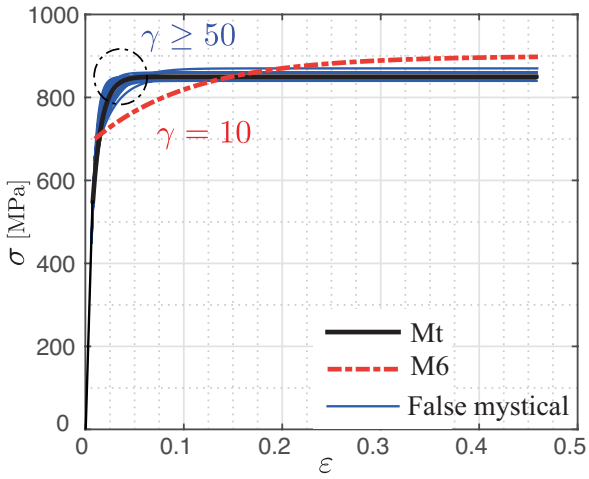

FIGURE 6.9 *"True"* mystical material that is distinguished with multi-depth indentation.

6.4 Closing remarks

In this chapter, the source of the non-unicity problem in probing Voce parameters was carefully investigated, and we found that this is essentially due to the inadequacy of a single indentation test in capturing material plasticity. By defining an indicator of similarity between imprints, we located, in the parametric space, a group of mystical siblings for the Voce law, which were later divided into two groups : (a) the *"false mystical pair"* which has relatively close uniaxial stress-strain curves, and (b) the *"true mystical pair"*, whose constitutive behaviors are quite different yet the indentation responses virtually indistinguishable.

We have also demonstrated that dual-sharp indentation, albeit useful for uniquely identifying Hollomon's power law parameters, may *not* improve the identification results for Voce hardening materials. However, multi-depth indentation, which tends to provide us with more information about plastic deformation around pile-up zone, allows us to differentiate between *true* and *false* mystical siblings.

That said, since Chapter 4, we have been focusing on purely numerical data without adding any noise, therefore solid verification needs to be actively pursued as a future work. In the next chapter, the gleaned insights will be verified by iterative identification procedures using several experimental measured imprints. The manifold-based identification protocol as well as the developed manifold learning algorithms will be employed to characterize three engineering materials.

Chapitre 7

Identification from experimental imprint obtained from spherical indentation

In the previous chapters, we have verified the efficiency of the manifold protocol using *synthetic* data, where both measurement and model errors were clearly absent. In this chapter, the identification approach in reduced shape-space is performed with actual experimental measurements after spherical indentation on industrial alloys.

Since we have proposed the use of the imprint to alleviate the non-uniqueness issue in previous chapters, we retain it as the primary focus of study in this chapter. Experimental imprints were measured with a laser scanning microscope. A variety of engineering materials, including the AISI 1095 steel and two different aluminum alloys EN AW-2017F and EN AW-5754F, have been characterized by assuming both the Hollomon's as well as the Voce hardening laws. Different local-manifold learning algorithms, i.e., *panning*, *zooming*, *panning & zooming* as well as "floating search" have been adopted.

This chapter is organized in the following manner : Section 7.1 presents the materials' preparation and related details of the indentation testing. In Section 7.2, identification results obtained by employing the different algorithms are compared for the AISI 1095 steel. Section 7.3 showcases the application of the manifold learning protocol combined with the "floating search" algorithm on the two aluminum alloys. In Section 7.4, the three materials are also characterized by assuming Voce hardening, showing the existence of materials that can be characterized by different laws. We also present a comparison of tensile curves "rebuilt" from the identified parameters for both material laws. Concluding remarks are given in Section 7.6.

7.1 Materials and experimental techniques

Three materials were selected for this study : a spheroidized AISI 1095 steel, an aluminum alloy EN AW-2017F and an aluminum alloy EN AW-5754F. These materials were selected because of their fine and homogeneous microstructure which should lead to a good reproducibility of the indentation tests. We chose the AISI 1095 steel as the main test case, with which the robustness of the identification procedure will be carefully verified in Appendix C.

7.1.1 Test materials

The spheroidized AISI 1095 steel is an unalloyed steel containing approximately 1 % of carbon that has been treated in order to transform the pearlite phase into cementite globules and ferrite. It has a body-centered-cubic (BCC) structure [38]. The standard spheroidizing annealing was carried out prior to delivery. The steel has the chemical composition shown in Table 7.1. The microstructure of this steel, shown in the optical micrograph in Figure 7.1, reveals a homogeneous and isotropic distribution of spheroidized cementite particles in a ferritic matrix.

TABLE 7.1 Composition of the AISI 1095 steel used in this study given in % of weight content.

C	S	P	Mn	Fe
0.90 -1.03	$\leq$ 0.05	$\leq$ 0.04	0.30 - 0.50	98.38 - 98.8

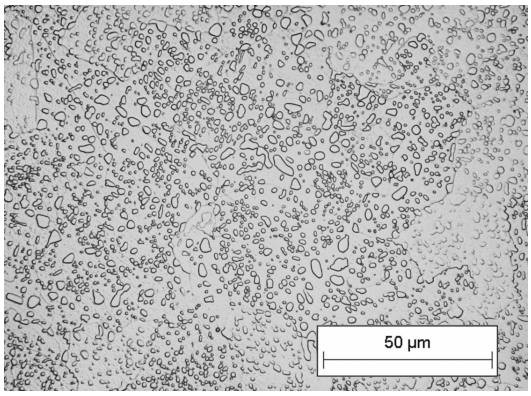

FIGURE 7.1 Microstructure of AISI 1095 steel.

The EN AW-2017F aluminum alloy is the second material with the chemical composition shown in Table 7.2. For this alloy, fine particles of inter-metallic phases Al_2Cu compounds oriented toward the rolled direction can be distinguished in Figure 7.2.

TABLE 7.2 Composition of the EN AW-2017F aluminum alloy used in this study given in % of weight content.

Cu	*Mg*	*Mn*	*Si*	*Fe*	*Al*
4.18	0.518	0.719	0.679	0.258	*balance*

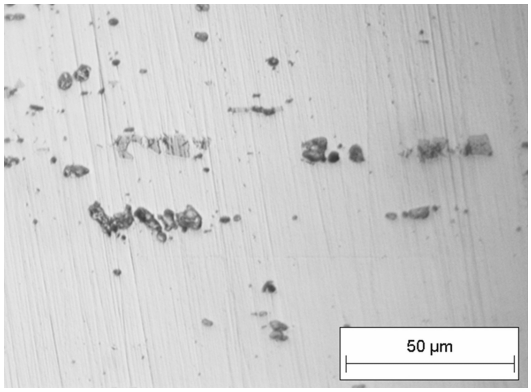

FIGURE 7.2 Microstructure of EN AW-2017F alloy.

The third material is the EN AW-5754F aluminum alloy with the chemical composition shown in Table 7.3. This alloy is frequently used in flooring applications due to its high weldability and corrosion resistance. The microstructure showing the size and the distribution of the $AlMg_2$ compounds is given in Figure 7.3.

TABLE 7.3 Composition of the EN AW-5754F aluminum alloy used in this study given in % of weight content.

Si	*Fe*	*Mn*	*Mg*	*Al*
0.4	0.4	0.5	3.2	*balance*

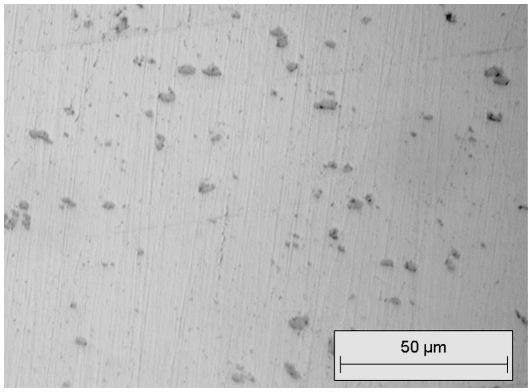

FIGURE 7.3 Microstructure of EN AW-5754F alloy.

7.1.2 Indentation set-up and procedure

Indentation tests were conducted on the three samples using the setup shown in Figure 7.4. We have used an industrial indenter composed of a tip bonded to the indenter holder (as opposed to a mono-block indenter which is a monolithic entity). The indenter has a spherical tip (Figure 7.5) with radius $R = 0.5$ mm made of Tungsten Carbide with $E_i = 600$ GPa and $\nu_i = 0.23$ (elastic properties measured by ultrasound), but the rest of the apparatus is composed of steel. The advantage of this type of indenter is that it is easy to produce and is available from many manufacturers. The disadvantage is that the mounting of the sphere presents modeling difficulties, and may also lead to a nonlinear load-displacement response in the assembly, thus is known to not give a very useful *P-h* curve on account of the presence of compound between the indenter and the indenter holder.

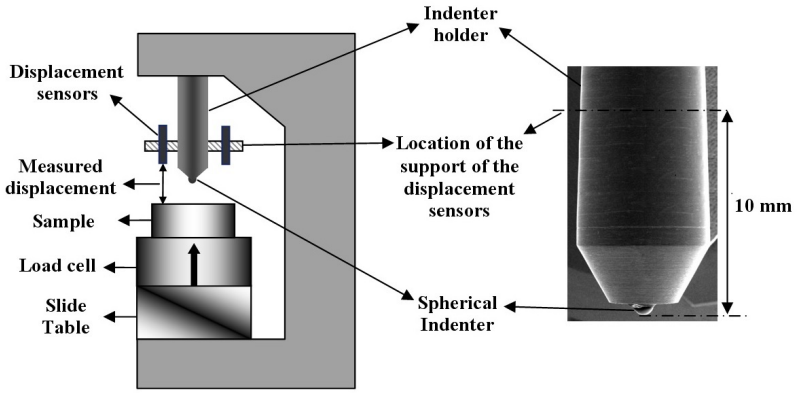

FIGURE 7.4 Experimental set up for indentation.

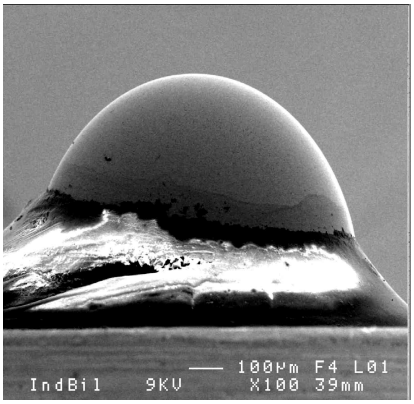

FIGURE 7.5 Spherical indenter tip measured by a Scanning Electron Microscope(SEM).

7.1.3 Analyzing the imprint shape

The experimental imprint shapes were measured using a metrological machine Altisurf 500 that works on the optical principle of chromatic confocal imaging (Figure 7.6). The maximum measurement range of the system is $100 \times 100 \times 100$ mm. The high-precision and DC motorized shifting platform allows the movement of the sample being controlled along X and Y axes with a minimum stepping of 0.1 μm.

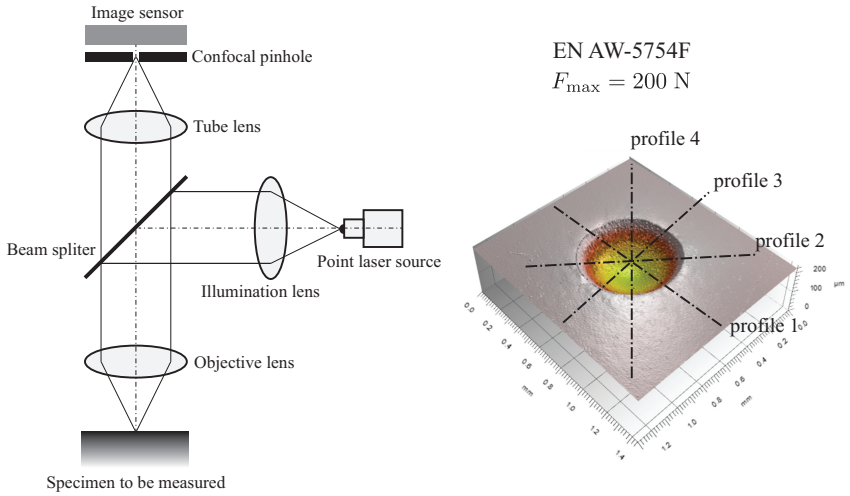

FIGURE 7.6 Confocal laser imaging setup and a typical scanned imprint on an aluminum alloy EN AW-5754F.

The measurement of each imprint shape was performed by using a non-contact sensor, i.e., CL2 Confocal chromatic probe, whose axial and lateral accuracy are 0.08 μm and 1.7 μm, respectively. In consideration of the used indenter and the size of our imprints, only a vicinity of the imprint center (a 2mm $\times$ 2mm zone) is scanned, and a rather large step length of 10 μm was chosen to accelerate the measurement. As a result, each imprint was then pixelized using a resolution of 200×200.

Considering the axial symmetry of indenter and material isotropy, 2D imprint profiles instead of 3D mappings are employed for identification. One should note that a fast correcting of the as-measured imprint is always applied before deducing each profile in the aim of obtaining an imprint : (a) with a summit located in $x = 0$; and (b) with the undeformed specimen surface on $z = 0$. In fact, (a) is required to match more easily with simulated imprint from FE as illustrated in Figure 4.4, while (b) is due to a problem of parallelism between the lower surface and the upper surface of the sample (correcting for planeness).

In the current work, the 3D imprint was "reduced" to a 2D profile (Figure 7.7) by using the mean profile from 4 different profiles with axes of symmetry oriented at 45° with each

other (see Figure 7.6). Of course, for anisotropic materials or pyramidal indentations, we should use the entire 3D imprint.

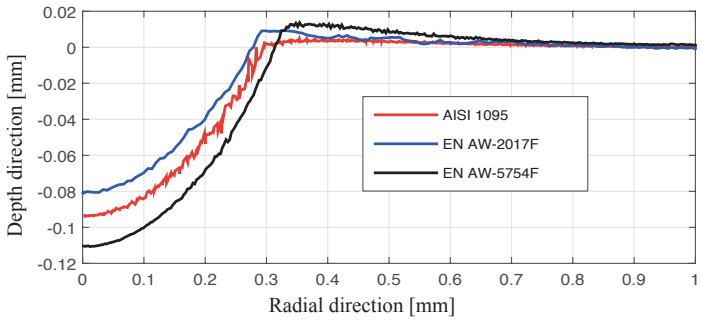

FIGURE 7.7 Experimentally measured imprints for the three considered materials.

The maximum values of the indentation force $P_{\max}$ are 500 N, 360 N and 200 N, respectively, for the three studied materials. The reason these particular maximum loads were chosen has to do with obtaining imprints of similar size for the three materials ($h_{\max}/R \simeq 0.2$). This ratio is important since [32] showed that a sufficient accuracy of the results is obtained only for a sufficiently high $h_{\max}/R$ ratio. Though proposed with regard to the loading-unloading curve, it is still adopted for the imprint to neglect the bluntness of the indenter or size effect. On the other hand, if extremely high value is chosen for this ratio, the results may be strongly influenced by the choice of friction coefficient.

7.1.4 Experimental employment

When solving the inverse problem within the reduced shape-space, the distance between imprints in Equation 5.1 may be computed in a variety of ways, the choice of the particular method used depending mainly on the linearity of the manifold. For linear cases, the Euclidean norm is accurate enough to characterize the distance, while for highly nonlinear manifold like that shown in Figure 2.1, a geodesic distance is required. Note that if we define $dist(\cdot)$ as $\|\cdot\|_{L2}$, the convergence criterion in Equation 5.1 is equivalent to

$$\boldsymbol{s}_t^* = \boldsymbol{s}(\boldsymbol{\mu}_t^*) = \underset{\boldsymbol{s}}{\operatorname{argmin}}\, dist(\tilde{\boldsymbol{s}}_{\text{exp}},\, \boldsymbol{s}(\boldsymbol{\mu})), \tag{7.1}$$

where $\tilde{\boldsymbol{s}}_{\text{exp}}$ refers to the projection of the experimental imprint reconstructed from POD modes

$$\tilde{\boldsymbol{s}}_{\text{exp}} = \bar{\boldsymbol{s}} + \boldsymbol{\Phi}\boldsymbol{\Phi}^{\text{T}}(\boldsymbol{s}_{\text{exp}} - \bar{\boldsymbol{s}}) = \bar{\boldsymbol{s}} + \boldsymbol{\Phi}\boldsymbol{\alpha}_{\text{exp}}. \tag{7.2}$$

We are aware that in local manifold methods both $\boldsymbol{\Phi}$ and $\bar{\boldsymbol{s}}$, as well as $\boldsymbol{\alpha}_{\text{exp}}$ are adaptive, and the subscript t is omitted in Equation 7.2 for simplicity sake. Moreover, we recommend that more attention be paid to the difference between $\tilde{\boldsymbol{s}}_{\text{exp}}$ and $\boldsymbol{s}_{\text{exp}}$.

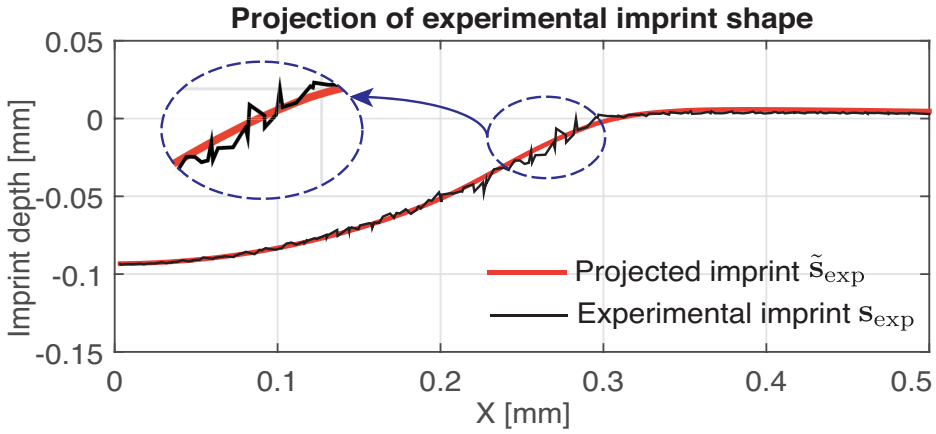

FIGURE 7.8 Projection of an experimental imprint to α-space.

Taking the imprint of AISI 1095 as an example, we compare $\tilde{\boldsymbol{s}}_{\text{exp}}$ with the experimental imprint $\boldsymbol{s}_{\text{exp}}$ in Figure 7.8. It is noticed that the measurement noise is smoothed out when projecting noise data into the reduced space. This is understandable since both the mean snapshot and POD modes are obtained from a series of smooth simulated imprints, and by consequence, their linear combination $\tilde{\boldsymbol{s}}_{\text{exp}}$ must be smooth as well. Therefore, the projection of the experimental zig-zag imprint in α-space may be considered as a physics-based smoothing procedure of experimental measurement. In this sense, the imprints are employed directly as illustrated in Figure 7.7.

7.2 AISI 1095 STEEL test case

The manifold-based identification protocol proposed in previous chapters was first verified by an axisymmetric indentation test on AISI 1095 steel using a spherical tip indenter with a radius of 0.5 mm. Since the *floating search* method has been verified in Section 5.3, only the identification results obtained by using *panning, zooming* and *panning & zooming* algorithms are presented here while those obtained by *floating search* are provided in Appendix B.

7.2.1 Problem description

A power Hollomon's law is assumed for the isotropic hardening, while the elastic portion follows Hooke's law. The hardening behavior is thus governed by three parameters : E, σ_y

and n. The Young's modulus E is fixed at 210 GPa and Poisson's ratio ν 0.3. The other two parameters : yield stress σ_y and strain hardening exponent n, controlling the plastic properties need to be identified. Even if we already have a general estimate for the properties of the above-mentioned material ($\sigma_y \approx 100$ Mpa, $n \approx 0.3$), the parameters are identified in a rather large design space ($n \in [0.1, 0.5]$, $\sigma_y \in [50\,\text{Mpa}, 400\,\text{Mpa}]$) so as to keep the material point of interest away from the boundaries [5]. This will ensure sufficient accuracy during the inverse analysis and allow us to test the robustness of the proposed methodology.

The same FE model as presented in Figure 4.1 (Section 4.1) is adopted, and the contact interface between the indenter and the specimen was characterized by a Coulomb friction coefficient of 0.1. The indentation force is progressively increased up to a prescribed value ($P_{\max} = 500$ N) and the unloading phase is simulated in one step, resulting in a final imprint shape after spring-back. We remind that the only indentation response used in identification is the non-smooth residual imprint in Figure 7.7.

7.2.2 Results and discussion

Three manifold learning algorithms were used for the resolution of the identification problem in this test case. A quadric polynomial basis (2D), containing 6 monomials, was applied for the construction of the smooth manifold in Equation 3.11. Seven snapshots were chosen in each DOE using Latin Hypercube sampling. These snapshots were then decomposed using POD with a full basis of size 7, giving a set of $\alpha_1, \alpha_2 \cdots \alpha_7$ for each of the 7 snapshots. In this subsection, we have used a full basis without truncation, leading to a 7-*dimensional* shape space. For the purpose of visualization, only the first three coordinates were chosen.

We identify two plastic parameters of the steel in the α-space by using the convergence criterion given in Equation 5.1 or 7.1. Note that this criterion in essence compares the *physical* imprint shape with the simulated one, and is normalized as

$$\varepsilon_1 = \frac{\|\tilde{\boldsymbol{s}}_{\text{exp}} - \boldsymbol{s}(\sigma_y, n)\|}{\|\tilde{\boldsymbol{s}}_{\text{exp}}\|}. \tag{7.3}$$

In order to demonstrate the advantage of using the *adaptive* local imprint-manifold, we have also calculated the error between the imprint shape obtained by simulation using the identified parameters and the *real* experimental data

$$\varepsilon_2 = \frac{\|\boldsymbol{s}_{\text{exp}} - \boldsymbol{s}(\sigma_y, n)\|}{\|\boldsymbol{s}_{\text{exp}}\|}. \tag{7.4}$$

Panning

The iteration history of identification using the *panning* algorithm is given in Table 7.4. The design of experiments is centered around successive sets of σ_y and n. $\Delta\sigma_y$ and Δn are the sizes of the design window. The pattern of exploration of the total design space by *panning* the design window is shown in Figure 7.9. Different symbols are used for odd and even iteration numbers for clearer visualization. For overlapping windows, the snapshots may be reused in order to save computing time.

TABLE 7.4 Iteration results using *panning* approach.

Iter	σ_y	n	$\Delta\sigma_y$	Δn	$\|\boldsymbol{\alpha}_{\text{exp}} - \boldsymbol{\alpha}^*\|$	ε_1	ε_2
1	205.0	0.225	30	0.05	0.0629	8.01%	8.78%
2	190.1	0.226	30	0.05	0.0327	4.15%	5.56%
3	175.1	0.239	30	0.05	0.0292	3.71%	5.16%
4	160.1	0.260	30	0.05	0.0219	2.79%	4.57%
5	145.1	0.275	30	0.05	0.0171	2.18%	4.20%
6	130.2	0.294	30	0.05	0.0118	1.50%	3.88%
7	115.4	0.312	30	0.05	0.0052	0.66%	3.58%
8	104.0	0.330	30	0.05	0.0030	0.38%	3.53%

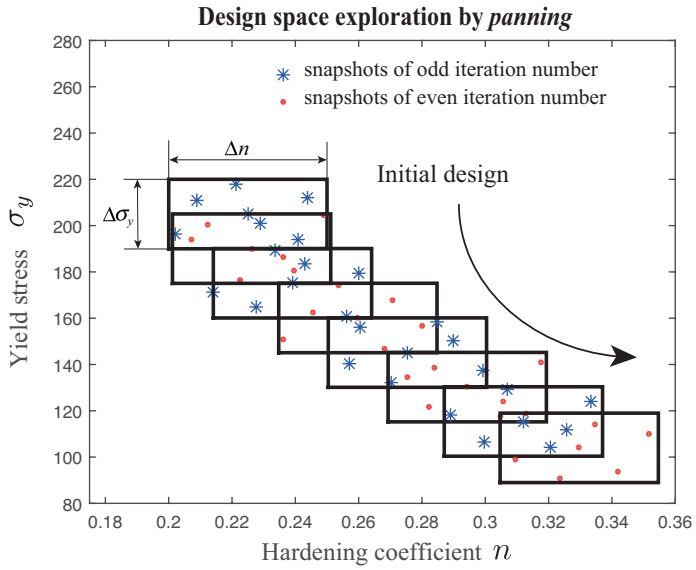

FIGURE 7.9 *Panning* iterations (Table 7.4).

Successive design spaces and corresponding local manifolds are shown in Figure 7.10-7.12. The green diamond, denoting the projection of the experimental imprint in α-space, converges to the center of the local coordinate system, which also implies that the estimated

imprint converges to $\boldsymbol{s}_{\text{exp}}$. The black dot in design space represents the current estimation parameters corresponding to the point on $\mathscr{M}$ closest to the projection of the experimental imprint.

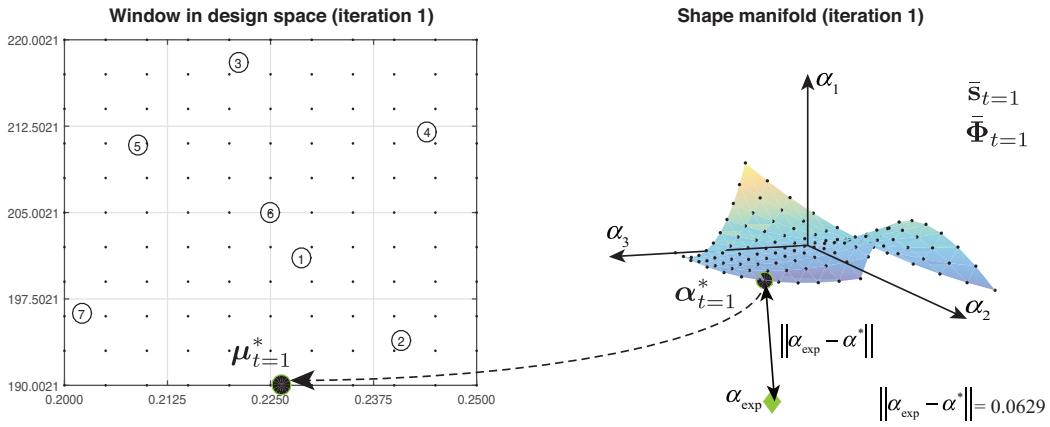

FIGURE 7.10 Material parameters identification procedure by design space and local manifold 1.

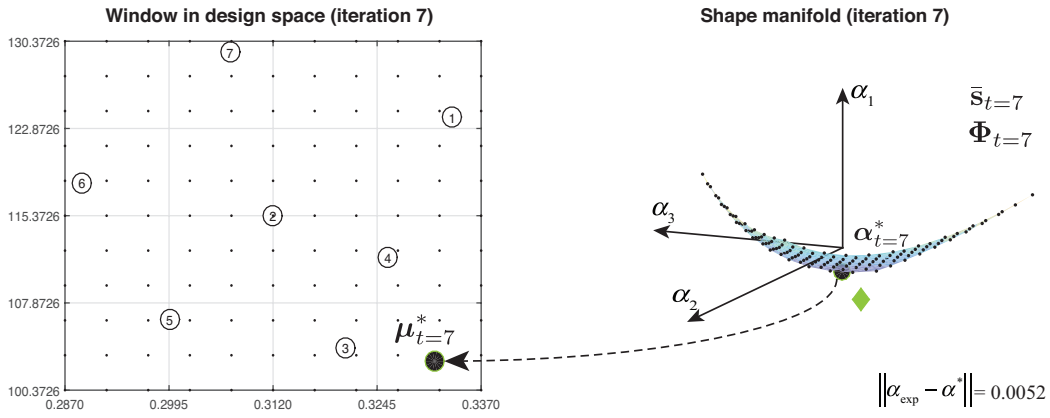

FIGURE 7.11 Material parameters identification procedure by design space and local manifold 7.

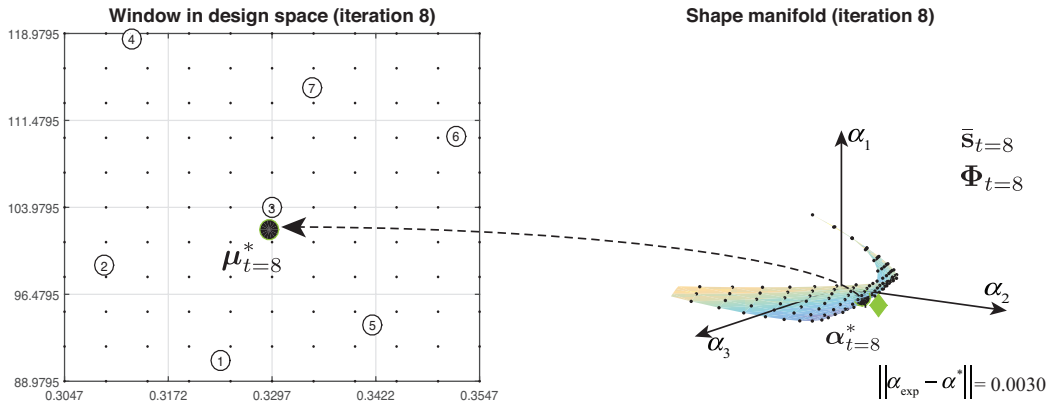

FIGURE 7.12 Material parameters identification procedure by design space and local manifold 8.

The local manifolds in this *panning* method are not accurately approximated for the simple reason that we are using only a *quadric* surface to approximate $\mathscr{M}$ in a relatively wide range($\Delta\sigma_y = 30$ MPa, $\Delta n = 0.05$). With the *panning* method, we can only obtain a general estimate for the material parameters. The accuracy may be improved by either increasing the degree of the polynomial basis or by shrinking the size of the window. Another option is to try to use more snapshots for a more accurate approximation of the local manifold, this will be discussed in Appendix C.5.

Zooming

For this algorithm, the convergence of the material properties is shown in Table 7.5, where σ_y stabilized around 105 MPa and n around 0.326. Clearly, the standard error ε_2 has stabilized at 3.6% after only 3 iteration steps, while the proposed error ε_1 drops to around 1% by using the projected imprint in shape space. Even though the error ε_1 in the 4^{th} iteration is smaller than in the last one, we still prefer the material identified in the last step for the reason that the local manifold is more accurate so we can obtain the projection of the experimental imprint. This last manifold is considered accurate since the identification is carried out in a small window size and the material parameters vary only in a small range : 2.5 MPa for σ_y and 0.002 for n.

The iteration procedure in design space is shown in Figure.7.13. Also, imprint snapshots at various stages and the experimental imprint are compared (Figure 7.14). It is clear that the simulated imprint shapes will concentrate around the experimental one when the local manifold patch decreases in size in subsequent iterations.

TABLE 7.5 Iteration results using regular *zooming* approach.

Iter	σ_y	n	$\Delta\sigma_y$	Δn	$\|\boldsymbol{\alpha}_{\text{exp}} - \boldsymbol{\alpha}^*\|$	ε_1	ε_2
1	250.0	0.250	320	0.3	0.2512	31.97%	32.16%
2	99.79	0.394	160	0.15	0.0155	1.97%	4.25%
3	98.32	0.336	80	0.08	0.0150	1.90%	3.89%
4	98.65	0.331	40	0.04	0.0056	0.71%	3.59%
5	112.44	0.327	20	0.02	0.0147	1.87%	3.57%
6	105.80	0.326	10	0.01	0.0092	1.16%	3.54%
7	105.46	0.326	5	0.005	0.0079	1.01%	3.57%
8	105.79	0.326	2.5	0.002	0.0069	0.87%	3.57%

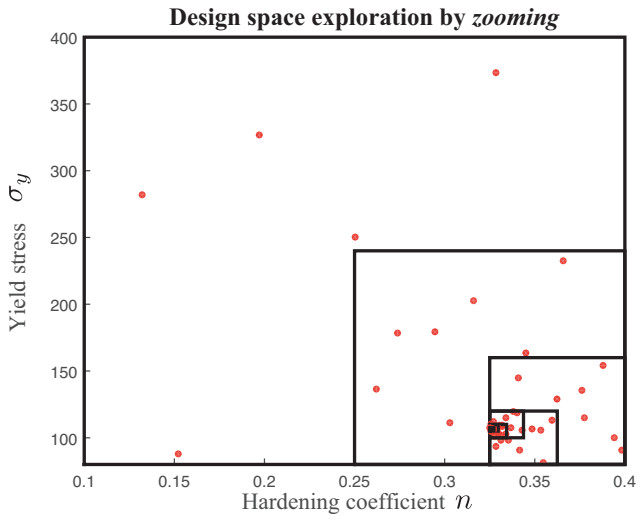

FIGURE 7.13 *Zooming* steps (Table 7.5).

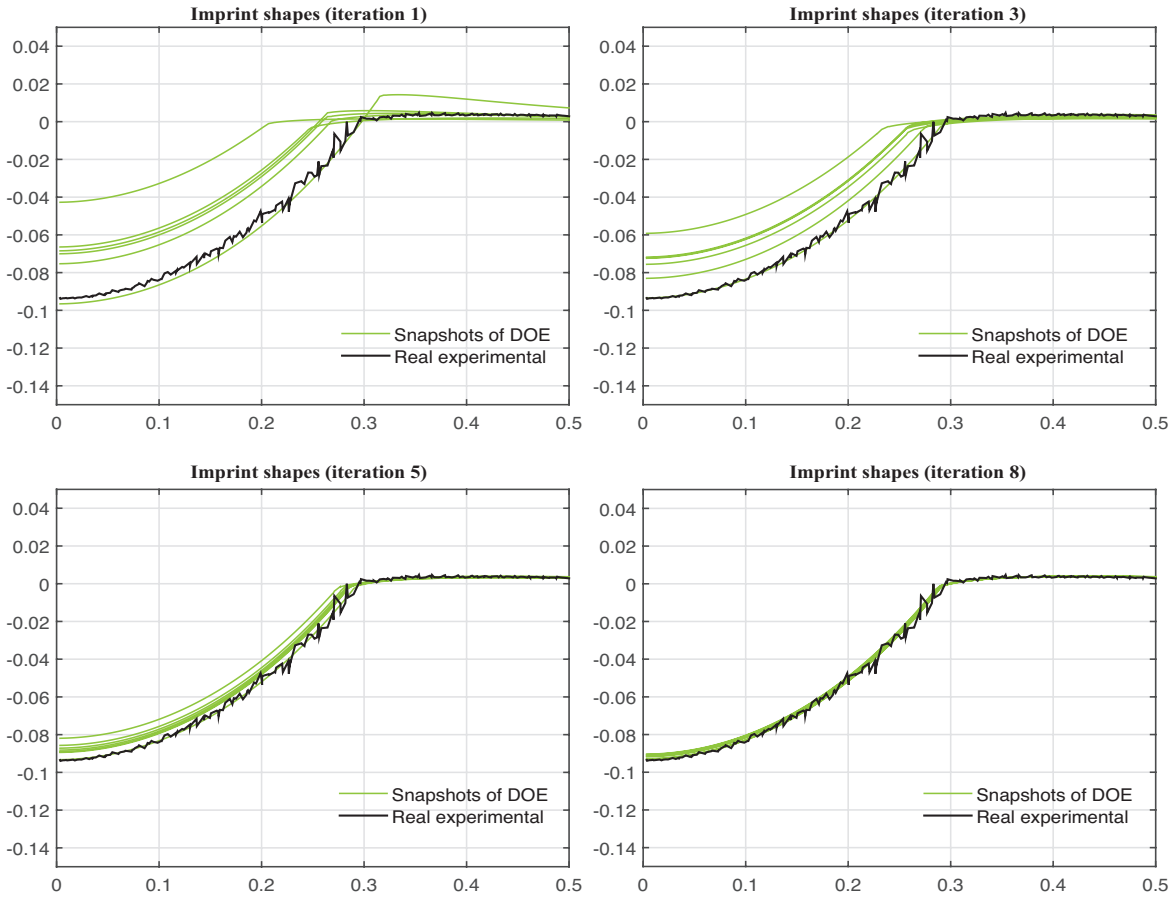

FIGURE 7.14 Experimental imprint and numerical snapshots (*zooming* algorithm).

Panning & *zooming*

Finally, a combined algorithm of *panning* & *zooming* is applied. Similar estimates of the material properties are obtained (Table 7.6). In the first four steps, the *panning* method is introduced to iteratively locate the most promising zone, and during these steps the design window remains of the same size. Next, the *zooming* algorithm is adopted in order to improve the accuracy of the local manifold for better identification. The first searching algorithm is automatically switched to the second one as soon as the estimate for the next iteration is located inside the current window rather than on its boundary. The pattern of exploration in design space is visualized in Figure 7.15.

TABLE 7.6 Iteration results using *panning & zooming*.

Iter	σ_y	n	$\Delta\sigma_y$	Δn	$\|\boldsymbol{\alpha}_{\text{exp}} - \boldsymbol{\alpha}^*\|$	ε_1	ε_2
1	175.0	0.300	40	0.04	0.1989	25.31%	25.56%
2	155.0	0.280	40	0.04	0.0697	8.87%	9.62%
3	135.2	0.287	40	0.04	0.0175	2.22%	3.98 %
4	120.5	0.307	40	0.04	0.0083	1.05%	3.68%
5	107.0	0.326	20	0.02	0.0059	0.75%	3.54%
6	108.0	0.323	10	0.01	0.0121	1.53%	3.57%
7	106.7	0.323	5	0.005	0.0089	1.13%	3.56%
8	107.0	0.324	2.5	0.002	0.0096	1.22%	3.57%

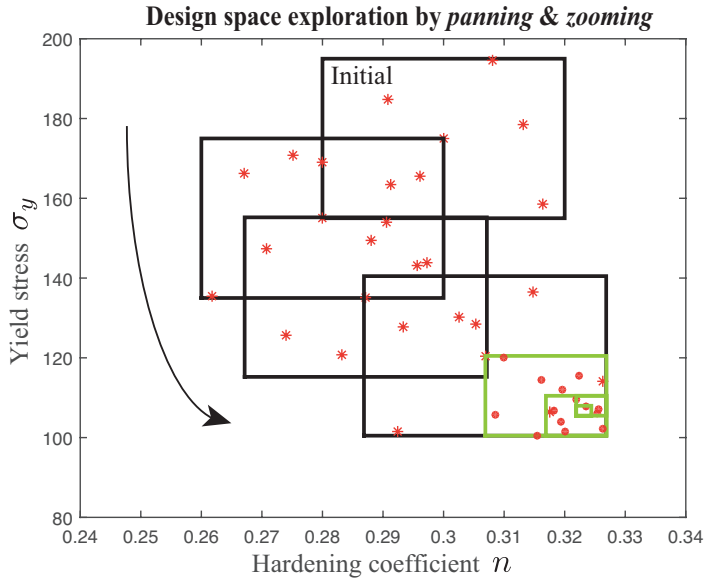

FIGURE 7.15 Combination of *zooming* and *panning* (Table 7.6).

Comparison of the three algorithms

For the purpose of comparison, the convergence patterns of material parameters identified by the three different algorithms are depicted in Figure 7.16. The robustness of the identification procedure in lower-dimensional α-space is confirmed by using different initial points for the three algorithms which lead to almost identical material parameters. In addition, it may also be concluded from the iteration histories that the combined *zooming & panning* approach gives the best convergence for *both* parameters.

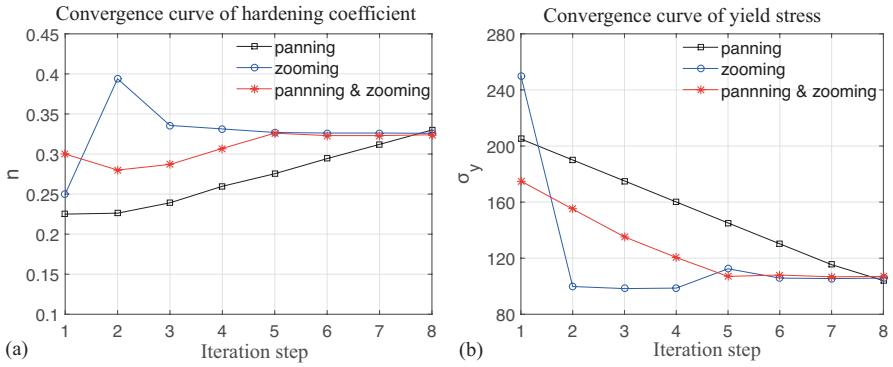

FIGURE 7.16 Convergence patterns for the parametric identification of n and σ_y.

The identification error ε_1 is shown in Figure 7.17. Obvious decreases are observed, that stabilize at around 1%. It bears mentioning that this error is more reliable if the design subspace/window is smaller at each iteration step, which is why the result in the 8^{th} iteration is preferable to that obtained in the 4^{th} iteration in Table.7.5.

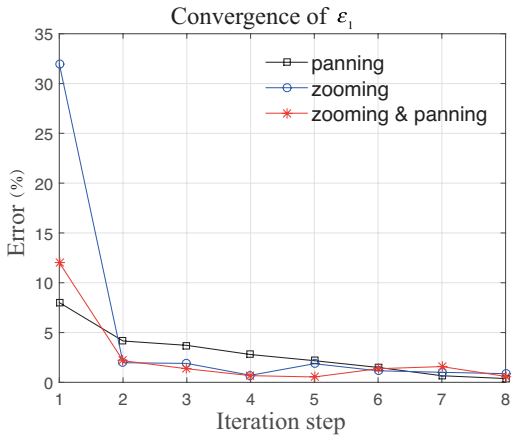

FIGURE 7.17 Progressive reduction of the error estimation ε_1 between the imprint shape obtained with identified parameters and the experimental imprint reconstructed with POD modes.

Other discussions are also made in Appendix C to demonstrate the robustness of these alogorithms with respect to such parameters as the number of retained POD modes, the order of polynomial basis in manifold approximation as well as the number of snapshots.

7.3 SECOND TEST CASE : aluminum alloys

Different from the previous example, the *floating search* algorithm was chosen to characterize the two aluminum alloys : EN AW-2017F and EN AW-5754F. Exactly the same protocol is followed to solve the inverse identification problem within the manifold space.

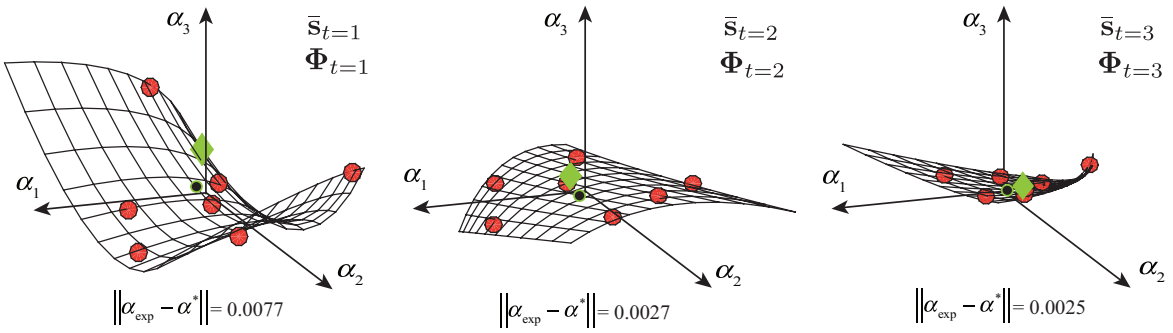

FIGURE 7.18 Local manifold convergence for EN AW-2017F.

In Figure 7.18, we choose the alloy EN AW-2017F to demonstrate the decreases in size of local manifolds along with the iterations, since a shrinking multiplier $\beta = 0.8$ (Algorithm 4) was adopted. As expected, the distance between the experimental imprint (marked with green diamonds) and the estimated admissible imprint on the manifold (represented by a black dot) is minimized. We also note that the new estimate of each iteration converges towards the origin of the coordinate system due to the reason that all the snapshots were centered before POD/SVD. A similar result was also obtained for EN AW-5754F alloys, and thus has been omitted here. The identified power-law parameters are summarized in Table 7.7.

TABLE 7.7 Summary of identified Hollomon's hardening parameters for the two aluminum alloys.

Material	Parameters	Floating search
EN AW-2017F	σ_y	254.8 MPa
	n	0.178
EN AW-5754F	σ_y	83.73 MPa
	n	0.174

The convergence patterns of material parameters identified for the two specimens studied by the proposed floating manifold search algorithm are compared in Figure 7.19. It is fairly clear that floating search approach gives a uniform and steady convergence of *both* plastic parameters.

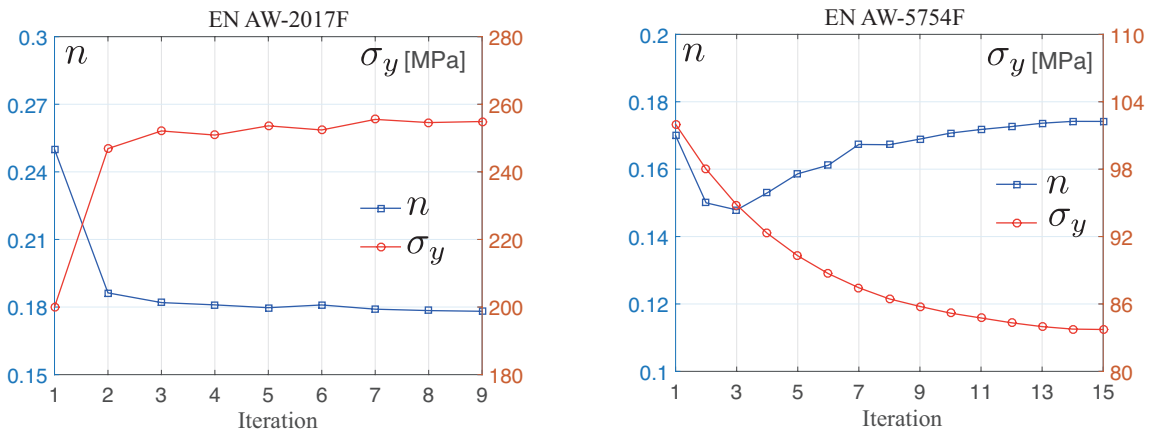

FIGURE 7.19 Convergence patterns for the parametric identification of n and σ_y for for the two aluminum alloys.

7.4 Characterizing three materials with Voce parameters

Thus far, the three hardening materials have been characterized by Hollomon's power law parameters. The imprints simulated with these parameters are in good agreement with the measured ones. However, these identification results are obtained based on the *a priori* assumption that most metallic materials will harden according to (or similar to) the Hollomon's power law, but this may not be the case each and every time we perform an indentation-based identification.

TABLE 7.8 Summary of identified parameters for the three materials considering different hardening behaviors.

Materials	Hollomon's		Voce		
	σ_y (MPa)	n	σ_y (MPa)	Q (MPa)	γ
AISI 1095	107	0.324	128.39	575.04	30
EN AW-2017F	254.8	0.178	274.86	224.74	25.84
EN AW-5754F	83.73	0.174	94.5	122.61	12.71

It is of interest therefore to evaluate materials with different constitutive behaviors. This is in fact a relatively simple matter since conducting the FE simulations using a different law and thus the number of parameters to be identified do not in any way change the implementation of the imprint-based identification protocol.

In this section, the three metallic materials are characterized by three Voce parameters using the residual imprints (Sect.7.1.1). For simplicity sake, only the identified Voce parameters are tabularized in Table 7.8, while the detailed results regarding the local manifold evolutions have been omitted.

7.5 Discussions on the material constitutive behaviors

Other than indentation, tensile testing was also carried out on the three materials to examine the identification results. In view of the homogeneity of the steel specimen, only one tensile test has been performed, while for the two aluminum alloys, their tensile behaviors were studied in three different directions : 0° (Rolling Direction : RD), 45° (Diagonal Direction : DD) and 90° (Transversal Direction : TD). The stress-strain curves for the three materials were measured until the necking phase. With the identified parameter sets in Table 7.8, we "recreate" the tensile curves corresponding to two different constitutive laws for three materials, and compare them with those obtained by uniaxial tensile test in Figures 7.20-7.22. We finally use the averaged tensile curves for the two alloys.

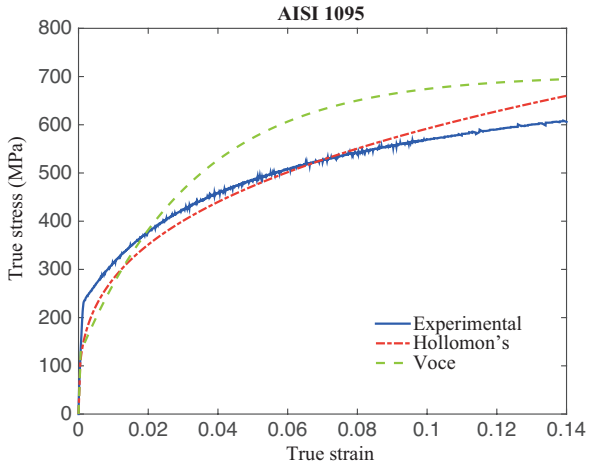

FIGURE 7.20 Comparison of tensile curves for steel AISI 1095.

For AISI 1095, Figure 7.20 indicates that the material appears to harden according to Hollomon's power behavior rather than the Voce law, in view of the less discrepancy between experimental tensile curve (blue line) and that reconstructed from the power law parameters (red dot-dash-line). Despite that, we still observe that the initial elastic limit seems to be underestimated. According to our knowledge of the material, the value between 107 MPa and 128.39 MPa for σ_y is however reasonable.

Similarly, Figure 7.21 suggests that EN-AW 5754F can be considered as a Voce material. Moreover, in view of the rather limited discrepancy with the curves identified from Hollomon's law, we consider that this material can also be characterized with power law hardening parameters. In fact, this observation is in a good accordance with that we have drawn from the global manifold in Sect.3.4.3 concerning materials that could be characterized by either law.

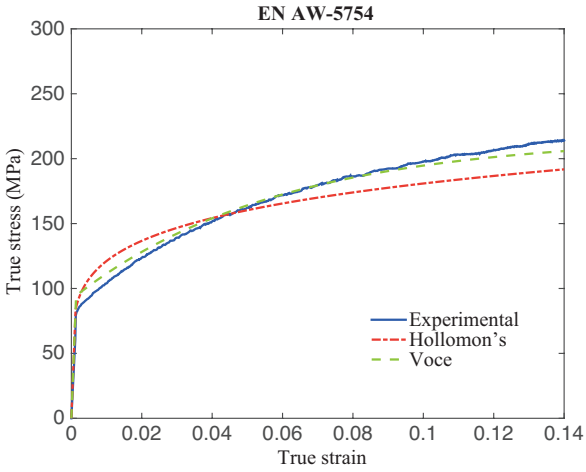

FIGURE 7.21 Comparison of tensile curves for EN AW-5754F alloy

For EN-AW 2017F characterized by both material laws, Figure 7.22 shows an obvious gap between the reconstructed and the experimental tensile curves, despite the fact that both simulated imprints correspond well to the experimental ones at convergence. We may be tempted to chalk this up to the indentation size effect (ISE) and the heterogeneity of the specimen. However, if we revisit (in Figure 7.3) the microstructures of the studied material and estimate the size of the heterogeneities ($<$ 10 microns) with respect to the radius of the indenter (0.5 mm) or even with the size of the imprints obtained, we see that the ratio is very low, allowing us to assume an almost homogeneous specimen.

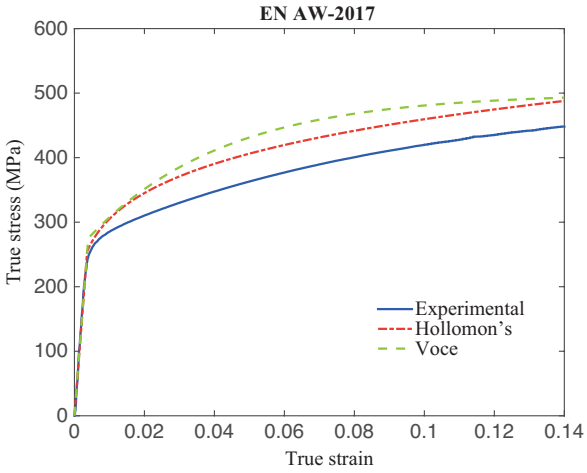

FIGURE 7.22 Comparison of tensile curves for EN AW-2017F alloy

Basically, we must remember that tensile testing is a more "global" method while indentation is a "local" method. Even if the microstructure appears to be homogenous, we could have a non-uniform evolution of residual stresses *ergo* hardening behavior, and indentation

at different points will (as is usually the case) give different results. In addition, the material itself may not necessarily be homogenous and isotropic, and may or may not follow an isotropic hardening, not to mention that there is no guarantee that the hardening laws are valid for the materials chosen. With these considerations in mind, we can rarely rebuild, with the indentation-based identification parameters, the *exact* same tensile curves as the experimental ones. Thereby, the material parameters identified in this section are acceptable.

7.6 Closing remarks

In this chapter, the manifold-based protocol for the identification of material work hardening properties has been verified for three metallic materials, using only the imprint shapes obtained after spherical indentation. Satisfactory results are obtained using a variety of algorithms. The proposed manifold method allows us to directly compare the imprints obtained by FE simulation (in the inverse analysis) with those obtained by actual indentation on the sample specimens.

Almost identical power law work hardening parameter sets (σ_y, n) are obtained with different algorithms even when starting from very different initial points for all tested materials. This may suggest that the residual imprint alone guarantees the uniqueness of inverse solution. We have also addressed that the non-smooth measurements were employed directly in the developed method, since the constructed α-manifold provides us with a natural/physics-based way of smoothing the imprint data of a real experiment. This smoothing is based on the modes that capture the intrinsic features of imprint shapes governed by a given constitutive law.

In addition, with the same imprints, the identification protocol was also applied to calibrate a more complex constitutive law, i.e., the Voce hardening law, since the order of the material law and thus the number of parameters to be identified do not in any way change the application of the protocol. The convergence of the imprints illustrating that two materials with different constitutive laws may lead to almost identical imprints after the withdrawal of indenter. By comparison with the corresponding tensile curves obtained for the three materials, we underline that the AISI 1095 behaves closer to the power law, while EN AW-2017 appears to be a Voce material.

Chapitre 8

Conclusions and Perspectives

In this thesis, we have made a first attempt to fuse the fields of computer science, namely dimensionality reduction and manifold learning, with the field of computational materials science and mechanics so as to meet the latter's urgent requirement of data analysis methods. The focus is on reducing/projecting massive data, collected from either FE simulations or advanced measurements, into a lower-dimensional space, in which an engineering problem can be solved straightforwardly, or a better understanding of complex phenomena is readily obtained. The work presented in this thesis spreads from methodology development to engineering applications.

With respect to methodologies, we have clarified in Chapter 3, based on general shapes within the context of computational mechanics, some basic concepts involved in the shape-manifold. Having a special interest in inverse identification, we developed non-linear shape-manifold learning protocols which are broadly applicable also to several other engineering problems, e.g., shape optimization and design of deep drawing. With regards to different features of the problem at hand, the dimensionality reduction algorithms reviewed in Section 2.1.2 may be implemented to the developed manifold protocol. In contrast with conventional methods, the manifold technique allows the automatic detection of data's underlying structure. To avoid prohibitively high computational investment, we have also proposed a series of local algorithms which tackle the same problem for moderate computational expense.

The developed methodology is then verified in Chapter 4 for an inverse identification problem based on a variety of indentation responses. The interests of the proposed methodology are first validated using synthetic noise-free data. Moreover, the well-known "mystical material" (w.r.t. the *P-h* curve) concerning the non-unicity of inverse identification of Hollomon's parameter is easily visualized in view of the correlation between the number of identifiable parameters and the intrinsic dimensionality of the manifold. This insight in turn suggests that we employ a *"prescribed-displacement"* boundary condition in simulation to formulate a

well-posed inverse problem, and to mitigate the mystical siblings by considering the residual imprint.

In pursuit of more general validation, in Chapter 5 we have extended the manifold approach to the identification of material hardening parameters according to the Voce law. The proposed method enables us to observe the non-unique solutions in parametric space, which has been rarely reported in the available literature. This non-unicity is then throughly investigated in Chapter 6, and in contrast to mystical material pairs w.r.t. Hollomon's law we have differentiated *two* groups of indistinguishable materials, i.e., the *"true"* and *"false"* pairs, with the aid of a criterion, "goodness of fit". Again, by observing the solutions within the reduced imprint-shape space, we discover that the presence of false mystical siblings is partly due to the parametrization of the constitutive law, and partly due to the inadequacy of indentation in capturing certain material properties (γ). That being said, we can still exclude the true mystical materials by using the multi-depth technique. Further verification on experimental indentation imprint is provided in Chapter 7 .

In this thesis, the application to the indentation-based identification problem may serve primarily to target the dissemination of manifold learning approach in the field of computational mechanics. To our best knowledge, this merging of computational mechanics and machine learning methods is a relatively new field which deserves more research interest. In the following, we provide our perspectives on potential extensions based on the proposed paradigms on this thesis :

— In the current work, the low-dimensional embedding of raw data is "discovered" by using PCA or MDS, both are essentially linear methods. From a methodological point of view, further comparison should be done with nonlinear manifold methods, like ISOMAP and Locally Linear Embedding. The geodesic distance, though introduced in Section 2.1 has not yet been adopted to formulate the cost function for minimization problem. Therefore, there is a necessity to integrate it in the global manifold.

— As can be observed from Figure 7.9-7.13, any local-manifold algorithm exploits the entire design space in such a manner that overlaps are observed for successive local design spaces. Therefore, the local manifold learning algorithms could (and should) be improved in order to "reuse" the snapshots when they are situated in the design windows of the incoming iterations. Generally, two possible strategies may be adopted : the first is to retain the same number of snapshots per iteration and to reuse these from the *previous* iteration steps to yield a significant reduction in computation time ; or the precedent snapshots fallen into *current* local space could be used as supplementary information to improve the accuracy of the current local-manifold approximation.

— In addition to indentation imprint/*P*-*h* curve, other potential measurements from testings like vibration testing and Digital Image Correlation could potentially be attempted. Work on these applications as well as refining the application to material characterization, in addition to improving the algorithms themselves, will constitute another research area in the near future.

Bibliographie

[1] Alcala, J., Barone, A., and Anglada, M. (2000). The influence of plastic hardening on surface deformation modes around vickers and spherical indents. *Acta Materialia*, 48(13) :3451 – 3464.

[2] Alkorta, J., Martinez-Esnaola, J., and Sevillano, J. G. (2005). Absence of one-to-one correspondence between elastoplastic properties and sharp-indentation load–penetration data. *Journal of materials research*, 20(02) :432–437.

[3] Allaire, G., Jouve, F., and Toader, A.-M. (2004). Structural optimization using sensitivity analysis and a level-set method. *Journal of Computational Physics*, 194(1) :363–393.

[4] Amanieu, H.-Y., Rosato, D., Sebastiani, M., Massimi, F., and Lupascu, D. C. (2014). Mechanical property measurements of heterogeneous materials by selective nanoindentation : Application to limn 2 o 4 cathode. *Materials Science and Engineering : A*, 593 :92–102.

[5] Ashby, M. F. and Cebon, D. (1993). Materials selection in mechanical design. *Le Journal de Physique IV*, 3(C7) :C7–1.

[6] Audouze, C., De Vuyst, F., and Nair, P. (2009). Reduced-order modeling of parameterized PDEs using time-space-parameter principal component analysis. *International Journal for Numerical Methods in Engineering*, 80(8) :1025 – 1057.

[7] Balasubramanian, M. and Schwartz, E. L. (2002). The isomap algorithm and topological stability. *Science*, 295(5552) :7–7.

[8] Bartier, O., Hernot, X., and Mauvoisin, G. (2010). Theoretical and experimental analysis of contact radius for spherical indentation. *Mechanics of Materials*, 42(6) :640 – 656.

[9] Benamara, T., Breitkopf, P., Lepot, I., and Sainvitu, C. (2016). Adaptive infill sampling criterion for multi-fidelity optimization based on gappy-pod. *Structural and Multidisciplinary Optimization*, 54(4) :843–855.

[10] Berkooz, G., Holmes, P., and Lumley, J. L. (1993). The proper orthogonal decomposition in the analysis of turbulent flows. *Annu Rev Fluid Mech*, 25(1) :539–575.

[11] Bocciarelli, M. and Bolzon, G. (2007). Indentation and imprint mapping for the identification of constitutive parameters of thin layers on substrate : perfectly bonded interfaces. *Materials Science and Engineering : A*, 448(1) :303–314.

[12] Bocciarelli, M., Bolzon, G., and Maier, G. (2005). Parameter identification in anisotropic elastoplasticity by indentation and imprint mapping. *Mechanics of Materials*, 37(8) :855–868.

[13] Bocciarelli, M., Buljak, V., Moy, C., Ringer, S., and Ranzi, G. (2014). An inverse analysis approach based on a {POD} direct model for the mechanical characterization of metallic materials. *Computational Materials Science*, 95(0) :302 – 308.

[14] Bocciarelli, M. and Maier, G. (2007). Indentation and imprint mapping method for identification of residual stresses. *Computational Materials Science*, 39(2) :381–392.

[15] Bolzon, G., Maier, G., and Panico, M. (2004). Material model calibration by indentation, imprint mapping and inverse analysis. *International Journal of Solids and Structures*, 41(11) :2957–2975.

[16] Bouzakis, K.-D., Michailidis, N., Hadjiyiannis, S., Skordaris, G., and Erkens, G. (2002). The effect of specimen roughness and indenter tip geometry on the determination accuracy of thin hard coatings stress–strain laws by nanoindentation. *Materials characterization*, 49(2) :149–156.

[17] Brammer, P., Bartier, O., Hernot, X., Mauvoisin, G., and Sablin, S.-S. (2012). An alternative to the determination of the effective zero point in instrumented indentation : use of the slope of the indentation curve at indentation load values. *Materials & Design*, 40 :356–363.

[18] Breitkopf, P. and Kleiber, M. (1987). Knowledge engineering enhancement of finite element analysis. *Communications in applied numerical methods*, 3(5) :359–366.

[19] Breitkopf, P., Naceur, H., Rassineux, A., and Villon, P. (2005a). Moving least squares response surface approximation : Formulation and metal forming applications. *Computers and Structures*, 83(17-18) :1411–1428.

[20] Breitkopf, P., Naceur, H., Rassineux, A., and Villon, P. (2005b). Moving least squares response surface approximation : formulation and metal forming applications. *Computers & Structures*, 83(17) :1411–1428.

[21] Breitkopf, P., Rassineux, A., and Villon, P. (2002). An introduction to moving least squares meshfree methods. *Revue Europeenne des Elements*, 11(7-8) :825–867.

[22] Bressan, J., Tramontin, A., and Rosa, C. (2005). Modeling of nanoindentation of bulk and thin film by finite element method. *Wear*, 258(1) :115–122.

[23] Bucaille, J.-L., Stauss, S., Felder, E., and Michler, J. (2003). Determination of plastic properties of metals by instrumented indentation using different sharp indenters. *Acta materialia*, 51(6) :1663–1678.

[24] Buljak, V. and Maier, G. (2011). Proper orthogonal decomposition and radial basis functions in material characterization based on instrumented indentation. *Engineering Structures*, 33(2) :492–501.

[25] Camastra, F. (2003). Data dimensionality estimation methods : a survey. *Pattern recognition*, 36(12) :2945–2954.

[26] Cao, Y. and Huber, N. (2006). Further investigation on the definition of the representative strain in conical indentation. *Journal of materials research*, 21(07) :1810–1821.

[27] Cao, Y. P. and Lu, J. (2004a). Depth-sensing instrumented indentation with dual sharp indenters : stability analysis and corresponding regularization schemes. *Acta Materialia*, 52(5) :1143–1153.

[28] Cao, Y. P. and Lu, J. (2004b). A new method to extract the plastic properties of metal materials from an instrumented spherical indentation loading curve. *Acta materialia*, 52(13) :4023–4032.

[29] Capehart, T. and Cheng, Y. (2003). Determining constitutive models from conical indentation : Sensitivity analysis. *Journal of materials research*, 18(04) :827–832.

[30] Castanier, M. P., Ottarsson, G., and Pierre, C. (1997). A reduced order modeling technique for mistuned bladed disks. *Journal of Vibration and Acoustics*, 119(3) :439–447.

[31] Ceruti, C., Bassis, S., Rozza, A., Lombardi, G., Casiraghi, E., and Campadelli, P. (2014). Danco : An intrinsic dimensionality estimator exploiting angle and norm concentration. *Pattern recognition*, 47(8) :2569–2581.

[32] Chen, X., Ogasawara, N., Zhao, M., and Chiba, N. (2007). On the uniqueness of measuring elastoplastic properties from indentation : the indistinguishable mystical materials. *Journal of the Mechanics and Physics of Solids*, 55(8) :1618–1660.

[33] Chen, X. and Vlassak, J. J. (2001). Numerical study on the measurement of thin film mechanical properties by means of nanoindentation. *Journal of Materials Research*, 16(10) :2974–2982.

[34] Cheng, Y.-T. and Cheng, C.-M. (1999). Can stress–strain relationships be obtained from indentation curves using conical and pyramidal indenters ? *Journal of Materials Research*, 14(09) :3493–3496.

[35] Chinesta, F., Ammar, A., and Cueto, E. (2010). Proper generalized decomposition of multiscale models. *International Journal for Numerical Methods in Engineering*, 83(8-9) :1114–1132.

[36] Chinesta, F., Ladeveze, P., and Cueto, E. (2011). A short review on model order reduction based on proper generalized decomposition. *ARCHIVES OF COMPUTATIONAL METHODS IN ENGINEERING*, 18(4) :395–404.

[37] Chollacoop, N., Dao, M., and Suresh, S. (2003). Depth-sensing instrumented indentation with dual sharp indenters. *Acta materialia*, 51(13) :3713–3729.

[38] Collin, J.-M., Mauvoisin, G., Bartier, O., Abdi, R. E., and Pilvin, P. (2009). Experimental evaluation of the stress-strain curve by continuous indentation using different indenter shapes. *Materials Science and Engineering : A*, 501(1-2) :140–145.

[39] Constantinides, G., Ulm, F.-J., and Van Vliet, K. (2003). On the use of nanoindentation for cementitious materials. *Materials and Structures*, 36(3) :191–196.

[40] Cooreman, S., Lecompte, D., Sol, H., Vantomme, J., and Debruyne, D. (2008). Identification of mechanical material behavior through inverse modeling and dic. *Experimental Mechanics*, 48(4) :421–433.

[41] Cordier, L., El Majd, B. A., and Favier, J. (2010). Calibration of pod reduced order models using tikhonov regularization. *International Journal for Numerical Methods in Fluids*, 63(2) :269–296.

[42] Cortes, C. and Vapnik, V. (1995). Support vector machine. *Machine learning*, 20(3) :273–297.

[43] Cox, T. F. and Cox, M. A. (2000). *Multidimensional scaling*. CRC press.

[44] Dao, M., Chollacoop, N. v., Van Vliet, K., Venkatesh, T., and Suresh, S. (2001). Computational modeling of the forward and reverse problems in instrumented sharp indentation. *Acta materialia*, 49(19) :3899–3918.

[45] Dean, J. and Clyne, T. (2016). Extraction of plasticity parameters from a single test using a spherical indenter and fem modelling. *Mechanics of Materials*.

[46] Dean, J. and Clyne, T. (2017). Extraction of plasticity parameters from a single test using a spherical indenter and fem modelling. *Mechanics of Materials*, 105 :112–122.

[47] Duvigneau, R. (2006a). Adaptive parameterization using free-form deformation for aerodynamic shape optimization.

[48] Duvigneau, R. (2006b). Adaptive parameterization using free-form deformation for aerodynamic shape optimization. *INRIA Research Report RR-5949*.

[49] Forrester, A. I. J. and Keane, A. J. (2009). Recent advances in surrogate-based optimization. *Progress in Aerospace Sciences*, 45 :50–79.

[50] Freund, Y. and Mason, L. (1999). The alternating decision tree learning algorithm. In *icml*, volume 99, pages 124–133.

[51] Friedman, J. H. (1987). Exploratory projection pursuit. *Journal of the American statistical association*, 82(397) :249–266.

[52] Furey, T. S., Cristianini, N., Duffy, N., Bednarski, D. W., Schummer, M., and Haussler, D. (2000). Support vector machine classification and validation of cancer tissue samples using microarray expression data. *Bioinformatics*, 16(10) :906–914.

[53] Futakawa, M., Wakui, T., Tanabe, Y., and Ioka, I. (2001). Identification of the constitutive equation by the indentation technique using plural indenters with different apex angles. *Journal of Materials Research*, 16(08) :2283–2292.

[54] Ganneau, F., Constantinides, G., and Ulm, F.-J. (2006). Dual-indentation technique for the assessment of strength properties of cohesive-frictional materials. *International journal of solids and structures*, 43(6) :1727–1745.

[55] Ghnatios, C., Chinesta, F., Cueto, E., Leygue, A., Breitkopf, P., and Villon, P. (2011). Methodological approach to efficient modeling and optimization of thermal processes taking place in a die : Application to pultrusion. *Composites Part A*, 42 :1169–1178.

[56] Ghnatios, C., Masson, F., Huerta, A., Cueto, E., Leygue, A., and Chinesta, F. (2012). Proper generalized decomposition based dynamic data-driven control of thermal processes. *Computer Methods in Applied Mechanics and Engineering*, 213 :29–41.

[57] Giannakopoulos, A. and Suresh, S. (1999a). Determination of elastoplastic properties by instrumented sharp indentation. *Scripta materialia*, 40(10) :1191–1198.

[58] Giannakopoulos, A. and Suresh, S. (1999b). Theory of indentation of piezoelectric materials. *Acta materialia*, 47(7) :2153–2164.

[59] Gibson, R. F. (2014). A review of recent research on nanoindentation of polymer composites and their constituents. *Composites Science and Technology*, 105 :51–65.

[60] Goldberg, D. E. and Holland, J. H. (1988). Genetic algorithms and machine learning. *Machine learning*, 3(2) :95–99.

[61] Golub, G. H. and Reinsch, C. (1970). Singular value decomposition and least squares solutions. *Numerische mathematik*, 14(5) :403–420.

[62] Gonzalez, D., Cueto, E., and Chinesta, F. (2015). Computational patient avatars for surgery planning. *Annals of Biomedical Engineering*, pages 1–11.

[63] Grau, P., Berg, G., Fraenzel, W., and Meinhard, H. (1994). Recording hardness testing. problems of measurement at small indentation depths. *physica status solidi (a)*, 146(1) :537–548.

[64] Grediac, M. (2004). The use of full-field measurement methods in composite material characterization : interest and limitations. *Composites Part A : applied science and manufacturing*, 35(7) :751–761.

[65] Hagan, M. T., Demuth, H. B., Beale, M. H., and De Jesús, O. (1996). *Neural network design*, volume 20. PWS publishing company Boston.

[66] Hanche-Olsen, H. (2004). Buckingham ?s pi-theorem. *NTNU : http ://www. math. ntnu. no/˜ hanche/notes/buckingham/buckingham-a4. pdf*.

[67] Hastie, T. and Stuetzle, W. (1989). Principal curves. *Journal of the American Statistical Association*, 84(406) :502–516.

[68] Hoang, K., Kerfriden, P., and Bordas, S. (2016). A fast, certified and "tuning free" two-field reduced basis method for the metamodelling of affinely-parametrised elasticity problems. *Computer Methods in Applied Mechanics and Engineering*, 298 :121–158.

[69] Hou, Y., Sapanathan, T., Dumon, A., Culière, P., and Rachik, M. (2016). A novel artificial dual-phase microstructure generator based on topology optimization. *Computational Materials Science*, 123 :188–200.

[70] Hurtado, J. E. (2013). *Structural reliability : statistical learning perspectives*, volume 17. Springer Science & Business Media.

[71] Ito, K. and Ravindran, S. (1998). A reduced-order method for simulation and control of fluid flows. *Journal of computational physics*, 143(2) :403–425.

[72] J. Toal, D. J. and Keane, A. J. (2011). Efficient multipoint aerodynamic design optimization via cokriging. *Journal of Aircraft*, 48(5) :1685–1695.

[73] Jin, H. and Lloyd, D. (2004). The tensile response of a fine-grained aa5754 alloy produced by asymmetric rolling and annealing. *Metallurgical and Materials Transactions A*, 35(13) :997–1006.

[74] Johnson, K. L. and Johnson, K. L. (1987). *Contact mechanics*. Cambridge university press.

[75] Johnson, W., Mahtab, F., and Williams, A. (1965). Experiments concerning geometric similarity in indentation. *International Journal of Mechanical Sciences*, 7(6) :389–398.

[76] Jolliffe, I. (2002). *Principal component analysis*. Wiley Online Library.

[77] Kamali-Bernard, S., Keinde, D., and Bernard, F. (2014). Effect of aggregate type on the concrete matrix/aggregates interface and its influence on the overall mechanical behavior. a numerical study. *Key Engineering Materials*, 617 :14 – 17.

[78] Kang, S.-K., Kim, Y.-C., Lee, Y.-H., Kim, J.-Y., and Kwon, D. (2012). Determining effective radius and frame compliance in spherical nanoindentation. *Materials Science and Engineering : A*, 538(0) :58 – 62.

[79] Kumar, V., Grama, A., Gupta, A., and Karypis, G. (1994). *Introduction to parallel computing : design and analysis of algorithms*, volume 400. Benjamin/Cummings Redwood City, CA.

[80] Langley, P. (2011). The changing science of machine learning. *Machine Learning*, 82(3) :275–279.

[81] Le Quilliec, G., Raghavan, B., and Breitkopf, P. (2015). A manifold learning-based reduced order model for springback shape characterization and optimization in sheet metal forming. *Computer Methods in Applied Mechanics and Engineering*, 285 :621–638.

[82] Legrain, G., Cartraud, P., Perreard, I., and Moes, N. (2011). An x-fem and level set computational approach for image-based modelling : Application to homogenization. *International Journal for Numerical Methods in Engineering*, 86(7) :915–934.

[83] Li, N., Tahar, M. B., Aboura, Z., and Khellil, K. (2016). A dynamic analysis approach for identifying the elastic properties of unstitched and stitched composite plates. *Composite Structures*, 152 :959–968.

[84] Lichinchi, M., Lenardi, C., Haupt, J., and Vitali, R. (1998). Simulation of berkovich nanoindentation experiments on thin films using finite element method. *Thin solid films*, 312(1) :240–248.

[85] Lopez, E., Gonzalez, D., Aguado, J., Abisset-Chavanne, E., Cueto, E., Binetruy, C., and Chinesta, F. (2016). A manifold learning approach for integrated computational materials engineering. *Archives of Computational Methods in Engineering*, pages 1–10.

[86] Love, A. (1939). Boussinesq's problem for a rigid cone. *The Quarterly Journal of Mathematics*, (1) :161–175.

[87] Lu, Y. and Shinozaki, D. (2005). Effects of substrate constraint on micro-indentation testing of polymer coatings. *Materials Science and Engineering : A*, 396(1–2) :77 – 86.

[88] Lucia, D. J., Beran, P. S., and Silva, W. A. (2004). Reduced-order modeling : new approaches for computational physics. *Progress in Aerospace Sciences*, 40(1) :51–117.

[89] Marteau, J., Bouvier, S., and Bigerelle, M. (2014). Review on numerical modeling of instrumented indentation tests for elastoplastic material behavior identification. *Archives of Computational Methods in Engineering*, pages 1–17.

[90] Matsuda, K. (2002). Prediction of stress-strain curves of elastic-plastic materials based on the vickers indentation. *Philosophical Magazine A*, 82(10) :1941–1951.

[91] Meng, L., Breitkopf, P., and Le Quilliec, G. (2017a). An insight into the identifiability of material properties by instrumented indentation test using manifold approach based on ph curve and imprint shape. *International Journal of Solids and Structures*, 106 :13–26.

[92] Meng, L., Breitkopf, P., Le Quilliec, G., Raghavan, B., and Villon, P. (2016). Nonlinear shape-manifold learning approach : Concepts, tools and applications. *Archives of Computational Methods in Engineering*, pages 1–21.

[93] Meng, L., Breitkopf, P., Raghavan, B., Mauvoisin, G., Bartier, O., and Hernot, X. (2015a). Identification of material properties using indentation test and shape manifold learning approach. *Computer Methods in Applied Mechanics and Engineering*, pages –.

[94] Meng, L., Breitkopf, P., Raghavan, B., Mauvoisin, G., Bartier, O., and Hernot, X. (2015b). Identification of material properties using indentation test and shape manifold learning approach. *Computer Methods in Applied Mechanics and Engineering*, 297 :239–257.

[95] Meng, L., Raghavan, B., Bartier, O., Hernot, X., Mauvoisin, G., and Breitkopf, P. (2017b). An objective meta-modeling approach for indentation-based material characterization. *Mechanics of Materials*, 107 :31–44.

[96] Meng, L., Zhang, W.-H., Zhu, J.-H., Xu, Z., and Cai, S.-H. (2015c). Shape optimization of axisymmetric solids with the finite cell method using a fixed grid. *Acta Mechanica Sinica*, pages 1–15.

[97] Millan, D., Rosolen, A., and Arroyo, M. (2013a). Nonlinear manifold learning for meshfree finite deformation thin-shell analysis. *International Journal for Numerical Methods in Engineering*, 93(7) :685–713.

[98] Millan, D., Rosolen, A., and Arroyo, M. (2013b). Nonlinear manifold learning for model reduction in finite elastodynamics. *Computer Methods in Applied Mechanics and Engineering*, 261-262(7) :181–131.

[99] Minsky, M. (1961). Steps toward artificial intelligence. *Proceedings of the IRE*, 49(1) :8–30.

[100] Moes, N., Stolz, C., Bernard, P. ., and Chevaugeon, N. (2011). A level set based model for damage growth : The thick level set approach. *International Journal for Numerical Methods in Engineering*, 86(3) :358–380.

[101] Montgomery, D. C., Peck, E. A., and Vining, G. G. (2006). Introduction to linear regression. *Wiley, New Jersey*.

[102] Mott, B. W. (1956). *Micro-indentation hardness testing*. Butterworths Scientific Publications.

[103] Moussa, C., Bartier, O., Mauvoisin, G., Hernot, X., Collin, J.-M., and Delattre, G. (2014a). Experimental and numerical investigation on carbonitrided steel characterization with spherical indentation. *Surface and Coatings Technology*, 258(0) :782 – 789.

[104] Moussa, C., Hernot, X., Bartier, O., Delattre, G., and Mauvoisin, G. (2014b). Identification of the hardening law of materials with spherical indentation using the average representative strain for several penetration depths. *Materials Science and Engineering : A*, 606 :409–416.

[105] Moy, C., Bocciarelli, M., Ringer, S., and Ranzi, G. (2011a). Indentation and imprint mapping for the identification of material properties in multi-layered systems. *Computational Materials Science*, 50(5) :1681 – 1691.

[106] Moy, C. K., Bocciarelli, M., Ringer, S. P., and Ranzi, G. (2011b). Identification of the material properties of al 2024 alloy by means of inverse analysis and indentation tests. *Materials Science and Engineering : A*, 529 :119–130.

[107] Mukhopadhyay, A. (1999). Comparative study of indentation fatigue in structural ceramics. *Journal of Materials Science Letters*, 18(4) :333–337.

[108] Mukhopadhyay, A., Datta, S., and Chakraborty, D. (1990). On the microhardness of silicon nitride and sialon ceramics. *Journal of the European Ceramic Society*, 6(5) :303 – 311.

[109] Mulford, R., Asaro, R. J., and Sebring, R. J. (2004). Spherical indentation of ductile power law materials. *Journal of Materials Research*, 19 :2641–2649.

[110] Murat, F. and Simon, J. (1976). Sur le controle par un domaine geometrique. *Prepublication du Laboratoire d'Analyse Numerique, no 76015, Universite de Paris*, 6.

[111] Nakamura, T., Wang, T., and Sampath, S. (2000). Determination of properties of graded materials by inverse analysis and instrumented indentation. *Acta Materialia*, 48(17) :4293–4306.

[112] Oliver, W. C. and Pharr, G. M. (1992). An improved technique for determining hardness and elastic modulus using load and displacement sensing indentation experiments. *Journal of materials research*, 7(06) :1564–1583.

[113] Oliver, W. C. and Pharr, G. M. (2004). Measurement of hardness and elastic modulus by instrumented indentation : Advances in understanding and refinements to methodology. *Journal of materials research*, 19(01) :3–20.

[114] Oshier, S. and Sethian, J. A. (1988). Fronts propagating with curvature-dependent speed : Algorithms based on hamilton-jacobi formulations. *Journal of Computational Physics*, 79 :12–49.

[115] Paietta, R. C., Campbell, S. E., and Ferguson, V. L. (2011). Influences of spherical tip radius, contact depth, and contact area on nanoindentation properties of bone. *Journal of biomechanics*, 44(2) :285–290.

[116] Peterson, J. S. (1989). The reduced basis method for incompressible viscous flow calculations. *SIAM Journal on Scientific and Statistical Computing*, 10(4) :777–786.

[117] Pop, O., Meite, M., Dubois, F., and Absi, J. (2011). Identification algorithm for fracture parameters by combining dic and fem approaches. *International journal of fracture*, 170(2) :101–114.

[118] Raghavan, B., Breitkopf, P., Tourbier, Y., and Villon, P. (2013a). Towards a space reduction approach for efficient structural shape optimization. *Structural and Multidisciplinary Optimization*, 48(5) :987–1000.

[119] Raghavan, B., Breitkopf, P., Tourbier, Y., and Villon, P. (2013b). Towards a space reduction approach for structural shape optimization. *Structural & Multidisciplinary Optimization*.

[120] Raghavan, B., Hamdaoui, M., Xiao, M., Breitkopf, P., and Villon, P. (2013c). A bi-level meta-modeling approach for structural optimization using modified {POD} bases and diffuse approximation. *Computers & Structures*, 127(0) :19 – 28.

[121] Raghavan, B., Le Quilliec, G., Breitkopf, P., Rassineux, A., Roelandt, J.-M., and Villon, P. (2014a). Numerical assessment of springback for the deep drawing process by level set interpolation using shape manifolds. *International Journal of Material Forming*, 7(4) :487–501.

[122] Raghavan, B., Le Quilliec, G., Breitkopf, P., Rassineux, A., Roelandt, J.-M., and Villon, P. (2014b). Numerical assessment of springback for the deep drawing process by level set interpolation using shape manifolds. *International Journal of Material Forming*, 7(4) :487–501.

[123] Raghavan, B., Xia, L., Breitkopf, P., Rassineux, A., and Villon, P. (2013d). Towards simultaneous reduction of both input and output spaces for interactive simulation-based structural design. *Computer Methods in Applied Mechanics and Engineering*, 265 :174–185.

[124] Raghavan, B., Xia, L., Breitkopf, P., Rassineux, A., and Villon, P. (2013e). Towards simultaneous reduction of both input and output spaces for interactive simulation-based structural design. *Computer Methods in Applied Mechanics and Engineering*.

[125] Reed, J., Dean, J., Aldrich-Smith, G., and Clyne, T. (2016). A methodology for obtaining plasticity characteristics of metallic coatings via instrumented indentation. *International Journal of Solids and Structures*, 80 :128–136.

[126] Rodríguez, M., Molina-Aldareguía, J. M., González, C., and LLorca, J. (2012). Determination of the mechanical properties of amorphous materials through instrumented nanoindentation. *Acta Materialia*, 60(9) :3953–3964.

[127] Rokach, L. and Maimon, O. (2014). *Data mining with decision trees : theory and applications*. World scientific.

[128] Russell, S., Norvig, P., and Intelligence, A. (1995). A modern approach. *Artificial Intelligence. Prentice-Hall, Egnlewood Cliffs*, 25 :27.

[129] Sabnis, P. A., Forest, S., Arakere, N. K., and Yastrebov, V. A. (2013). Crystal plasticity analysis of cylindrical indentation on a ni-base single crystal superalloy. *International Journal of Plasticity*, 51 :200 – 217.

[130] Sakagami, T. and Kubo, S. (1999). Development of a new crack identification method based on singular current field using differential thermography. In *AeroSense'99*, pages 369–376. International Society for Optics and Photonics.

[131] Samuel, A. L. (1959). Some studies in machine learning using the game of checkers. *IBM Journal of research and development*, 3(3) :210–229.

[132] Saul, L. K. and Roweis, S. T. (2000). An introduction to locally linear embedding. *unpublished. Available at : http ://www. cs. toronto. edu/˜ roweis/lle/publications. html*.

[133] Saul, L. K., Weinberger, K. Q., Ham, J. H., Sha, F., and Lee, D. D. (2006). Spectral methods for dimensionality reduction. *Semisupervised learning*, pages 293–308.

[134] Schölkopf, B., Smola, A., and Müller, K.-R. (1998). Nonlinear component analysis as a kernel eigenvalue problem. *Neural computation*, 10(5) :1299–1319.

[135] Schulz, V. (2012). A riemannian view on shape optimization. *Foundations of Computational Mathematics*.

[136] Schwiedrzik, J. and Zysset, P. (2015). Quantitative analysis of imprint shape and its relation to mechanical properties measured by microindentation in bone. *Journal of biomechanics*, 48(2) :210–216.

[137] Sebastiani, F. (2002). Machine learning in automated text categorization. *ACM computing surveys (CSUR)*, 34(1) :1–47.

[138] Sebastiani, M., Cusmà, A., Bemporad, E., and Carassiti, F. (2014). Elastic anisotropy of coatings by AFM analysis of microindentations. *Surface Engineering*, 30(1) :41–47.

[139] Shastry, C. G., Mathew, M., Rao, K. B. S., and Mannan, S. (2004). Applicability of voce equation for tensile flow and work hardening behaviour of p92 ferritic steel. *International Journal of Pressure Vessels and Piping*, 81(3) :297 – 301.

[140] Smith, R. L. and Sandly, G. E. (1922). An accurate method of determining the hardness of metals, with particular reference to those of a high degree of hardness. *Proceedings of the Institution of Mechanical Engineers*, 102(1) :623–641.

[141] Sneddon, I. N. (1965). The relation between load and penetration in the axisymmetric boussinesq problem for a punch of arbitrary profile. *International journal of engineering science*, 3(1) :47–57.

[142] Sutton, M. A., Orteu, J. J., and Schreier, H. (2009). *Image correlation for shape, motion and deformation measurements : basic concepts, theory and applications*. Springer Science & Business Media.

[143] Tabor, D. (1951). *The hardness of metals*, volume 10. ClarendonP.

[144] Tabor, D. (1970). The hardness of solids. *Review of physics in technology*, 1(3) :145.

[145] Taljat, B. and Pharr, G. (2004). Development of pile-up during spherical indentation of elastic–plastic solids. *International Journal of Solids and Structures*, 41(14) :3891 – 3904.

[146] T.Benamara, P.Breitkopf, I. C. (2016). Adaptive infill sampling criterion for multi-fidelity optimization based on gappy-pod. *Structural and multidisciplinary optimization*.

[147] Tenenbaum, J. B., De Silva, V., and Langford, J. C. (2000). A global geometric framework for nonlinear dimensionality reduction. *science*, 290(5500) :2319–2323.

[148] Tho, K., Swaddiwudhipong, S., Liu, Z., Zeng, K., and Hua, J. (2004). Uniqueness of reverse analysis from conical indentation tests. *Journal of materials research*, 19(08) :2498–2502.

[149] Tong, S. and Koller, D. (2002). Support vector machine active learning with applications to text classification. *The Journal of Machine Learning Research*, 2 :45–66.

[150] Tu, J., Choi, K. K., and Park, Y. H. (1999). A new study on reliability-based design optimization. *Journal of mechanical design*, 121(4) :557–564.

[151] Tunvisut, K., Busso, E., O'dowd, N., and Brantner, H. (2002). Determination of the mechanical properties of metallic thin films and substrates from indentation tests. *Philosophical Magazine A*, 82(10) :2013–2029.

[152] Tvergaard, V. and Needleman, A. (2011). Polymer indentation : Numerical analysis and comparison with a spherical cavity model. *Journal of the Mechanics and Physics of Solids*, 59(9) :1669 – 1684.

[153] Ullner, C., Reimann, E., Kohlhoff, H., and Subaric-Leitis, A. (2010). Effect and measurement of the machine compliance in the macro range of instrumented indentation test. *Measurement*, 43(2) :216 – 222.

[154] Ulm, F.-J., Vandamme, M., Bobko, C., Alberto Ortega, J., Tai, K., and Ortiz, C. (2007). Statistical indentation techniques for hydrated nanocomposites : Concrete, bone, and shale. *Journal of the American Ceramic Society*, 90(9) :2677–2692.

[155] Van Vliet, K. J., Prchlik, L., and Smith, J. F. (2004). Direct measurement of indentation frame compliance. *Journal of Materials Research*, 19 :325–331.

[156] Venkatesh, T., Van Vliet, K., Giannakopoulos, A., and Suresh, S. (2000). Determination of elasto-plastic properties by instrumented sharp indentation : guidelines for property extraction. *Scripta materialia*, 42(9) :833–839.

[157] Wang, M., Wu, J., Hui, Y., Zhang, Z., Zhan, X., and Guo, R. (2016). Identification of elastic-plastic properties of metal materials by using the residual imprint of spherical indentation. *Materials Science and Engineering : A*.

[158] Wang, S., Lim, K., Khoo, B., and Wang, M. (2007). An extended level set method for shape and topology optimization. *Journal of Computational Physics*, 221(1) :395 – 421.

[159] Willcox, K. and Peraire, J. (2002). Balanced model reduction via the proper orthogonal decomposition. *AIAA Journal*, 40(11) :2323–2330.

[160] Xia, L., Raghavan, B., Breitkopf, P., and Zhang, W. (2013). Numerical material representation using proper orthogonal decomposition and diffuse approximation. *Applied Mathematics and Computation*, 224 :450–462.

[161] Xie, X. and Mirmehdi, M. (2011). Radial basis function based level set interpolation and evolution for deformable modelling. *Image and Vision Computing*, 29(2-3) :167 – 177.

[162] Yagawa, G. and Okuda, H. (1996). Neural networks in computational mechanics. *Archives of Computational Methods in Engineering*, 3(4) :435–512.

[163] Zhang, C. and Wang, B. (2012). Identification of the hardening behavior of solids described by three-parameter voce law using spherical indentation. *Journal of Materials Research*, 27(20) :2624–2629.

[164] Zhang, W.-H., Beckers, P., and Fleury, C. (1995). Unified parametric design approach to structural shape optimization. *International Journal for Numerical Methods in Engineering*, 38(13) :2283–2292.

Annexe A

Preparation of specimens

The tensile test and indentation specimens for the Al alloys were carefully sectioned with a Precision Cut-Off Machine from a laminated hot rolled sheet of 6 mm thickness, while the steel specimen was cut from a cylindrical bar of 30 mm radius. This was followed by polishing using fine emery papers (up to 1200 grit) and diamond suspensions (6 and 3 μm) for the purpose of avoiding roughness-related uncertainties.

TABLE A.1 Surface roughness measures for the studied samples.

Material	root mean square height of surface	Arithmetic average of the roughness profile
	S_q (μm) ISO 25178	R_a (μm) ISO 4287
AISI1095	0.047	0.021
EN AW-2017F	0.097	0.045
EN AW-5754F	0.053	0.028

Figure A.1 shows an example of the roughness profile obtained for the studied materials and Table A.1 gives the values of the root mean square height of the surface S_q obtained according the ISO 25178 standard for the studied materials. In this table, the values of the arithmetic average of the roughness profile R_a according the ISO 4287 standard are also provided.

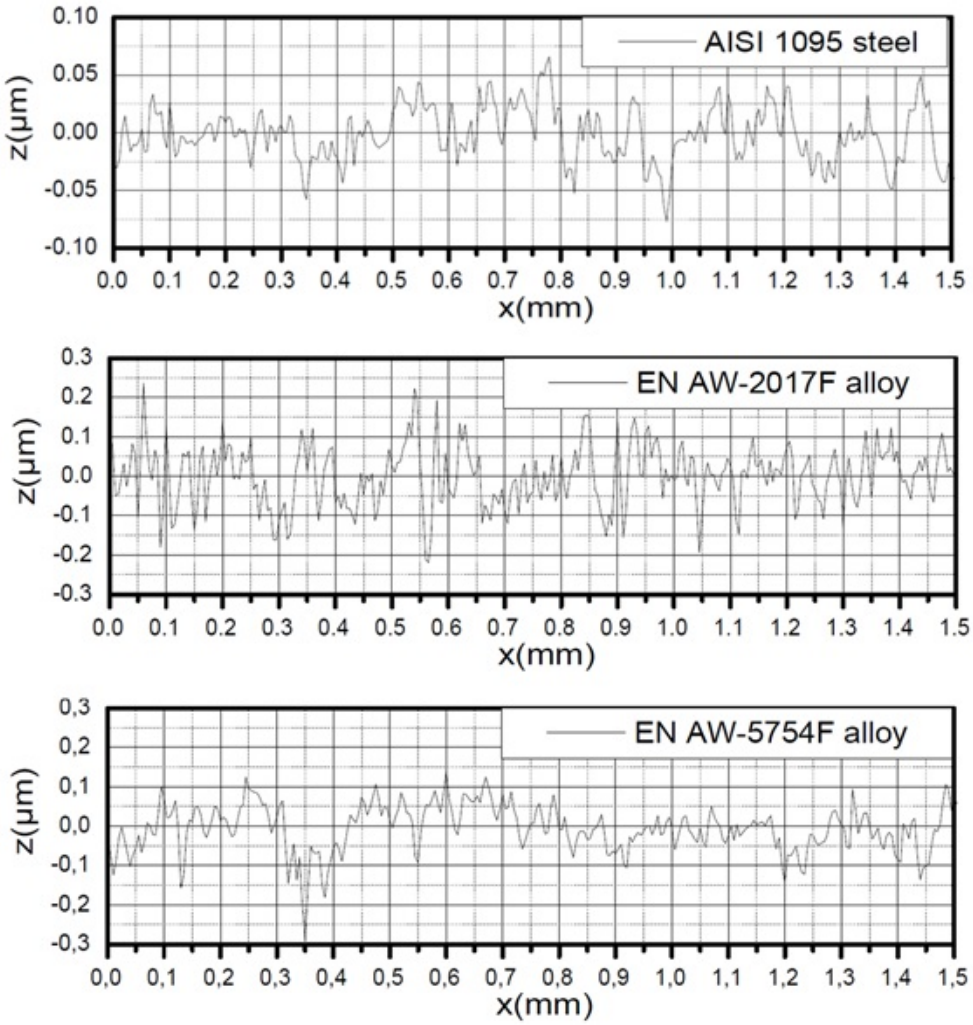

FIGURE A.1 Surface roughness profiles for the three materials.

Annexe B

Identifying AISI 1095 with floating search algorithm

By fixing $E = 210$GPa, the hardening behavior of the material is characterized by identifying the yield stress σ_y and the strain hardening exponent n. We follow the procedures demonstrated using the pseudo-code Algorithm 4 so as to construct the local manifold piece-by-piece using the *floating search* algorithm.

To demonstrate the robustness of the algorithm, we consider three identification cases with 3 different initializations :

A. $\sigma_y = 175$ MPa, $n = 0.3$,

B. $\sigma_y = 155$ MPa, $n = 0.4$ and

C. $\sigma_y = 80$ MPa, $n = 0.25$.

Furthermore, the "shrinking rates" of the search windows are different, we use $\beta = 0.8$ for cases A and B, while $\beta = 0.6$ for case C. The experimentally measured imprint is obviously the same with the one used in [93]. The numerical simulation of the loading and unloading phases of the indentation test is performed with ABAQUS by using the FE model shown in Fig. 4.1 using four-node axisymmetric elements (CAX4). The Coulomb friction coefficient at indenter-specimen interface is set as equal to 0.1. The maximum value of the indentation force $P_{\max}$ is set to equal to 500N in order to obtain a moderate imprint.

A quadric polynomial basis (2D), containing 6 different terms, was applied for the construction of the smooth manifold. 7 snapshots were chosen in each DoE using Latin Hyper Cubic sampling. As earlier, the POD was performed with a full basis of size 7 *without* truncation, although only the first three coordinates are shown here for visualization purposes. The parameters were identified in the mathematical space by using the criterion as given in Equation 4.11.

The identified parameters with different initial points are compared in Table B.1. As can be observed, almost identical results are obtained for the three cases, showing that the material studied has an elastic limit σ_y of around 107 MPa and hardening coefficient $n = 0.324$.

TABLE B.1 Summary of identified hardening coefficient for steel.

Cases	parameters	A	B	C
Starting values	σ_y	175	155	80
	n	0.3	0.4	0.25
Solution	σ_y	105.54	107.04	107.09
	n	0.3263	0.3242	0.3239
	Cost function ε	0.0058	0.0052	0.0087

The different convergence patterns in design space are summarized in Figure B.1. They demonstrate once again that, instead of attempting a *global* manifold construction, the design space is searched in a piece-wise fashion and the search direction is determined automatically using the manifold learning algorithm.

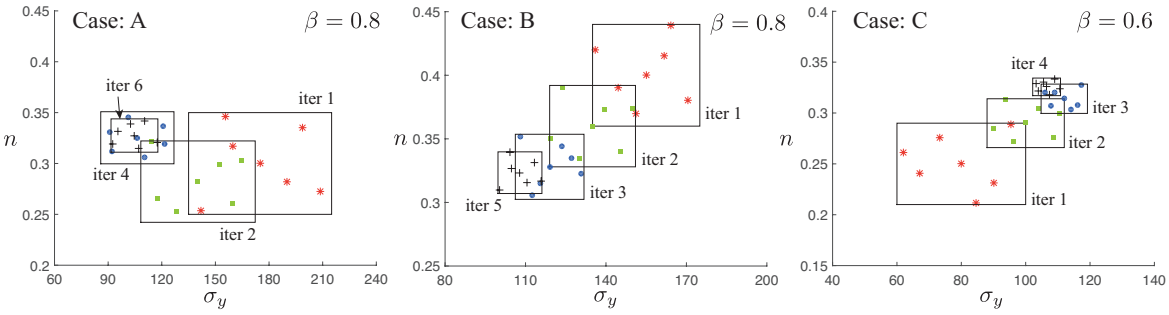

FIGURE B.1 Convergence of design space with different values of β (shrinking coefficient).

Furthermore, Figure B.2 also presents the evolution of several local manifolds in which the red points refer to the snapshots of each iteration, for Case B. As expected, the distance between the experimental imprint (marked with green diamonds) and the estimated admissible imprint on the manifold (represented by a black dot) is minimized. It is also noticed that, at the 5^{th} iteration, the local manifold is small enough so as to be regarded as a tangential approximation of global manifold. Figure B.3 shows the identified imprint of each iteration with the experimental one.

Finally, the convergence summary for the three identification cases is given in Figure B.4. In addition to coincident identification results, the algorithm appears to begin converging from the 5^{th} step, an observation that is in line with the one from Figure B.2.

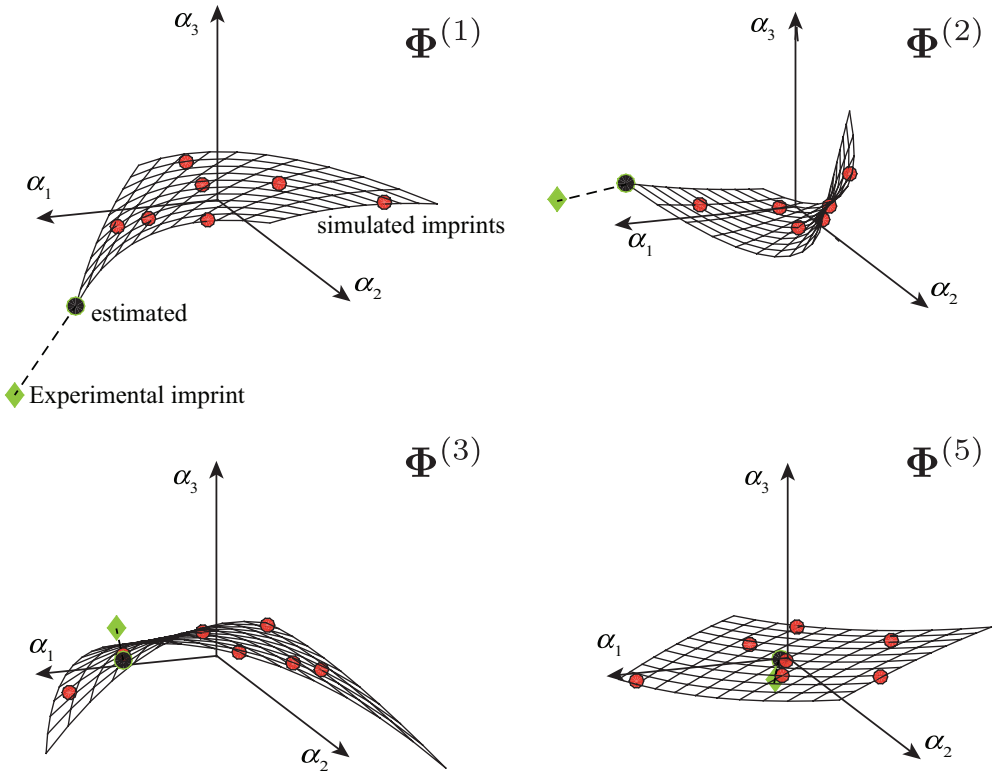

FIGURE B.2 Actual convergence of the local manifold for case B.

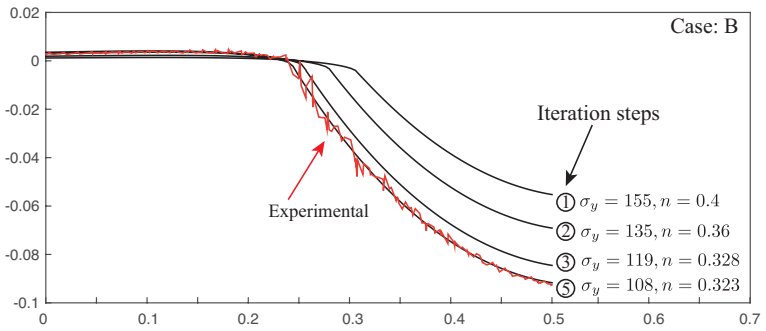

FIGURE B.3 Convergences of residual imprints for case B.

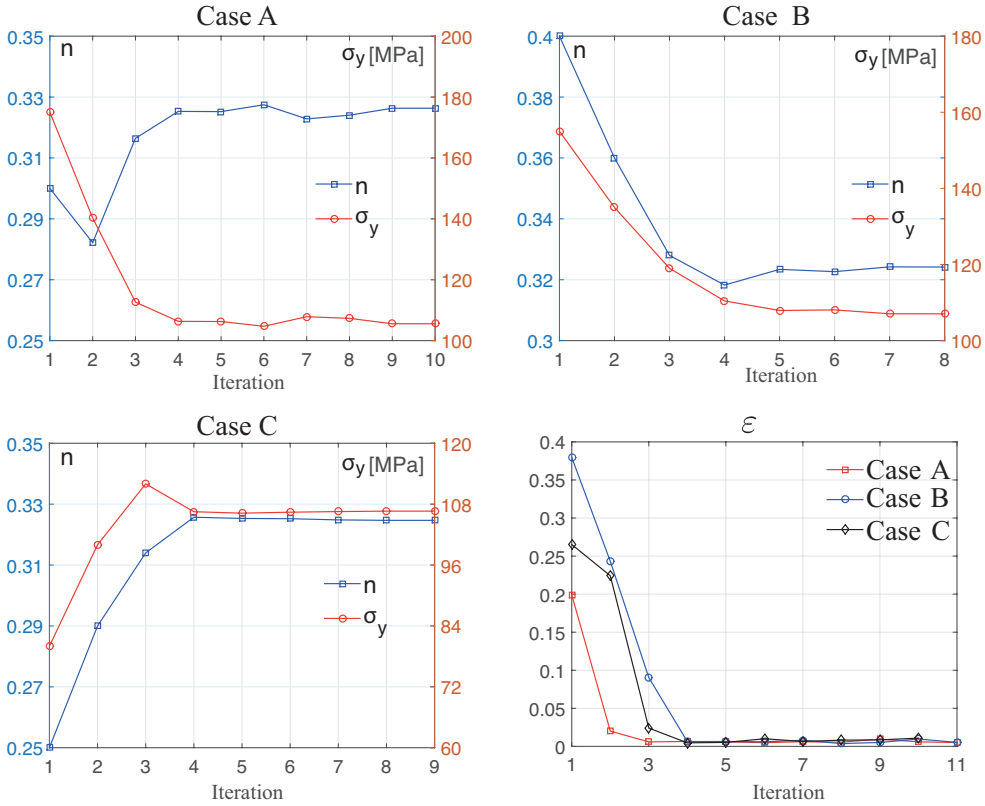

FIGURE B.4 Convergence summary for the three cases.

Annexe C

Verification of local-manifold identification method

In this section, the robustness of the manifold-based identification protocol is accessed on the basis of various parameters involved in local manifold construction. For simplicity sake, we focus on the characterization of AISI 1095 steel using the *panning & zooming* algorithm.

C.1 Truncation on POD modes

In our work, we aim to minimize the distance between the experimental and simulated imprints in shape space. Thus, it is unnecessary to perform any truncation like in the traditional POD method. First of all, the optimization problem is already placed in a rather low dimensional space, and computing the Eulerian distance is straightforward and easy. In addition, for the sake of higher precision, we retain all POD modes, and we do not choose a threshold value for POD truncation either. Moreover, the first several modes are dominant, while the others are merely numerical noise with negligible amplitude (the corresponding α-coordinates tend to zero). By consequence, their influence on the convergence criterion is fairly limited. To verify this, we performed a series of identifications by employing different number of modes (Table C.1).

TABLE C.1 Identified results with truncated POD modes.

Parameters	n_{mod}=2	n_{mod}=3	n_{mod}=4	n_{mod}=5	n_{mod}=6
σ_y	245	108.0	106.0	105.8	106.0
n	0.175	0.321	0.326	0.326	0.326

We observe that the values of σ_y and n almost stabilized for $n_{\text{mod}} \geq 4$. Thus, we would like

to conclude that in order to identify material properties using the shape manifold learning approach, the size of minimum orthogonal basis of the reduced shape space is $n_{\text{mod}} = 2l$, where l is the number of parameters. However, this is still open to discussion, and it is one of the reasons why we prefer using all the modes without truncation.

C.2 Sensitivity to different prescribed loads

We test in this section the proposed methodology with a prescribed force of 300 N (instead of the previously used 500 N in Section 7.2). Due to the absence of experimental indentation data for this value, we first generated the pseudo imprint using the pre-defined material parameter set : $\sigma_y = 107$ MPa, $n = 0.324$. Next, a 3% white noise was introduced to the obtained imprint and finally, the "missed" parameters are identified (results shown in Table C.2).

TABLE C.2 Identified results with prescribed force of 300 N.

Parameters	Identified value	reference value	relative error
σ_y	109.7	107	2.52%
n	0.3208	0.324	0.99%

As the table indicates, acceptable errors are obtained (lower than the percentage of introduced noise) when comparing with the pre-defined ones, and we may attribute this error to the inaccuracy of the manifold and noise introduced. However, it must be mentioned that, when using the proposed method, the maximum force needs to be large enough to involve plastic deformations. Otherwise, imprint-based identification would be impossible since all the deformation would be recovered after elastic spring back.

C.3 Inaccuracy of local manifold

We mentioned in Section 5.1 that when we project the experimental imprint onto the shape space, *even* assuming that the indented material behaved exactly according to the postulated plastic hardening law, the projection will never lie *exactly* on the manifold due to noise in the measured data. While this statement is based on the fundamental hypothesis of manifold, and it is only true for the an ”exact” manifold.

In the implementation of the current work, the local manifold is described by its parametric form using (moving) least squares approximation, and thus it is inexact. Consequently,

the offset of experimental imprint from the local manifold may be attributed to two factors (assuming again that the indented material hardens according the power law)

1. inaccuracy of manifold ;
2. measurement noise.

In order to quantify these two errors, we adopt the manifold in Figure 7.12, and project a smooth imprint simulated with the parameter set $\sigma_y = 107$ Mpa and $n = 0.324$ onto the α-space. We obtain a distance of the projection to the manifold is 7.0×10^{-4}, compared with 3.0×10^{-3} for the imprint with noise.

Thus, we may conclude that since the manifold is approximated in the vicinity of the snapshot, and considering the simplicity of the problem itself, the error caused by measurement error could be dominant compared with the error incurred by manifold inaccuracy. This statement could be further explained by observing the accuracy of identification using even lower-order polynomial basis in the next section.

C.4 The effect of polynomial basis

In present work, the global manifold is approximated progressively by lower-dimensional local ones based on a set of snapshots in the vicinity of current evaluation point. A quadratic polynomial basis has been adopted as it allows for gradient and Hessian evaluation. However, the number of terms of quadratic basis increases rapidly with the number of parameters. Therefore, we investigate a lower-order *bilinear* basis for the sake of reduction in the number of snapshots per iteration. The essential significance of lower order polynomial basis will be firmly highlighted when more parameters need to be identified. For example, in the case where 5 parameters are involved, the number of snapshots per iteration needed for bilinear and quadratic basis is 16 and 32, respectively.

By choosing the same initial evaluation for the two parameters, a comparison of bilinear and quadratic basis are conducted and the results are given in Table C.3. Excepting for the almost identical results, it is also observed that, as expected, the total numbers of simulations for bilinear basis is less than that for quadratic basis, 50 compared with 56.

TABLE C.3 Identified results derived by adopting different polynomial basis.

Polynomial basis	σ_y	n	Iterations	Snapshots	Total simulations
Quadratic	107.0	0.324	8	7	56
Bilinear	108.4	0.321	10	5	50

C.5 The effect of number of snapshots k

In our fist test case on the steel, the local manifolds are approximated by a quadratic bivariate polynomial basis, in which 6 coefficients need to be determined. However, considering the numerical instability of simulation, we have chosen 7 snapshots to construct the local manifold so as to guarantee the unicity of solution to Equation 3.11 in the case where one of the simulations does not converge.

To have a better understanding of the influence of the number of snapshots for each iteration, we performed several identification procedures by adopting even more snapshots, and the stability can be observed form Table C.4

TABLE C.4 Identified results using different number of snapshots.

Parameters	$k=7$	$k=8$	$k=9$	$k=10$
σ_y	104.0	105.6	106.6	105.0
n	0.330	0.324	0.325	0.322